

# **Investigation of High-Frequency Thermoacoustic Instabilities**

Von der Fakultät für Ingenieurwissenschaften, Abteilung Maschinenbau und Verfahrenstechnik  
der

Universität Duisburg-Essen

zur Erlangung des akademischen Grades

eines

Doktors der Ingenieurwissenschaften

Dr.-Ing.

genehmigte Dissertation

von

**Vahid Sharifi**

aus

Teheran

Gutachter: Univ.-Prof. Dr.-Ing. Andreas M. Kempf

Univ.-Prof. Dr.-Ing. C. Oliver Paschereit

Tag der mündlichen Prüfung: 24.06.2021



*This work is dedicated to the memory of my beloved father who always, with no ifs  
and buts, fought for my success.*



## Acknowledgements

This work was conducted at the Chair of Fluid Dynamics at the University of Duisburg-Essen in cooperation with Siemens Energy company. I am very grateful to the head of the chair, Prof. Dr.-Ing. Andreas M. Kempf, for allowing me the opportunity to complete my PhD under his supervision. I will always be indebted to him for his professional and personal support and for his enormous dedication, which helped me tremendously in advancing my research project. During my promotion, I had the exclusive opportunity to spend half of my time in the development department for combustion chambers at Siemens Energy working on my dissertation. I would also like to thank Dr. Christian Beck very much for his commitment, his time and his competent support as well as for his trust in me.

I would like to thank my colleagues at the Chair of Fluid Mechanics for many valuable discussions and suggestions. With a special mention of Dr. Cifuentes, Dr. Deng, Dr. Janas, Dr. Mohri, Dr. Nguyen, Dr. Proch, Dr. Rittler, Dr. Rieth, Dr. Sikalo, Dr. Wlokas, Pascal Gruhlke, Eray Inanc, Hossein Janbazi, Timo Lipkowicz, Johannes Sellmann and Patrick Wollny. My special thanks go to my colleague at the development department for combustion chambers at Siemens Energy for their support and encouragement. With a special mention of Dr. Flohr, Dr. Huth, Dr. Janus, Dr. Kaufmann, Dr. Terjung, Dr. Walz and Dr. Werdelman. Thanks also go to the secretary of our chair, Sylvia Helwig, and the IT-administrator Michael Vetter and all the other colleagues who made the atmosphere of cooperation as professional and great as it was.

At last, but certainly not least, I would like to express my gratefulness to my parents, my brothers and my wife, who support and encourage me at all times.

Place: Duisburg

Date: 20.07.2021

**Signature**

*VSharifi*



## Abstract

The motivation of the present work was to develop a simple laboratory-scale atmospheric test case that can be used for the analysis and modeling of thermoacoustic oscillations.

To gain a better understanding of the interaction of the transverse acoustic waves and the flames, forced-response large-eddy simulations (LES) were performed for two types of acoustic flame interaction: a) velocity forcing: the flame was placed at the acoustic pressure node and b) pressure forcing: the flame was placed at the acoustic pressure anti-node. The comparison of the results of the two acoustic/flame interactions showed that the flame at the pressure anti-node is generally more susceptible to thermoacoustic instabilities. Density oscillations were identified as the main driving mechanism in the case of pressure forcing and the flame displacement mechanism in the case of velocity forcing.

Based on the lessons learned from the forced response studies, a generic combustor was constructed using LES, which can exhibit self-excited thermoacoustic instabilities in a frequency range often observed in real gas turbines. Additional investigations allowed a gradual increase in the complexity of the combustor in terms of realistic boundary conditions and geometry until a feasible configuration for the experiment was obtained. This configuration was subsequently investigated experimentally. For a given air mass flow, thermoacoustic instabilities of the first radial mode were identified when a critical equivalence ratio was exceeded. The largest amplitude was observed at an equivalence ratio of a slightly lean mixture. The ability of the numerical method with respect to high-frequency thermoacoustics and stable combustion prediction were taken into account. It could be demonstrated that CFD could reliably predict the results with a reasonable agreement for both states.

The developed experiment proves the capability of LES as a design tool for thermoacoustic applications and opens the door for more sophisticated experiments to gain a better understanding of these kinds of instabilities.

## Zusammenfassung

Die Motivation der vorliegenden Arbeit war es, einen einfachen atmosphärischen Testfall im Labormaßstab zu entwickeln, der für die Analyse und Modellierung thermoakustischer Instabilitäten verwendet werden kann.

Um ein besseres Verständnis der Wechselwirkung zwischen den transversalen akustischen Wellen und den Flammen zu erhalten, wurden für zwei Arten der akustischen Flammenwechselwirkung fremderregte Large-Eddy-Simulationen (LES) durchgeführt:

- a) Geschwindigkeitsanregung: Die Flamme wurde am Schalldruckknoten platziert und
- b) Druckerregung: Die Flamme wurde am Schalldruckbauch platziert. Der Vergleich der Ergebnisse der beiden Wechselwirkungen zeigte, dass die Flamme am Schalldruckbauch anfälliger für thermoakustische Instabilitäten ist. Es wurden Dichteoszillationen als Hauptmechanismus im Falle von Druckerregung und der Flammenverschiebungsmechanismus im Falle von Geschwindigkeitsanregung identifiziert.

Basierend auf den Erkenntnissen aus den Forced-Response-Studien wurde unter Verwendung von LES eine generische Brennkammer konstruiert, die selbsterregte thermoakustische Instabilitäten in einem Frequenzbereich aufweisen kann, der häufig bei Gasturbinen beobachtet wird. Weitere Untersuchungen ermöglichten eine schrittweise Erhöhung der Komplexität der Brennkammer hinsichtlich realistischer Randbedingungen und Geometrie, bis eine realisierbare Konfiguration für das Experiment erreicht war. Diese Konfiguration wurde anschließend experimentell untersucht. Für einen gegebenen Luftmassenstrom wurden thermoakustische Instabilitäten der ersten radialen Mode identifiziert, wenn ein kritisches Äquivalenzverhältnis überschritten wurde. Die größte Amplitude wurde bei einem Äquivalenzverhältnis einer leicht mageren Mischung beobachtet. Die Vorhersagekraft der numerischen Methode in Bezug auf die hochfrequente thermoakustische Instabilitäten und die Vorhersage einer stabilen Verbrennung wurden untersucht. Es konnte gezeigt werden, dass CFD die Ergebnisse mit einer vernünftigen Übereinstimmung für beide Zustände zuverlässig vorhersagen konnte.

Das entwickelte Experiment beweist die Fähigkeit von LES als Designwerkzeug für thermoakustische Anwendungen und öffnet die Tür für anspruchsvollere Experimente, um ein besseres Verständnis dieser Art von Instabilitäten zu erlangen.

# TABLE OF CONTENTS

|   |           |
|---|-----------|
| <b>LIST OF FIGURES</b>                                | viii      |
| <b>LIST OF TABLES</b>                                 | xi        |
| <b>LIST OF SYMBOLS</b>                                | xii       |
| <b>1 Introduction</b>                                 | <b>1</b>  |
| 1.1 Thermoacoustic Instabilities: Literature Overview | 2         |
| 1.1.1 Instability Mechanisms                          | 5         |
| 1.1.2 Methods of Investigation                        | 10        |
| 1.2 Motivation and Overview of the Present Work       | 14        |
| <b>2 Theory</b>                                       | <b>19</b> |
| 2.1 Governing Equations                               | 19        |
| 2.2 Turbulence Theory                                 | 20        |
| 2.2.1 Turbulent Length and Time Scale                 | 21        |
| 2.3 Combustion Theory                                 | 22        |
| 2.3.1 Chemistry Description                           | 22        |
| 2.3.2 Combustion Mode                                 | 24        |
| 2.4 Acoustic Theory                                   | 27        |
| 2.4.1 Acoustic Source Term                            | 29        |
| <b>3 Simulation and Modelling of Reactive Flows</b>   | <b>31</b> |
| 3.1 Direct Numerical Simulation                       | 31        |
| 3.2 Large Eddy Simulation                             | 31        |
| 3.2.1 Favre-Filtered Governing Equations              | 32        |
| 3.2.2 Sub-Grid Scale Turbulence Models                | 33        |
| 3.2.3 Turbulent Combustion Modeling                   | 34        |
| <b>4 Numerical Methods</b>                            | <b>37</b> |

|          |  |           |
|----------|--|-----------|
| 4.1      | Finite Volume Method . . . . .   | 37        |
| 4.2      | Numerical Discretization Schemes . . . . .   | 38        |
|          | 4.2.1 Spatial Discretization . . . . .   | 38        |
|          | 4.2.2 Temporal Discretization . . . . .  | 40        |
| 4.3      | Boundary Conditions . . . . .  | 41        |
|          | 4.3.1 Non-Reflective Boundary Conditions . . . . .   | 41        |
|          | 4.3.2 Turbulent Boundary Condition . . . . .   | 45        |
| <b>5</b> | <b>Large-Eddy Simulation of Acoustic Flame Response to High-Frequency<br/>Transverse Excitations</b> | <b>47</b> |
| 5.1      | Introduction . . . . .   | 48        |
| 5.2      | Test Cases . . . . .   | 51        |
| 5.3      | Modeling and Simulation . . . . .  | 53        |
|          | 5.3.1 Combustion Model . . . . .   | 53        |
|          | 5.3.2 Rayleigh Index and Budget Analysis . . . . .   | 55        |
| 5.4      | Results . . . . .  | 58        |
|          | 5.4.1 Comparing Pressure Forcing and Velocity Forcing . . . . .                                      | 58        |
|          | 5.4.2 Effect of Forcing Frequency . . . . .  | 63        |
|          | 5.4.3 Effect of the Flame Length on the Rayleigh Indices . . . . .                                   | 66        |
| 5.5      | Conclusion . . . . .   | 68        |
| <b>6</b> | <b>High-Frequency Instabilities in a Cylindrical Single-Jet Combustion<br/>Chamber</b>               | <b>69</b> |
| 6.1      | Introduction . . . . .   | 70        |
| 6.2      | Design Process of the Generic Configuration . . . . .  | 71        |
| 6.3      | Modeling and Simulation . . . . .  | 72        |
| 6.4      | Results . . . . .  | 73        |
|          | 6.4.1 Influence of Equivalence Ratio on the Instabilities . . . . .                                  | 73        |
|          | 6.4.2 Influence of Chamber Wall Temperature on Instabilities . . . . .                               | 75        |
| 6.5      | A strategy to Dampen Thermoacoustic Instabilities . . . . .  | 77        |
| 6.6      | Influence of Upstream Acoustic Boundary Conditions on Instabilities . . . . .                        | 79        |
| 6.7      | The Final Configuration . . . . .  | 80        |
| 6.8      | Conclusion . . . . .   | 81        |

|                     |   |            |
|---------------------|---|------------|
| 6.9                 | Acknowledgments . . . . .   | 82         |
| <b>7</b>            | <b>Design and Testing of a High Frequency Thermoacoustic Combustion</b> |            |
|                     | <b>Experiment</b>   | <b>83</b>  |
| 7.1                 | Introduction . . . . .  | 83         |
| 7.2                 | Experiment . . . . .  | 86         |
|                     | 7.2.1 Design - based on <i>a priori</i> LES . . . . .                   | 86         |
|                     | 7.2.2 Experimental setup and diagnostics . . . . .                      | 88         |
|                     | 7.2.3 Experimental Results . . . . .                                    | 91         |
| 7.3                 | Numerical Investigation . . . . .                                       | 94         |
|                     | 7.3.1 Test Cases and Operating Points . . . . .                         | 94         |
|                     | 7.3.2 Modeling and Simulation . . . . .                                 | 97         |
|                     | 7.3.3 Numerical Results . . . . .                                       | 100        |
|                     | 7.3.4 Mechanism of instabilities . . . . .                              | 109        |
| 7.4                 | Conclusion . . . . .  | 112        |
| <b>8</b>            | <b>Summery and outlook</b>  | <b>115</b> |
| <b>Appendix A</b>   | <b>Validation of the Combustion Model</b>                               | <b>121</b> |
| <b>Appendix B</b>   | <b>Grid Refinement Study</b>  | <b>125</b> |
| <b>Bibliography</b> | . . . . .   | 126        |

## LIST OF FIGURES

|      |  |    |
|------|--|----|
| 1.1  | Thermoacoustic loop. . . . .   | 3  |
| 1.2  | Combustors damaged by HFI. . . . .                                   | 3  |
| 1.3  | Acoustic mode shapes. . . . .  | 4  |
| 1.4  | Schematic of the Rijke tube. . . . .                                 | 5  |
| 1.5  | Vortex shedding in Volvo test case. . . . .                          | 11 |
| 2.1  | Kolmogorov energy spectrum. . . . .                                  | 21 |
| 2.2  | Turbulent combustion regimes. . . . .                                | 25 |
| 2.3  | Limit-cycles. . . . .  | 30 |
| 4.1  | One-dimensional grid system. . . . .                                 | 38 |
| 4.2  | TVD region based on sweby. . . . .                                   | 41 |
| 4.3  | Boundary conditions located on the x-axis. . . . .                   | 42 |
| 5.1  | Can-type combustor. . . . .  | 51 |
| 5.2  | Simplified combustor. . . . .  | 51 |
| 5.3  | Comparison of the global heat release rate oscillations. . . . .     | 57 |
| 5.4  | Phase averaged unsteady pressure field. . . . .                      | 58 |
| 5.5  | Phase averaged contour of the regress variable. . . . .              | 59 |
| 5.6  | Flame shape changes due to the acoustic transverse velocity. . . . . | 61 |
| 5.7  | Phase averaged Q-isosurface. . . . .                                 | 62 |
| 5.8  | Phase averaged contours of the regress variable. . . . .             | 63 |
| 5.9  | Heat release rate amplitude due to respective contributions. . . . . | 64 |
| 5.10 | Acoustic transverse pressure distributions at 90°. . . . .           | 65 |
| 5.11 | Rayleigh Indices over forcing frequencies. . . . .                   | 66 |
| 5.12 | Rayleigh Index over flame length. . . . .                            | 67 |
| 6.1  | Schematic of SiGenUDE. . . . .                                       | 72 |
| 6.2  | Spectra of pressure signal captured at Pw. . . . .                   | 73 |
| 6.3  | Amplitude distribution of the acoustic pressure. . . . .             | 74 |

|      |  |     |
|------|--|-----|
| 6.4  | Phase-averaged line of sight fields of heat release. . . . .   | 76  |
| 6.5  | Pressure amplitude over combustion chamber temperature. . . . .                                      | 76  |
| 6.6  | Fields of temperature and amplitude of acoustic pressure. . . . .                                    | 77  |
| 6.7  | Pressure history and Time-averaged axial velocity. . . . .   | 78  |
| 6.8  | DFT of pressure, fields of equivalence ratio and Phase-averaged global<br>heat release rate. . . . . | 79  |
| 6.9  | Schematic of upstream plenums. . . . .   | 80  |
| 6.10 | Pressure history and Phase plane of the established oscillations. . . . .                            | 81  |
| 6.11 | Fields of velocity and Amplitude distribution of the acoustic pressure. . . . .                      | 81  |
| 7.1  | Fields of temperature and amplitude of the acoustic pressure. . . . .                                | 88  |
| 7.2  | Single-jet Metallic HFI combustor. . . . .   | 89  |
| 7.3  | Fourier transform of signals recorded by the pressure transducers. . . . .                           | 92  |
| 7.4  | Wall temperature of the cylindrical part of combustor. . . . .                                       | 93  |
| 7.5  | Amplitude of acoustic oscillations versus global equivalence ratio. . . . .                          | 94  |
| 7.6  | HFI-Combustor wall temperature as a function of equivalence ratio. . . . .                           | 95  |
| 7.7  | Amplitude of acoustic oscillations versus bulk jet velocity. . . . .                                 | 95  |
| 7.8  | Experimental data vs. LES results for unstable operating point. . . . .                              | 102 |
| 7.9  | Mean measured temperature as a function of the HFI-Combustor length. . . . .                         | 102 |
| 7.10 | HFI-Amplitude vs. HFI-Combustor radius. . . . .  | 103 |
| 7.11 | Experimental data vs. LES results for stable operating point. . . . .                                | 103 |
| 7.12 | Comparison of the pressure signal for UTC and RTC. . . . .   | 104 |
| 7.13 | Comparison of the acoustic mode shapes; RTC vs. UTC. . . . .   | 105 |
| 7.14 | Comparison of the axial acoustic velocity and its phase. . . . .                                     | 106 |
| 7.15 | Line of sight fields of heat release rate. . . . .   | 107 |
| 7.16 | Instantaneous and time-averaged fields of the axial velocity. . . . .                                | 107 |
| 7.17 | Comparison of the time-averaged temperature field for RTC and UTC. . . . .                           | 108 |
| 7.18 | Comparison of the instantaneous temperature field for RTC and UTC. . . . .                           | 109 |
| 7.19 | Time averaged temperature and axial velocity over the chamber radius. . . . .                        | 110 |
| 7.20 | Phase-averaged normalized global heat release rate. . . . .  | 111 |
| 7.21 | Comparison of fields of local Rayleigh indices for RTC and UTC. . . . .                              | 113 |
| A.1  | Computational domain of the triple jet. . . . .  | 122 |
| A.2  | Field of methane concentration from experiment and CFD. . . . .                                      | 123 |

|     |  |     |
|-----|--|-----|
| A.3 | CO2 mass fraction and mean progress variable. . . . .            | 123 |
| B.1 | Axial velocity and the temperature fields. . . . .               | 125 |
| B.2 | Time averaged and rms-value of velocity and temperature. . . . . | 125 |

## LIST OF TABLES

|     |  |     |
|-----|--|-----|
| 5.1 | Overview of the operating conditions . . . . .                         | 52  |
| 5.2 | Overview of the operating conditions . . . . .                         | 53  |
| 6.1 | Overview of the operating conditions. . . . .                          | 78  |
| 6.2 | Overview of the operating conditions. . . . .                          | 81  |
| 7.1 | Eigenfrequencies in Hz. . . . .  | 91  |
| 7.2 | LES vs. experiment: Differences in amplitudes and frequencies. . . . . | 101 |
| 7.3 | Normalized Rayleigh indices of different contributions. . . . .        | 112 |
| A.1 | Boundary condition for the validation case . . . . .                   | 122 |



## LIST OF SYMBOLS

|           |  |
|-----------|--|
| $A$       | burning area, $m^2$                          |
| $a_0$     | sound speed, $m/s$                           |
| $a_i$     | $i$ -ten NASA polynomials coefficients       |
| $Amp$     | amplitude, $Pa$                              |
| $b$       | regress variable                             |
| $c$       | progress variable                            |
| $D$       | diffusion coefficient, $m^2/s$               |
| $D_c$     | chamber diameter, $m$                        |
| $D_m$     | molecular diffusion coefficients, $m^2/s$    |
| $D_f$     | sub-grid diffusion coefficients, $m^2/s$     |
| $d\theta$ | phase difference, <i>degree</i>              |
| $e_{ac}$  | acoustic energy density, $J/m^3$             |
| $f$       | frequency of oscillation, $Hz$               |
| $H$       | heat of reaction per mass of fuel, $J/kg$    |
| $h$       | specific absolute enthalpy, $J/kg$           |
| $\hat{i}$ | amplitude of the $i$ -oscillation            |
| $k_{sgs}$ | sub-grid turbulent kinetic energy, $m^2/s^2$ |
| $Le$      | Lewis number                                 |
| $\dot{m}$ | mass flow rate, $kg/s$                       |
| $P$       | power, $W$                                   |
| $p$       | pressure, $Pa$                               |
| $Q$       | Q-criterion, $1/s^2$                         |
| $\dot{q}$ | local heat release rate per volume, $W/m^3$  |

|                 |   |
|-----------------|---|
| $\dot{Q}$       | total heat release rate of the system, $W$  |
| $\dot{Q}_\rho$  | total heat release rate of the contribution from density oscillation, $W$                   |
| $\dot{Q}_{S_l}$ | total heat release rate of the contribution from laminar flame speed oscillation, $W$       |
| $\dot{Q}_\Xi$   | total heat release rate of the contribution from sub-grid wrinkling factor oscillation, $W$ |
| $\dot{Q}_A$     | total heat release rate of the contribution from burning area oscillation, $W$              |
| $\dot{Q}_{f_t}$ | total heat release rate of the contribution from fuel mass fraction oscillation, $W$        |
| $R'$            | specific gas constant, $J/kg \cdot K$   |
| $RI$            | total Rayleigh Index of the system, $W$   |
| $RI_\rho$       | Rayleigh Index of the contribution from density oscillation, $W$                            |
| $RI_{S_l}$      | Rayleigh Index of the contribution from laminar flame speed oscillation, $W$                |
| $RI_\Xi$        | Rayleigh Index of the contribution from sub-grid wrinkling factor oscillation, $W$          |
| $RI_A$          | Rayleigh Index of the contribution from burning area oscillation, $W$                       |
| $RI_{f_t}$      | Rayleigh Index of the contribution from fuel mass fraction oscillation, $W$                 |
| $S_l$           | laminar flame speed, $m/s$  |
| $Sc_t$          | turbulent Schmidt number  |
| $T$             | temperature, $K$  |
| $t_p$           | time period of acoustic oscillation, $s$  |
| $u$             | axial velocity, $m/s$   |
| $u$             | axial velocity, $m/s$   |
| $u'_{sgs}$      | sub-grid velocity fluctuation, $m/s$  |
| $V$             | combustor volume, $m^3$   |
| $v$             | transverse velocity, $m/s$  |
| $W$             | molecular weight, $kg/mol$  |

|                  |  |
|------------------|--|
| $Y_f$            | fuel mass fraction in reactants              |
| $\alpha_l$       | thermal diffusivity, $m^2/s$                 |
| $\gamma$         | heat capacity ratio                          |
| $\Delta$         | filter size, $m$                             |
| $\Theta$         | phase, $rad$                                 |
| $\mu_t$          | turbulent viscosity $Pa \cdot s$             |
| $\nu$            | molecular viscosity, $kg/ms$                 |
| $\nu_t$          | sub-grid scale eddy viscosity, $kg/ms$       |
| $\Xi$            | sub-grid scale flame wrinkling factor        |
| $\rho$           | density, $kg/s$                              |
| $\Sigma_{gen}$   | generalized flame surface density, $1/m$     |
| $\rho$           | density, $kg/s$                              |
| $\tau$           | relaxation time scale, $s$                   |
| $\Xi$            | sub-grid scale flame wrinkling factor        |
| $\dot{\omega}_c$ | source term for progress variable, $kg/m^3s$ |

#### Subscripts

|      |                |
|------|----------------|
| 0    | mean value     |
| 1    | acoustic value |
| $c$  | coarse mesh    |
| $f$  | fine mesh      |
| $F$  | Fuel           |
| $j$  | jet            |
| $m$  | medium mesh    |
| $mi$ | mixture        |
| $p$  | products       |
| $r$  | reactants      |
| $u$  | unburned       |

#### Abbreviation

|     |                             |
|-----|-----------------------------|
| CDS | Central Differencing Scheme |
|-----|-----------------------------|

|     |  |
|-----|--|
| CFD | Computational Fluid Dynamics             |
| HFI | High Frequency Instabilities             |
| IFI | Intermediate Frequency Instabilities     |
| LES | Large Eddy Simulation                    |
| LFI | Intermediate Frequency Instabilities     |
| RI  | Rayleigh Index                           |
| RTC | Realistic wall Temperature Configuration |
| TVD | Total Variation Diminishing              |
| UDS | Upwind Differencing Scheme               |
| UTC | Uniform wall Temperature Configuration   |

## CHAPTER 1

### Introduction

The International Energy Agency (IEA) predicts in its "World Energy Outlook 2019" [1] a further increase of natural gas use to generate electricity over the next 20 years. Power generation with high-performance gas turbines remains an economically efficient process. The political pressure to reduce emissions and the demand for higher gas turbine efficiency make further technological improvements imperative.

Gas turbines consist of three main modules, a compressor, a combustor and a turbine. The combustor section is responsible for mixing the compressed air with the fuel, and subsequent combustion. During the combustion process, emissions such as CO, CO<sub>2</sub>, NO<sub>x</sub> and soot particles are released. Nitrogen oxide gases are the most toxic emissions and have a direct (e.g. by respiration) and indirect (e.g. by contaminating plants) harmful effect on human health [2]. Therefore they are subject to strict regulations worldwide [3]. The main strategy for controlling NO<sub>x</sub> emissions of heavy-duty gas turbines is to reduce the maximum temperature in the combustion chamber. The reduction of the peak temperature in the combustion chamber was partially made possible by the introduction of lean premixed combustion systems. For a given amount of air from the compressor, a further reduction in NO<sub>x</sub> emissions can also be achieved by reducing the amount of cooling air. This increases the amount of air used for mixing and combustion by this amount. Thus, the maximum temperature can be lowered using a leaner mixture, while maintaining the total power generation capacity [4]. A strategy to reduce the amount of cooling air, which is followed and reflected in the historical development of industrial gas turbines of Siemens [5], is the development of more compact combustion chambers. The first generation of Siemens gas turbines was equipped with a silo-combustor with a large surface area. The next generations were equipped with can combustors and annular combustion chambers [6].

Although annular combustors have the most compact design, their further development is more complex and expensive compared to can combustors. Reliable investigations on such combustion chambers must include the entire combustion chamber, since the flames of the individual burners interact with each other and with the various thermoacoustic modes of the combustor [7]. For can combustion chambers, the analysis of a single can is representative for the entire module. To reduce the time-to-market and cost

involved in developing new gas turbines, the major manufacturers of high-performance gas turbines focus on the further advancement of can-based combustion chambers.

Thermoacoustic instabilities are one of the main problems in the further development of gas turbine technologies. These type of instabilities arise from the coupling of heat release fluctuations and the resonances of the confined combustor and are destructive in nature. They limit the operating range and performance of gas turbines and indirectly increase the emissions of the gas turbines [8]. A common method to mitigate thermoacoustic instabilities is to add additional acoustic damping to the system, e.g. by using Helmholtz-based resonators [9]. The resonators are mounted on the combustor walls. To avoid any thermal damage to the resonators, they are cooled with purge air extracted from the last compressor stage [10]. This leads to a reduction in the air available for the combustion process and thus reduces the power output of the gas turbine at a fixed equivalence ratio. To compensate the resulting power losses, the combustion chamber must be operated with a richer mixture and thus at a higher temperature. This increases the thermal  $\text{NO}_x$  emission. Moreover, resonators are only efficient in a very narrow frequency band around their resonant frequency, so resonators of different sizes are required to suppress the wider frequency range of thermoacoustic instabilities [9].

The gas turbine industry is constantly investigating new strategies to develop a robust combustion chamber that is resistant to thermoacoustic instabilities. The aim is to be less dependent on conventional damping methods (e.g. Helmholtz resonators), which influence the performance and efficiency of gas turbines [11]. In the past, several successful concepts for mitigating low-frequency thermoacoustic instabilities have been proposed, e.g. by changing fuel injection positions and the corresponding time-delay distributions [12]. However, there is still no established design concept that can be used against high-frequency thermoacoustic instabilities. This may be because the mechanisms responsible for the occurrence of this type of instability are not well understood. Therefore, a better understanding of the driving mechanisms and identifying the conditions under which they occur is essential.

## 1.1 Thermoacoustic Instabilities: Literature Overview

Noise generation is a characteristic feature of combustion processes. In a confined system, the generated noise can be reflected at the boundaries of the combustion chamber. The (reflected) waves cause flow fluctuations, which leads to a fluctuation in heat release rate after a time delay. This closes a feedback loop between the acoustic fluctuations and the heat release fluctuations, as shown in Fig. 1.1. The necessary, though not sufficient, criterion that must be met for the amplitude of fluctuations to increase and for the system to become unstable was first addressed by Lord Rayleigh in 1878 [13] and is known as the Rayleigh criterion: The energy is added to the acoustic field of the

system, when the heat release rate oscillations in a combustion chamber are in phase with pressure oscillations. The system, however, destabilizes only when the gain of acoustic energy in the combustor is greater than the acoustic losses a) due to dissipation processes, or b) through the system boundaries [14].

The flame/acoustic interaction can cause such large amplitudes of acoustic pulsations that the system can be damaged either by low-cycle fatigue (within days) or by high-cycle fatigue (within minutes). Thus, there is a substantial risk of damage to the combustor if the gas turbine is not turned down after surpassing a specific amplitude of high-frequency vibrations. Crack formation usually occurs in an area of high stress concentration due to shape, welded joints or cooling holes [15]. Exemplary images of combustors of industrial gas turbines damaged by high-frequency thermoacoustic instabilities are shown in Fig. 1.2.

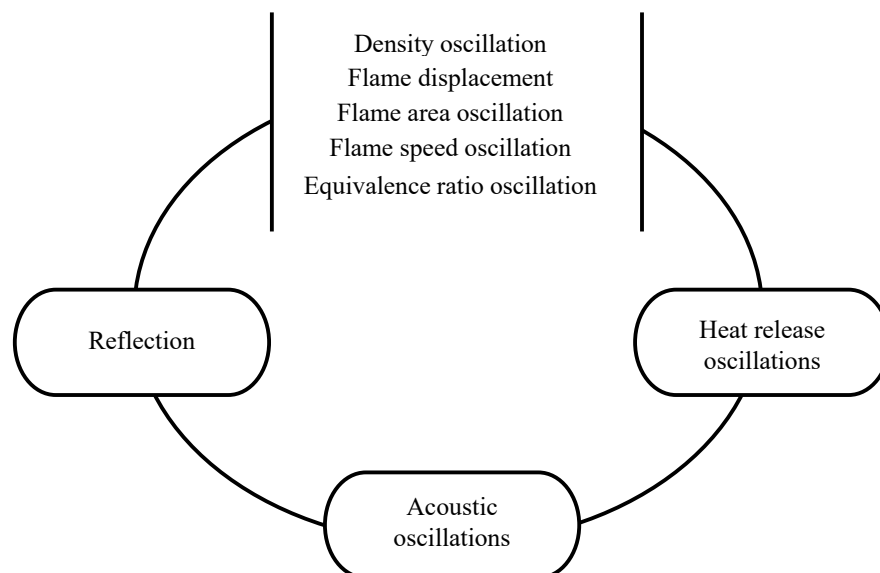


**Fig. 1.1** Thermoacoustic instability loop.

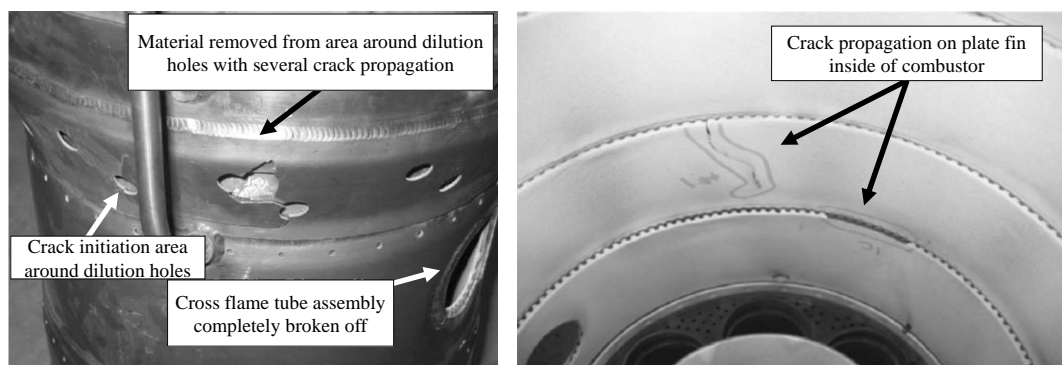


**Fig. 1.2** Combustors damaged by high-frequency thermoacoustic instabilities [15].

Thermoacoustic instabilities typically occur at frequencies near the resonance frequencies of the combustion chamber. The common acoustic modes in a combustor are

a) longitudinal, b) transverse radial and c) transverse azimuthal modes, which are illustrated in Fig. 1.3. For can combustors, thermoacoustic instabilities can be divided into three categories based on the acoustic mode shape, and the corresponding mitigation strategies: a) LFI: Low Frequency Instabilities, b) IFI: Intermediate Frequency Instabilities, and c) HFI: High Frequency Instabilities. The corresponding acoustic mode shapes at the LFI are often Helmholtz modes (bulk modes) and do not correspond to longitudinal acoustic modes of the combustion system. The mode shape of IFI normally matches one of the longitudinal Eigenmodes of the combustion chamber. The HFI modes have transverse components in addition to the longitudinal component.

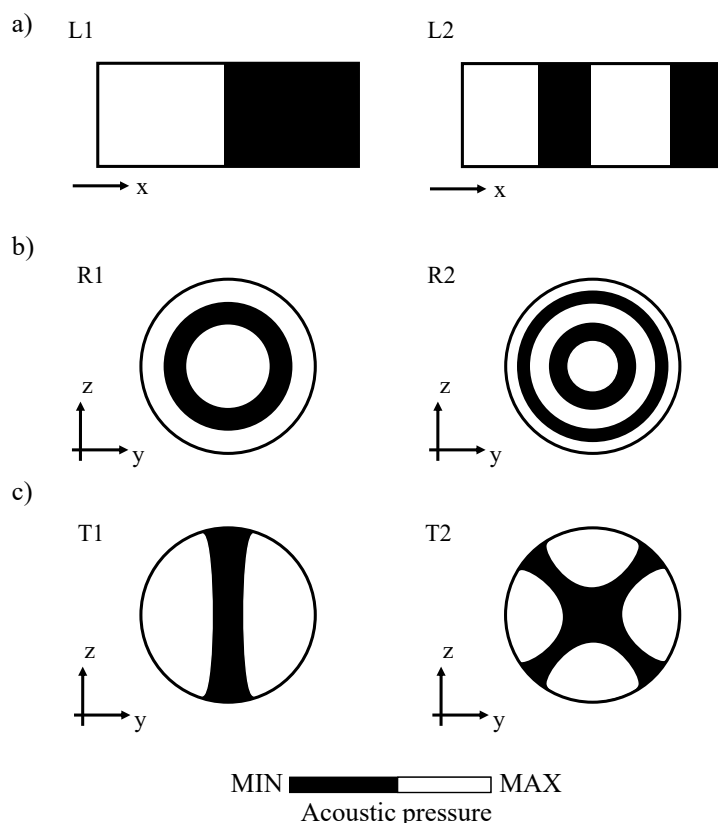


**Fig. 1.3** Sketches of a) longitudinal, b) transverse radial and c) transverse azimuthal acoustic modes.

The Rijke tube [16] is an example of a system that shows pure thermoacoustic longitudinal oscillations. It consists of a vertical tube and a heat source (a heated gauze), which is placed a quarter of the tube length from one end of the tube, as shown in Fig. 1.4. The experiment starts by heating the gauze with an external heat source. The heated gauze causes an upward flow by natural convection. Once the external heat source is removed, the tube begins to produce a loud sound at a frequency corresponding to the first longitudinal mode of the tube. The driving thermoacoustic mechanism could be explained as follows [17]: The acoustic pressure and velocity corresponding to the first longitudinal resonant mode of the tube are shown in Fig. 1.4. In the first half of the

acoustic cycle ( $0^\circ$  to  $180^\circ$ ), the upward flow velocity increases by the acoustic velocity (particle velocity) of the acoustic wave at the gauze position, improving heat transfer through convective processes with a time delay. During these phases, the acoustic pressure at the position of the gauze increases. In the second half of the acoustic cycle ( $180^\circ$  to  $360^\circ$ ), the direction of the acoustic velocity is reversed. The upward flow velocity decreases by the acoustic velocity of the acoustic wave at the gauze position. Therefore a decrease in heat transfer is expected. During these phases, the acoustic pressure is reduced in the position of the gauze. Based on this explanation, in the Rijke tube, the heat transfer rate oscillates preferentially with the pressure oscillations when the heat source is placed in the lower half of the tube, resulting in an increase in acoustic energy and acoustic pulsation based on the Rayleigh criterion.

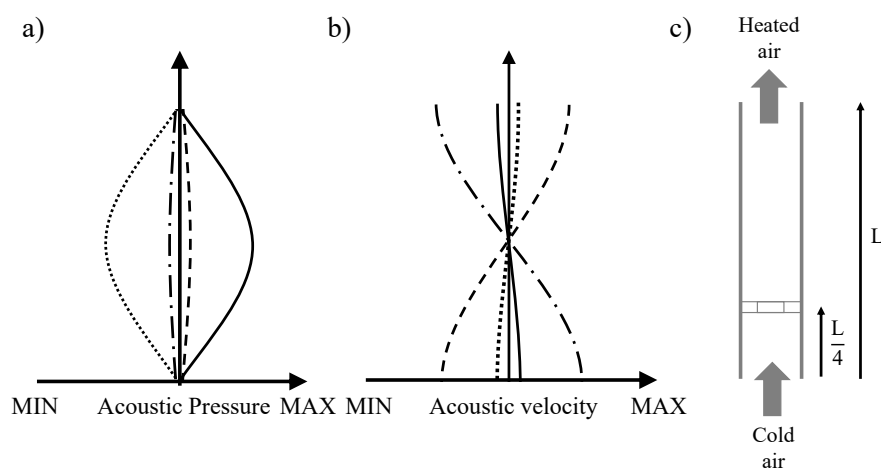


**Fig. 1.4** Distribution of a) acoustic pressure, b) acoustic velocity for the first axial natural mode of the tube and c) schematic of the Rijke tube.

### 1.1.1 Instability Mechanisms

In gas turbine combustion chambers, however, more complex driving mechanisms are involved than in the Rijke tube. In the following, mechanisms by which the heat release rate might pulsate in a combustion chamber are briefly outlined. It should be noted that in an industrial combustion chamber several driving mechanisms might exist simultaneously and even influence each other. The dominant mechanism might even alter concerning changes in operating conditions and frequency of instabilities.

#### *Flame/Vortex Coupling Mechanism*

Flame/vortex interactions are observed and addressed to be important in many thermostatically unstable systems [18, 19, 20, 21, 22, 23, 24]. The periodic shedding of vortex structures leads to a periodic extension of the flame area (e.g. by rolling up), which may lead to fluctuations in the heat release rate. When these fluctuations are

in phase with pressure fluctuations, thermoacoustic instabilities can be driven as described by the Rayleigh criterion. The shedding frequency is observed to be the same as the acoustic frequency prescribed by the acoustic resonance of the geometry in the self-excited systems [20] or the forcing frequency in the forced response studies [25]. Vortex shedding is observed in almost all unstable combustors, but it is still ambiguous whether these instabilities are responsible for the initiation of instabilities or only caused by thermoacoustic instabilities [26]. Venkataraman et al. [27] investigated experimentally thermoacoustic mechanisms of 500 Hz instabilities in a bluff-body stabilized dump combustor. In their premixed setup, they observed a significant interaction of vortex structures with the flame at the frequency of instabilities. They determined the flame area from the two-dimensional Chemiluminescence images and showed that the flame area oscillated in phase with the pressure, indicating the destabilizing impact of the flame/vortex interaction. Poinsot et al. [19] reported instabilities with a frequency of 530 Hz in a dump combustor. From Schlieren images, they observed that a vortex forms in each cycle, then grows in size and interacts with the flame. Comparing the Schlieren images with the phase averaged fields of the reaction rates, they indicated an increase in the reaction rate during this interaction. However, the heat release rate was observed to be maximum at the time, when the vortices from the adjacent jets interacted and enhanced the reaction rates. Thus, the authors concluded in their paper that the interaction of the neighboring vortices was the driving mechanism for the observed thermoacoustic instabilities. Rogers et al. [20] studied a V-shaped flame in a rectangular combustor, which showed high-frequency oscillations of 3800 Hz. They observed alternate vortex shedding from the flame holder's lips with the frequency of the instability. They explained the mechanism as follows: The transverse velocity forms a vortex, consisting of fresh mixture, and carries the generated vortex into the hot recirculation zone. The fresh mixture, which is periodically fed to the reaction zone by vortices, causes a periodically oscillating heat release rate with a time delay. The time delay results from the transport of the fresh mixture to the reaction zone, its mixing with the hot gas, and its ignition and combustion. If this time delay is in phase with the acoustic pressure, the Rayleigh criterion is fulfilled and instabilities can increase. Schwing et al. [21] investigated excitation mechanisms in a tubular single burner combustor with a premixed swirl flame. They observed alternate vortex shedding driven by the transverse acoustic velocity with a frequency of 3300 Hz. Based on their observation, they proposed the following mechanism: the acoustic transverse velocity forms pockets of combustion products in the unburned mixture, and these pockets will be transported with the mean flow and cause oscillations in the heat release rate further downstream.

### *Equivalence Ratio Coupling Mechanism (Fuel Time-Lag Mechanism)*

Another cause of heat release rate oscillations in combustors might be equivalence ratio fluctuations. These fluctuations can be generated due to the interaction of the acoustic waves, which reach the upstream fuel or air supply, and generate pockets of rich and lean mixtures. These pockets convect downstream and reach the flame, causing fluctuations in the heat release rate. When the resulting heat release rate oscillation is in phase with the pressure oscillation, energy is added to the acoustics of the system. Lieuwen et al. [28] developed a simple model based on the time delay between heat release rate and equivalence ratio oscillation to investigate the role of the equivalence ratio coupling mechanism. They considered two main time delays: a) a convective time delay, i.e. the time required for the pockets of the lean/rich mixture to reach the flame front, and b) a chemical time delay, i.e. the time it takes for the total heat release rate to follow the equivalence ratio oscillation. Based on the model, they proposed a stability chart showing regions of time lag where instabilities were possible. They compared the estimated time delays of several unstable experimental test cases and showed that most instabilities occurred in unstable regions of their stability chart, demonstrating the decisive destabilizing effect of the equivalence ratio mechanism. Lee et al. [29] experimentally investigated the validity of the time delay theory on a dump combustor with a swirl-stabilized flame for which pressure measurements, heat release rates and equivalent ratios were performed. In their atmospheric experiment, they first investigated the influence of variations of the mean equivalence ratio and the mean air mass flow rate on the instabilities of the system. The system tended to exhibit instabilities for a range of equivalence ratios between 0.6 and 0.7. An increase of the amplitude of oscillations was observed as the air mass flow rate was increased. For the operating conditions corresponding to the largest amplitude of fluctuations, they compared the measured equivalence ratio modulations to the heat release rate fluctuations and showed that the time-lag theory could explain the instabilities. However, they found that for their stable case, the time-lag criterion was also fulfilled. They argued that the time-lag model presents only a necessary condition, but not a sufficient condition, under which instability might occur. Schuermans et al. [30] investigated the causes of instabilities in an atmospheric swirl-stabilized flame of a full-scale gas turbine burner experimentally. The system was able to operate in a fully premixed and partially premixed mode. In the latter mode, a fluctuation of the equivalence ratio was expected. Their result showed a significant increase in the flame response when the equivalence ratio fluctuation was considered, indicating the destabilizing effect of the equivalence ratio coupling mechanism. Cho et al. [31] analytically studied the response of a laminar Bunsen-type flame, subjected to equivalence ratio perturbations using the G-Equation model. The equivalence ratio fluctuation was induced by the oscillation of the upstream

air mass flow rate, whereby the fuel mass flow rate remained fixed. They correlated the heat release rate oscillations to the oscillations of the enthalpy of reaction, the flame speed and the flame surface area. They showed that the flame response at low Strouhal number was mainly controlled by the oscillation of heat of reaction (directly correlated with the equivalence ratio) . Towards the higher Strouhal numbers, the contribution of the flame speed oscillations and the contribution of flame area oscillations were comparable with the contribution of the heat of reaction modulation. A similar study for a V-shaped flame [32] resulted in a more significant contribution of the flame speed oscillation to the heat release rate oscillation.

#### *Pressure/Density Coupling Mechanism*

The heat release rate of a flame is proportional to the density of the reactants. Pressure fluctuations in a combustion chamber result in an oscillation of the reactant density, which in turn causes an oscillation of the heat release rate. Hakim et al. [33] simulated the dynamics of a cryogenic flame in a scaled rectangular multi-injector combustor. The combustion chamber was forced to oscillate in the first transverse natural frequency with a pressure node (and simultaneously acoustic velocity node) in the midplane of the combustor. They found that the flame furthest from the midplane of the combustor (subjected to a largest amplitude of pressure oscillation) shows an oscillating heat release rate with the largest amplitude, indicating the destabilizing impact of the direct effect of pressure fluctuations on the heat release rate. Zellhuber et al. [34] proposed a theoretical model for the decomposition of the thermoacoustic source terms and used this model in a forced response simulation of a generic reheat combustor. They observed that the density fluctuation had a most significant contribution to the instabilities. Recently, Sharifi et al. [35] studied the response of a Bunsen-type flame subjected to high-frequency transverse acoustic pressure oscillation for a frequency range between 1000 to 5000 Hz. They analyzed the relative significance of different mechanisms to the thermoacoustic instabilities. For the flame positioned in the acoustic pressure anti-node and simultaneously acoustic velocity node, they identified the pressure/density interaction as the main destabilizing mechanism over all forcing frequencies.

#### *Pressure/Chemistry Coupling Mechanism*

The pressure/chemistry coupling mechanism involves the direct effect of the acoustic field on the fluctuation of the local flame speed and enthalpy of reaction, which in turn cause heat release rate oscillations. Schmidt et al. [36] studied numerically the response of a one-dimensional laminar premixed methane flame subjected to pressure oscillations with a frequency range between 50 to 3000 Hz. In the absence of other pathways through which the heat release rate could oscillate (e.g. flame surface

oscillation, equivalence ratio oscillation), they showed an in-phase oscillation of the heat release rate with the pressure, which proves the destabilizing effect of the pressure/chemistry coupling mechanics. They also found that the sensitivity of the heat release rate response to acoustic disturbances was increased by increasing the forcing frequency. More recently, Beardsell et al. [37] extended the previous study to large hydrocarbon fuel flames and observed comparable quantitative behaviour. Shreekrishna et al. [38] carried out an analytical investigation [39] on a 2D configuration to study the alteration of the contributions of different mechanisms leading to heat release rate response of a laminar premixed V-flame to axial acoustic oscillations. They derived a model to identify the effects of oscillation of density, flame surface area, enthalpy of reaction and the flame speed on the global heat release rate fluctuations. The flame speed was modified with equivalence ratio changes, stretch effects and direct pressure effects in their model. The effect of different mechanisms on the response of the flame was identified by excluding the response through other mechanisms. They showed that the heat release rate oscillations were controlled by the pressure/density mechanism at low frequencies. In contrast, the pressure/flame speed mechanism was dominant for high frequencies. For the frequency range from 2000 Hz to 4000 Hz, where high-frequency thermoacoustic instabilities usually occur in gas turbines, both mechanisms were relevant, with the pressure/density mechanism being slightly more significant. Recently, Sharifi et al. [35] proposed an algebraic model to consider the fluctuation of the flame speed due to acoustic pressure oscillation. They showed that considering the pressure sensitivity of flame speed in their forced response configuration increased the response of the flame for the high-frequency oscillations.

#### *Flame Stretch Coupling Mechanism*

The flame stretch can be altered by the velocity gradient along the flame surface and the curvature effects [8]. The local flame speed is known to be function of the local stretch [40, 41]. Fluctuations in flame stretch due to flow/acoustic fluctuations over the flame can therefore lead to fluctuations in flame speed, which in turn leads to fluctuations in the heat release rate. Wang et al. [42] investigated analytically the influence of local flame speed changes due to strain modulation. They considered a two-dimensional premixed V-shaped flame exposed to acoustic oscillations. They used the G-equation method and assumed constant enthalpy of reaction and fixed density of the mixture, allowing local flame speed changes to be only due to stretch effects. They showed that the oscillation of the burning velocity was negligible at the lower perturbation frequencies and become important at high frequencies (e.g., more than 4 kHz for a practical V-shaped flames). They also showed that the stretch modulation caused an in-phase oscillation of the heat release rate, which proves its destabilizing

character. More recently, Orchini et al. [43] investigated this effect for a conical flame, leading to similar results.

### *Flame Displacement Mechanism*

The Sattelmayer group [44, 45, 46, 47] studied the excitation mechanism in a tubular single burner combustor with a premixed swirl flame, which showed the first transverse acoustic mode with a frequency around 3300 Hz. They observed a synchronized up and down displacement of the flame with the pressure. The displacement of the flame due to the transverse oscillation was also observed in other studies [48, 33]. Based on this observation, they proposed a mechanism, termed the flame-displacement mechanism. Based on this mechanism, the acoustic transverse velocity shifts the flame to the region with higher pressure, so that the flame always releases heat at higher acoustic pressure amplitude, and thus the Rayleigh index is always positive. Although this mechanism is always present when the flame is subjected to transverse velocity oscillation, it might not be the main contribution to thermoacoustic instabilities of the flame. Hummel et al. [46] proposed a model for non-compact heat release rate oscillations due to the flame displacement and density oscillation (pressure/density mechanism). They performed two eigenvalue analyses, whereby they considered only the contribution of the flame displacement in the first analysis, and the contribution of the density oscillation to the oscillation of the heat release rate in the second. They solved the problems for the corresponding complex Eigenfrequencies associated with the observed first transverse mode in the experiment of the Sattelmayer Group. The comparison of the growth rates of each mechanism showed a more significant contribution of the pressure/density coupling mechanism. However, it was shown that the simultaneous presence of both mechanisms was necessary to achieve the unstable behavior of the experiment.

#### 1.1.2 Methods of Investigation

##### *Experimental Approaches*

Simplified or real geometries can be used to investigate thermoacoustic instabilities experimentally. Laboratory setups are mostly used to investigate the interaction of the flame with the imposed acoustic transverse wave. Mery et al. [49] designed a rectangular multi jet methane/liquid-oxygen combustor to investigate the driving and coupling mechanisms of high-frequency (1.8 - 3.2 kHz) instabilities. The combustion chamber ended into two outlet nozzles from which the exhaust gases were discharged. In order to excite the first transverse mode of the system, a rotating gear was used, which periodically blocked one of the two outlet nozzles at the desired frequency, so that the entire exhaust gas flow leaves from the other open outlet nozzle. The experimental rectangular single burner combustor of Lespinasse et al. [48] was equipped with two loudspeakers.

ers at the sides of the chamber to generate standing waves. The distance between the chamber walls could be modified to ensure the resonance at frequencies of 506 or 1012 Hz. The burner was also adjustable, so that the position of the flame could be varied concerning the position of the pressure anti-node. Measurements revealed significant differences in local and global flame response at various locations in the acoustic waveform.

Although the aforementioned experiments could improve the understanding of the flame/acoustic interactions, the most reliable information to aid the design of a robust combustor can be taken from self-excited thermoacoustic experiments. In the following Paragraphs, some experiments relevant for gas turbines with self-excited high-frequency oscillations are briefly presented:

a) *The Volvo Test Rig*

Sjunnesson et al. [18, 50] investigated the thermoacoustic behaviour of a bluff body stabilized propane flame in a rectangular combustor at Volvo in Sweden. The combustor was 0.24 m wide, 0.12 m high and 1.5 m long. The duct terminated into a circular plenum. The top and bottom walls of the combustor were water-cooled and the side walls were air-cooled, however, the temperature of the walls was not addressed. The air was mixed with propane, upstream of the inlet section. The turbulence was controlled by an upstream honeycomb. The honeycomb and the downstream plenum, which were vital for the acoustic reflection, were not clearly reported in the experiments. A triangular flame holder was used to stabilize the flame. The system operated in a stable regime for an operating condition with an air velocity of 17.3 m/s and an equivalence ratio of 0.61. High-frequency oscillation with a frequency of 1400 Hz was observed by increasing the velocity and equivalence ratio to 36 m/s and 0.72, respectively. A Schlieren image of the high-frequency instability can be seen in Fig. 1.5, indicating periodic symmetrical vortex shedding.



**Fig. 1.5** Schlieren image of periodic vortex shedding in Volvo test case [18].

b) *The Tubular Swirl-Stabilized Combustor of the Sattelmayer Group*

Schwing et al. [21, 44] investigated the excitation mechanism in an atmospheric self-excited single jet cylindrical combustor, with a premixed swirl stabilized natural gas flame. The combustor consisted of an upstream plenum, a swirler, a mixing tube,

an air-cooled quartz glass flame tube ( $D=156$  mm) and a water-cooled exhaust tube with the same diameter as the flame tube [51]. The preheated fuel and air were mixed in a pre-chamber and flowed through an Alstom-type swirler before flowing into the mixing passage and flame tube. The base plate of the combustor was equipped with five dynamic pressure sensors to capture the azimuthal mode. Mie-scattering images, PIV and  $\text{OH}^*$ -Chemiluminescence were used to measure density, local flow velocity and heat release, respectively. In the experiment, the swirl number, the preheating temperature and the mass flow rate were varied to investigate their influence on the occurrence of instabilities. For all operating conditions, it was found that first transverse instabilities were initiated by exceeding a critical equivalence ratio. The frequencies of the first radial mode were found to be between 2400 and 3400 Hz with an amplitude around 10 mbar. The critical equivalence ratio seemed to be a function of the preheating temperature, the air mass flow rate and the swirl number. The limit of the critical equivalence ratio was moved towards the leaner mixture by decreasing the swirl number, increasing the mass flow rate and decreasing the preheating temperature. The flame/vortex interaction and the flame displacement mechanism and density mechanism were proposed to be important mechanisms for the observed instabilities.

#### *c) Single-Jet Combustor of Purdue University (Viper-S)*

Buschhagen et al. [52, 53] designed a cylindrical single-jet combustor with a fully premixed natural gas jet flame at an elevated pressure of 7 bar, which was susceptible to high-frequency instabilities. The combustor consisted of an external pre-mixer, a cylindrical duct with a diameter of 40 mm and a cylindrical combustor with a diameter of 80 mm. By means of a choked orifice plate and a choked nozzle, the duct and combustion chamber were acoustically separated from the upstream and downstream devices, respectively. Thus, a well-defined acoustic boundary condition was provided. The experiment with an equivalence ratio of 0.72 and a pressure of 7.2 bar clearly introduced pressure oscillation at 360 Hz, corresponding to the first longitudinal mode of the combustor. A slight decrease in equivalence ratio and pressure of about 2% and 3%, respectively, resulted in the occurrence of high-frequency pressure fluctuations at a range between 4.8 to 6.5 kHz. The mode shape of the instabilities was, however, not experimentally addressed. Chemiluminescence images of  $\text{OH}^*$  clearly showed a periodic oscillation of the heat release rate at the upper and lower parts of the combustor. An effort was made to shed light on the driving mechanism of the instabilities. However, a simultaneously existing interaction of different complex acoustic modes with the flame made a clear investigation of the mechanism extremely difficult.

### *Numerical Approaches*

Large-eddy simulation (LES) is the most powerful, affordable tool available today for investigating combustion instabilities in technical combustion systems. LES is as-

sumed to be able to consider almost all thermoacoustic drive and damping mechanisms in a complex system. However, it should be considered that the reliability of LES in the investigation of thermoacoustic instabilities is clearly limited by the combustion model employed in the simulation. There are two main approaches for the use of LES to investigate thermoacoustic instabilities: a) self-excited approaches and b) forced response approaches.

The complete combustion chamber with the realistic acoustic boundary conditions must be investigated in the self-excited simulations [54]. All of the excitation and feedback mechanisms are present and the flame can interact with the three-dimensional thermoacoustic modes of the combustor. In forced response simulations, a reduced combustor geometry can be used [33, 55]. The acoustic fluctuations are imposed through perturbations prescribed on the boundaries. Thus, the interaction of an individual flame with acoustic waves under different acoustic frequencies and amplitudes can be investigated. However, in this method, the three-dimensional thermoacoustic behavior of the real combustor is neglected and the flame normally interacts with one-dimensional acoustic modes.

Different groups [56, 57, 58, 59] used self-excited approaches to investigate the high-frequency instabilities in the Volvo test rig. Ghani et al. [57] simulated a simplified configuration, where the acoustical effect of the honeycomb and the fuel injection were neglected. The combustor walls were assumed to be adiabatic. They used a third order compressible CFD code with the Sigma model [60] to model sub-grid turbulence structures. The inlet and outlet boundaries were assumed to be fully reflective, which differed drastically from the experiment. To model combustion, they used a reduced two-step mechanism for propane/air combustion. Their results showed a pressure fluctuation with a frequency of 1360 Hz (experiment: 1400 Hz), which corresponds to the first longitudinal and second transverse mode of the combustor. Although they could capture the symmetric flow pattern observed in the experiment (see Fig. 1.5), they stated that this behaviour was due to the longitudinal part of the acoustic mode. It should be noted that the mode shape was not reported in the experiment and that the symmetric flow pattern could be due to a purely longitudinal mode with a frequency of 1.4 kHz, as reported by other authors [61]. This underlines how the lack of information in experiments can lead to ambiguous results.

### *Low-Order Methods*

In this approach, the complete combustion system is modeled as a network of acoustic elements. Acoustic waves are superimposed on the mean properties of each element. Acoustic transfer matrices connect elements. The interaction of the acoustic wave with the flame can be characterized by a flame transfer function (FTF) [62] or a flame de-

scribing function (FDF) [63]. Low-order models solve for the complex Eigenfrequencies, from which the growth rate of instabilities can be determined [64]. The main drawback is that the reliability of this method is restricted to the model representing the flame/acoustic interactions and the acoustical damping of the system. Low-order methods are extensively employed to investigate the low-frequency instabilities with longitudinal acoustic mode shapes under the assumption of a compact flame with respect to acoustic waves [65, 66, 67]. Recently, investigations are performed [68, 69] employing a distributed FTF to study high-frequency instabilities.

## 1.2 Motivation and Overview of the Present Work

An improved understanding of the thermoacoustic mechanism is indispensable in designing a robust combustor for a desired operating condition. Therefore, an extensive set of information about the flow, flame and acoustical fields is required from experiments. The experimental data of a full-scale test rig showing thermoacoustic instabilities are hardly suitable to understand the thermoacoustic instability mechanisms or to use them as validation case, due to the following issues:

1. The thermoacoustic instabilities observed in such a device are the undesirable side-product of the full-scale test rig. The test facility must be turned off immediately after exceeding a quite low level of thermoacoustic instabilities. As a result, the operating conditions under which instabilities have occurred, are not stationary and not well defined.
2. The experimental data are limited to pressure signals in one or two positions, so that the acoustic mode shape can hardly be determined.
3. The acoustic boundary conditions of the test rig are not exactly addressed, which makes them a non-reproducible test case.
4. Simulations of large combustion chamber geometries covering the entire upstream and downstream parts of the combustion chamber are too complex and costly.

More detailed and reliable experimental data can be obtained from lab-scale test cases and can be used as a starting point to investigate these type of instabilities. However, there is a lack of simple experiments with acoustically well-defined boundary conditions relevant for state-of-the-art stationary gas turbines to study thermoacoustic instabilities. The available test cases were mentioned previously and were briefly explained. It should be noted that the manner of flame stabilization (e.g. swirl stabilized, bluff body stabilized, jet-stabilized) crucially affects the thermoacoustic mechanisms,

through which the instabilities can arise [70]. Thus, a swirl-stabilized flame is not necessarily an appropriate test case to study the flame dynamics of a jet-stabilized flame, which is the characteristic stabilization method in the combustion chamber of the new generation of Siemens heavy-duty gas turbines. Although the recently performed experiment of the "Viper-S" combustor at Purdue University [52, 53] could be a starting point, there are some doubts about the instabilities in this combustor: There was no operating condition found in the experiment, for which the system was in a stable regime. This would raise the question, if the observed instabilities occurred only due to the acoustically closed inlet and outlet, leading to minimizing the acoustic fluxes through the combustor boundaries and to an accumulation of the acoustic energy in the system for any level of flame/acoustic coupling.

In order to overcome the problems of previous experiments, the present work attempted to develop a simple and suitable atmospheric experiment on the laboratory scale, which can be used as a valuable test case for the analysis and modelling of thermoacoustic oscillations. LES was used to investigate high-frequency thermoacoustic instabilities and support the design of the test case. Forced response simulations were firstly conducted to identify and quantify underlying driving mechanisms of high-frequency thermoacoustic instabilities on a single jet flame. The flame was subjected to transverse acoustic modulation to reproduce two possible flame/acoustic interaction scenarios characteristic of the high-frequency instabilities in can combustion chambers. A budget analysis method was introduced to identify the main mechanism in each scenario and to understand how it was affected by the frequency of the instabilities. Finally, the state in which the flame was most susceptible to thermoacoustic instabilities was determined.

Based on the lessons learned from the forced response investigations, an effort was made to design a simplified combustion chamber on a laboratory scale that fulfilled the following requirements:

1. Use of atmospheric combustion to reduce the cost of the experiment.
2. Instabilities with a frequency range that is often observed in real gas turbines.
3. Reproducible high-frequency instabilities.
4. Well-defined acoustic boundary conditions.

In the forced response simulations, the highest destabilization was observed, when the flame was positioned in a pressure anti-node. To reproduce such a flame/acoustic interaction, the flame was positioned on the centerline of a cylindrical chamber. Given the axisymmetric behavior of a jet flame, it could generally be assumed that the acoustic radial Eigenmode of the cylindrical combustion chamber could be more easily excited. Thus the flame was positioned in the acoustic pressure anti-node. The diameter of the

cylindrical combustion chamber was chosen such that the first radial mode had a frequency of 3 kHz, a frequency, which is often observed in real gas turbines exhibiting thermoacoustic instabilities. The inlet and outlet of the system, corresponding to the position of acoustic boundaries, were set far away from the flame, to ensure there is no interaction with the flame. The equivalence ratio for the atmospheric combustion was modified until strong high-frequency oscillation was observed. The complexity of the test case was then increased in the design simulations to allow a feasible experiment with realistic wall heat transfer, upstream flow conditions and fuel mixing. An important finding from the design simulations was that for a given equivalence ratio, the largest amplitude of high-frequency acoustic instabilities was observed when the simulation was performed with adiabatic combustion chamber walls. Lowering the temperature of the combustor wall towards an experimentally feasible wall temperature reduced the amplitude of the instabilities. However, the mode shape remained untouched. When the temperature dropped below a critical temperature, the system stabilized. Further numerical investigations showed that it was possible to shift the critical wall temperature towards a colder temperature by increasing the equivalence ratio.

Finally, a configuration was determined which was susceptible to thermoacoustic oscillations and fulfilled the above requirements. This configuration was studied experimentally on the Siemens atmospheric test facility. The experiment was performed for different air mass flow rates and equivalence ratios. For a given air mass flow rate, thermoacoustic instabilities of the first radial mode were identified when a critical equivalence ratio was exceeded. A further increase of the equivalence ratio led first to an increase and then to a decrease in the amplitude of the high-frequency oscillations. The largest amplitude was observed at an equivalence ratio of a slightly lean mixture. By increasing the air mass flow rate, the equivalence ratio, at which the largest amplitude was observed shifted towards the leaner mixtures. It was also observed that an increase in the air mass flow rate led to a general increase in the amplitude of the thermoacoustic instabilities.

The predictive capability of the numerical method concerning thermoacoustic instabilities was then investigated. Two simulations were performed with the geometry used in the experiment. Both the predictive capability with respect to high-frequency thermoacoustics and the prediction of stable combustion were considered with the operating state corresponding to unstable and stable combustion, respectively. It could be shown that CFD was able to predict the results with a satisfying agreement for both states.

Notably, the amplitude of the high-frequency instabilities in the experiment was significantly smaller compared to the design simulations performed before the experiment. The main difference between these design simulations and the experiment was the treatment of the wall temperatures. The design simulation was performed with uni-

form combustion chamber wall temperatures. In the experiment, it was observed that the walls of the cylindrical combustion chamber around the base plate were relatively cold and became hotter towards the end of the combustion chamber. In order to investigate the influence of the wall temperature, a further simulation was carried out, applying the operating condition corresponding to the unstable operating point from the experiment. For this simulation, however, it was assumed that the combustion chamber wall temperature is uniform. The wall temperature value was set by averaging the temperatures measured in the experiment over the combustion chamber. The simulation showed a significantly higher oscillation amplitude of high-frequency instabilities for this case. This simulation can give an important indication why experiments on laboratory scale are less susceptible to high-frequency thermoacoustic instabilities than experiments on a full-scale test rig. Even though experiments in full-scale test rigs have a significantly higher energy density in the combustion chamber, the combustion chamber walls are well coated so that less energy is lost from the combustor wall. The test cases on the laboratory scale normally use optically accessible walls that are excessively cooled. Our study shows that excessive cooling of the combustion chamber walls can lead to the suppression of high-frequency thermoacoustics. The critical influence of the wall temperature should therefore be considered for the design of an unstable case in the future.

In terms of the development of a stable combustor, a method for suppressing the thermoacoustic instabilities was suggested in this work based on observations of the impact of wall temperature on the instabilities. It was shown that replacing the cylindrical combustor with a conical combustor resulted in the unstable system becoming stable. These results proved that the design of the conical combustor can be considered as a damping method for high-frequency instabilities with radial modes. However, in order to make a general statement, further evidence and further investigations are required.



## CHAPTER 2

### Theory

The Navier-Stokes equations are employed for the mathematical description of fluid dynamics. This set of nonlinear partial differential equations contains the conservation equations for mass, momentum, energy and species, presented in this section. The remainder of this section is followed by an introduction to the characteristics of turbulent flow and combustion. Finally, the theoretical background of linear acoustics is presented.

#### 2.1 Governing Equations

Transport equations for mass, momentum, total enthalpy and species can be used to describe the development of a viscous and compressible reacting flow, which are given below [64]:

$$\frac{\partial \rho}{\partial t} + \frac{\partial(\rho u_i)}{\partial x_i} = 0 \quad (2.1)$$

$$\frac{\partial(\rho u_i)}{\partial t} + \frac{\partial(\rho u_i u_j)}{\partial x_j} = -\frac{\partial p}{\partial x_i} + \rho g_i + \frac{\partial \tau_{ij}}{\partial x_j} \quad (2.2)$$

$$\frac{\partial(\rho h)}{\partial t} + \frac{\partial(\rho u_i h)}{\partial x_i} = \frac{\partial p}{\partial t} + u_i \frac{\partial p}{\partial x_i} - \frac{\partial q_i}{\partial x_i} + \tau_{ij} \frac{\partial u_i}{\partial x_j} + \dot{S} + \rho g_i \sum_{K=1}^{N_s} Y_K V_{K,i} \quad (2.3)$$

$$\frac{\partial(\rho Y_K)}{\partial t} + \frac{\partial(\rho u_j Y_K)}{\partial x_j} = \frac{\partial}{\partial x_j} \left( \frac{\mu}{Sc_K} \frac{\partial Y_K}{\partial x_j} \right) + \dot{\omega}_K \quad (2.4)$$

In the above equations  $\rho$ ,  $u_i$ ,  $p$ ,  $\tau_{ij}$ ,  $h$ ,  $Y_K$ ,  $\mu$  and  $Sc_K$  indicate the density, the  $i$ -th component of the velocity vector, the thermodynamic pressure, the stress tensor, the sum of sensitive enthalpy and chemical enthalpy per unit mass, the mass fraction of the species  $K$ , the viscosity of the gas mixture and the Schmidt-number, respectively. The first and second term on the right hand side (RHS) of the momentum equation, Eq. 2.2, represent the pressure gradient and the body forces due to gravitation, while the last term depicts the viscous forces. For a Newtonian fluid, the viscous stress tensor  $\tau_{ij}$  can

be written as follows:

$$\tau_{ij} = \mu \left( \frac{\partial u_i}{\partial x_j} + \frac{\partial u_j}{\partial x_i} \right) - \frac{2}{3} \mu \frac{\partial u_k}{\partial x_k} \delta_{ij} \quad (2.5)$$

In Eq. 2.5, the Kronecker Delta  $\delta_{ij}$  is 1 for  $i = j$ , and 0 otherwise. In the RHS of Eq. 2.3 the enthalpy flux  $q_i$  can be expressed according to the Fourier law considering the diffusion of species with different enthalpies  $h_K$  and diffusion velocities  $V_K$  as follows:

$$q_i = -\lambda \frac{\partial T}{\partial x_i} + \rho \sum_{K=1}^{N_s} h_K Y_K V_{K,i} \quad (2.6)$$

In the above equation,  $\lambda$  represents the thermal conductivity. The volumetric source term  $\dot{S}$  in Eq. 2.3 is an additional source term (e.g. to consider ignition) and must not be considered to be equivalent to the heat released from the combustion process. In the species conservation equation, Eq. 2.4, the first and second terms on the RHS express diffusion fluxes and the consumption rate, which together represent the total rate of change of a species  $K$ . The temperature dependent dynamic viscosity of the ideal gas mixture in the above equations can be determined according to the Sutherland model using a Sutherland coefficient  $A_s$  and a Sutherland temperature constant  $T_s$  as [71]:

$$\mu(T) = \frac{A_s \sqrt{T}}{1 + T_s/T} \quad (2.7)$$

## 2.2 Turbulence Theory

Navier–Stokes equations are valid for both laminar and turbulent flows. In the momentum equation (Eq. 2.2), the inertial term  $M_{ij} = \rho u_i u_j$  contributes to turbulence structures, while the viscous term  $\tau_{ij}$  tends to suppress them. The Reynolds number  $Re$  defines the ratio of inertial forces to viscous forces, and reads:

$$Re := \frac{\rho u L}{\mu} \quad (2.8)$$

In the above equation,  $L$  refers to a characteristic length of the system. When the Reynolds number surpasses a crucial value, the flow is classified as turbulent, as is the case in practically every gas turbine. Turbulent flows are characterized by time-dependent three-dimensional "chaotic" velocity fluctuations, which are superimposed on the time-averaged velocity.

### 2.2.1 Turbulent Length and Time Scale

In the case of a turbulent flow, there are structures (eddies) of different sizes. The largest eddies are of the size of an integral length scale, comparable to the system's characteristic length. The smallest eddies, with a length scale known as the Kolmogorov length scale  $\eta$ , are determined by the viscosity of the fluid and the rate of dissipation. The interaction time of the eddies with the flow is described for the largest eddies by the turbulence integral time scale  $\tau_t$  and for the smallest eddies by the Kolmogorov time scale  $\tau_k$ . Based on the concept of the turbulent energy cascade [72], the largest eddies transfer kinetic energy to smaller eddies, and this continues until the kinetic energy of the turbulence is dissipated into heat. A conceptual representation of the energy spectrum of eddies of different sizes, which are present in a turbulent flow, is illustrated in Fig. 2.1. The figure shows a log-log plot of the turbulent kinetic energy  $E(\kappa)$  versus the wavenumber  $\kappa$  and can be divided into three regions [73]: a) the energy-containing region with the largest eddies, which contains most of the turbulent energy, b) the inertial sub-region, in which the energy is transferred at a constant rate from the medium-sized eddies to smaller eddies, and c) the viscous region, in which the energy is dissipated into heat. In the inertial sub-region, the turbulent kinetic energy depends on the wavenumber  $\kappa$  and the dissipation rate  $\epsilon$ , the rate at which kinetic energy of the smallest eddies is converted into heat. Dimensional analysis can be used to obtain the turbulent kinetic energy density in the inertial region as in Eq. 2.9 [74]. In this equation,  $\mathcal{C}$  represents the universal Kolmogorov constant and is equal to 1.5.

$$E(k) = \mathcal{C} \epsilon^{2/3} k^{-5/3} \quad (2.9)$$

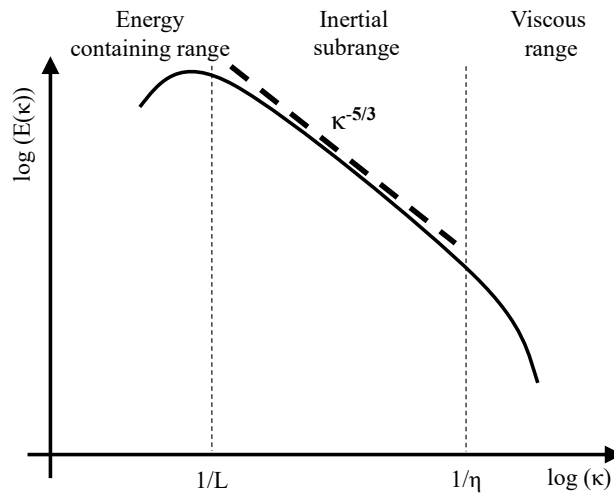
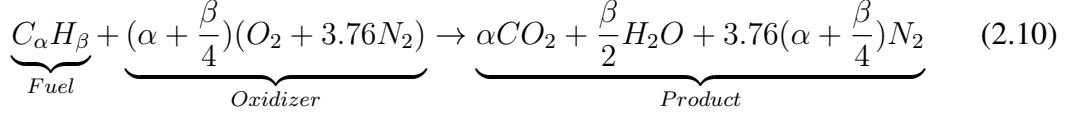


**Fig. 2.1** Sketch of Kolmogorov energy spectrum for turbulent flows [75].

## 2.3 Combustion Theory

Combustion is a chemical exothermic reaction between an oxidant and a fuel. In terms of a global, irreversible equilibrium reaction of a hydrocarbon fuel  $C_\alpha H_\beta$  [76], combustion can be described as follows:



An indicator for the mixture composition can be given by the equivalence ratio. The equivalence ratio of a system is defined as the ratio of the fuel-oxidizer ratio to the stoichiometric fuel-oxidizer ratio:

$$\phi = \frac{(\dot{m}_{\text{fuel}}/\dot{m}_{\text{oxidizer}})}{(\dot{m}_{\text{fuel}}/\dot{m}_{\text{oxidizer}})_{st}} \quad (2.11)$$

In Eq. 2.11,  $\dot{m}_{\text{fuel}}$  and  $\dot{m}_{\text{oxidizer}}$  are the mass flow rates of fuel and oxidizer, respectively. The stoichiometric fuel-oxidizer ratio for the combustion of general hydrocarbon can be estimated from the molar weight of fuel  $M_{\text{fuel}}$  and oxidant  $M_{\text{oxidant}}$  as follows:

$$\left(\frac{\dot{m}_{\text{fuel}}}{\dot{m}_{\text{oxidizer}}}\right)_{st} = \frac{M_{\text{fuel}}}{\left(\alpha + \frac{\beta}{4}\right)M_{\text{oxidizer}}} \quad (2.12)$$

### 2.3.1 Chemistry Description

#### *Detailed Chemistry*

The global reaction, as outlined above in Eq. 2.10, is the result of a large number of elementary reactions occurring at the molecular level. An example for a detailed mechanism to describe the combustion of small hydrocarbons is the GRI-3.0 mechanism [77], which includes 325 reactions and 53 species. A coupled set of elementary reactions for a system involving  $N_s$  species and  $N_r$  reactions can be written in the general form [78]:

$$\sum_{i=1}^{N_s} \nu'_{ij} \Psi_i \xrightleftharpoons[r_b]{r_f} \sum_{i=1}^{N_s} \nu''_{ij} \Psi_i \quad \text{for } j = 1, \dots, N_r \quad (2.13)$$

In the above equation,  $\nu'_{ij}$  and  $\nu''_{ij}$  are the stoichiometric coefficients. These coefficients indicate the number of molecules of the species  $\Psi_i$  involved in the reaction  $j$ . The reaction rates in Eq. 2.13, in forward and backward direction are represented by  $r_f$  and  $r_b$  respectively. In order to investigate reactive flows using detailed chemistry, the transport equation (Eq. 2.4) must be solved for each species. The source term  $\dot{\omega}_k$  for the individual equations is the sum of the production rates of the species  $\Psi_i$  in all elementary reactions [64]. The large number of transport equations to be solved makes the use

of detailed mechanisms for the simulation of combustion in a technical configuration prohibitively expensive and time-consuming. Various strategies for the simplification of chemical reaction mechanisms are presented in order to reduce the required effort (e.g. skeletal mechanism [79], globally reduced mechanism [80], analytically reduced mechanism [81] and tabulated chemistry [82]), which do not reproduce the chemical accuracy of the detailed mechanisms, but are generally able to reflect the essential properties of the flame.

### *Skeletal Mechanism*

Skeletal mechanisms are generated by reducing detailed mechanisms. The species and reactions that do not contribute to the prediction of the desired chemical quantities are simply removed from the mechanism. Different techniques for the generation of skeletal mechanisms are described (for an overview see e.g. the textbook of Tura'nyi and Tomlin [83]), including genetic algorithm-based methods [79]. Genetic algorithm-based methods are evolutionary and iterative algorithms for deriving skeletal mechanisms. The starting point for this method is the detailed reference mechanism as an initial solution followed by selection, crossover and mutation steps. The ability of each solution at every generation is evaluated to fulfill the desired criteria (e.g. flame speed, temperature profile, and the number of reactions) for the calculation of the reactive case (e.g. laminar flame). In each generation, the best solutions are selected to generate a new set of children (reduced mechanisms). The iteration process is repeated until the overall desired criteria are met. The final reduced mechanism may need to be further optimized by altering its reaction rate coefficients to match the correct overall behavior of the detailed mechanism [84].

### *One Step Chemistry*

A widely used assumption to greatly reduce the number of species and thus the number of equations to be solved is the description of the entire chemical mechanism by a single reaction:



An empirical expression can be used to describe the reaction rate. The reaction rate  $\dot{\omega}_F$  for this equation is then described by the Arrhenius law:

$$\dot{\omega}_F = -A\rho^{(\alpha+\beta)}Y_F^\alpha Y_O^\beta \exp\left(\frac{T_A}{T}\right) \quad (2.15)$$

The reaction order of the oxidizer and reactants are denoted by  $\alpha$  and  $\beta$ . The reaction parameters occurring in Eq. 2.15 are to be defined either experimentally or analytically

to determine the reaction rate.

### 2.3.2 Combustion Mode

#### *Premixed Combustion (Laminar)*

Premixed combustion is realized by supplying a uniform mixture of oxidant and fuel into the reaction zone. The combustion of the mixture is limited to the flammability limit of the fuel and can only exist for a certain range of equivalence ratios  $\phi$ . The combustion appears in a front that separates the unburned mixtures (from the burned mixtures). The front propagates normal to itself at a certain speed, the so-called laminar flame speed, in the direction of the unburned mixture. Premixed combustion is often characterised by low emissions of pollutants and uniform temperature combustion.

Two general definitions of flame velocity may be used [64]: a) the displacement speed  $S_d$ , which is based on the kinematic definition and measures the velocity of any iso-surface (e.g. temperature iso-surface) with respect to the flow, and b) the consumption speed  $S_c$ , which is based on the reaction rates  $\dot{\omega}$  and can be expressed as integral of the reaction rate along the flame front. The displacement speed is a local definition and varies across the flame front, while the consumption speed is a global quantity. The displacement speed at the reaction side and the global consumption speed are equivalent for a planar laminar unstretched premixed flame and are referred to as the laminar flame speed  $S_l$ . For simple chemistry (one-step reaction with the assumption of the unity Lewis number), a laminar flame thickness can be estimated based on the value of the temperature in the fresh mixture  $T_f$  and in the burnt mixture  $T_b$  and its gradient along with the flame normal coordinate  $n$  [85]:

$$\delta_L = \frac{T_b - T_f}{\max(|\frac{\partial T}{\partial n}|)} \quad (2.16)$$

#### *Premixed Combustion (Turbulent)*

Turbulent premixed combustion results from interactions between the flame front and the turbulent eddies with different sizes (from the integral length scale  $l_t$  to the Kolmogorov length scale  $\eta$ ) and different characteristic speeds (from the integral fluctuation velocity  $u'$  to the Kolmogorov velocity scale  $u_k$ ). The corresponding time scales can be estimated from the characteristic speeds and length scales as, for the integral time scale  $\tau_l = l_t/u'$  and for Kolmogorov time scale  $\tau_\eta = \eta/u_k$ . On the other hand, combustion may be expressed by a chemical time scale  $\tau_c$ , which can be estimated as the time it takes for the flame to propagate over a distance equal to its own thickness [86]:

$$\tau_c = \frac{\delta_L}{S_l} \quad (2.17)$$

Borghgi [87] and Peters [75] discussed this interaction qualitatively in depth and proposed regime diagrams. Here, we adopt the notes and assumptions of Peteres and discuss his proposed combustion regimes. Two non-dimensional numbers can describe the combustion regimes: a) the Damköhler number  $Da$ , being specified for the largest vortices and b) the Karlowitz-number  $Ka$ , being specified for the smallest eddies and read [75]:

$$Da = \frac{\tau_l}{\tau_c} \quad \text{and} \quad Ka = \frac{\tau_c}{\tau_\eta} \quad (2.18)$$

Four different regimes for turbulent combustion are shown in Fig. 2.2: a) the wrinkled flamelet regime ( $Da \gg 1$ ,  $Ka < 1$ ,  $u'/S_l < 1$ ), in which the flame thickness is smaller than the Kolmogorov length scale. This leads to a situation in which the flame surface becomes slightly wrinkled when interacting with the vortices; b) the corrugated flamelet regime ( $Da \gg 1$ ,  $Ka < 1$ ,  $u'/S_l > 1$ ), in which the flame surface is more wrinkled. The interaction of eddies and the flame surface causes the flame to roll up, creating pockets of similar size to the eddies; c) the thin reaction zones regime ( $Da > 1$ ,  $1 < Ka < 100$ ), where the flame is thicker than the smallest eddies. The Kolmogorov sized eddies can interact with the preheat zone of the flame and enhance the thermal diffusion. In this regime, the reaction zone, which is thinner than the Kolmogorov length scale, is not altered by the eddies; and finally d) the broken reaction zones regime ( $Da < 1$ ,  $Ka > 100$ ), where the reaction zone is thinner than the smallest eddies: the smallest eddies disturb the reaction zone and alter the thermal diffusion and heat transfer rate.

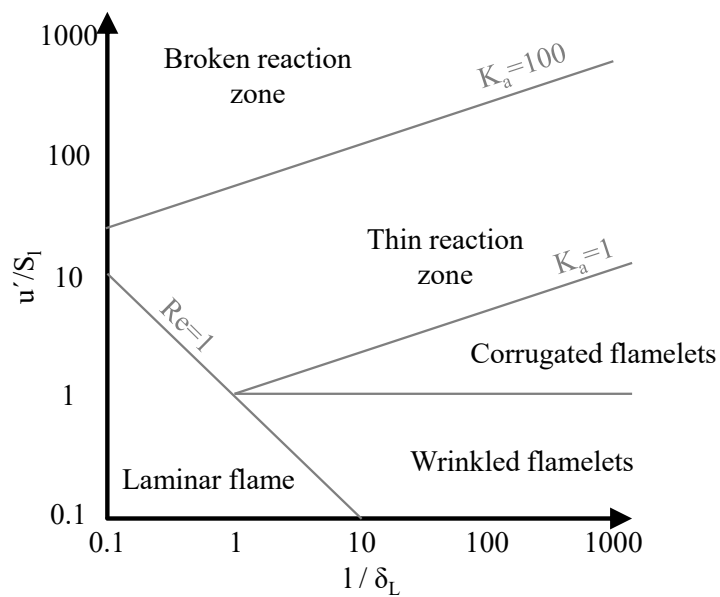


**Fig. 2.2** Turbulent combustion regimes [75].

The structure of the flame element in the wrinkled flamelet regime and in the the corrugated flamelet regime can be linked to the laminar flame structure. However, the flamelet assumption does not apply to the broken reaction zone regimes.

In the flamelet regimes the flame front is wrinkled by turbulent eddies. This leads to an increase in the effective flame area. It can be assumed that the front propagates with the laminar flame speed  $S_l$  and the increased heat release rate is then captured by the wrinkled turbulent flame surface  $A_T$ . From the modeling point of view, the turbulent flame can be seen as a front with a faster propagation speed. This propagation speed is termed as the turbulent flame speed  $S_T$ . The turbulent flame speed is equal to the laminar flame speed, multiplied by the ratio between the wrinkled instantaneous flame surface  $A_T$  and the laminar flame surface  $A_l$  [64]:

$$S_T = S_l \frac{A_T}{A_l} \quad (2.19)$$

### *Non-Premixed Combustion*

In non-premixed combustion, fuel and oxidant are not mixed before combustion. The reaction zone occurs at the locations where the stoichiometric conditions persist. Contrary to the premixed flame, the diffusion flame can occur at any oxidant to fuel mass flow rates ratio. Compared to premixed flames, the diffusion flame has a lower burning rate and higher local peak temperatures. The local mixing state is described by the mixture fraction  $Z$ . The mixture fraction, in a two-feed system in which fuel stream with a mass flux  $\dot{m}_1$  is mixed with oxidizer stream with a mass flux  $\dot{m}_2$ , may be defined as:

$$Z = \frac{\dot{m}_1}{\dot{m}_1 + \dot{m}_2} \quad (2.20)$$

The mass fraction of fuel in the mixture  $Y_{F,u}$  is proportional to the mass fraction of fuel in the fuel stream  $Y_{F,1}$  and reads:

$$Y_{F,u} = Y_{F,1} Z \quad (2.21)$$

Similarly, the mass fraction of the oxidizer in the mixture  $Y_{O_2,u}$  is defined using the mass fraction of oxidizer in the oxidizer stream  $Y_{O_2,2}$  and reads:

$$Y_{O_2,u} = Y_{O_2,2} (1 - Z) \quad (2.22)$$

Considering the relation between mass fractions of oxidizer and fuel which can be written as:

$$\frac{dY_{O_2}}{\nu'_{O_2}} = \frac{dY_F}{\nu'_F} \quad (2.23)$$

And integrating Eq. 2.23 between the initial unburnt state and any subsequent state leads to the well-known coupling function as follow:

$$\nu Y_F - Y_{O_2} = \nu Y_{F,u} - Y_{O_2,u} \text{ where } \nu = \frac{\nu'_O 2 W_{O_2}}{\nu'_F W_F} \quad (2.24)$$

Inserting Eqs. 2.21 and 2.22 into Eq. 2.24 one obtains the mixture fraction as a function of the mass fractions of the fuel and the oxygen and reads [78]:

$$Z = \frac{\nu Y_F - Y_{O_2} + Y_{O_2,2}}{\nu Y_{F,1} + Y_{O_2,2}} \quad (2.25)$$

## 2.4 Acoustic Theory

The flow variables  $p$ ,  $u$ ,  $\rho$  in a laminar flow can be decomposed into their mean and acoustic values as:

$$\begin{aligned} p(\mathbf{x}, t) &= p_0(\mathbf{x}) + p_1(\mathbf{x}, t) \\ U(\mathbf{x}, t) &= U_0(\mathbf{x}) + U_1(\mathbf{x}, t) \\ \rho(\mathbf{x}, t) &= \rho_0(\mathbf{x}) + \rho_1(\mathbf{x}, t) \end{aligned} \quad (2.26)$$

In the previous equations,  $\mathbf{x}$  is the local coordinate and  $t$  is the time. The indices 0 and 1 denote the mean and acoustic values, respectively. Substituting the acoustic variables into conservation equations for mass and momentum (Eqns. 2.1 and 2.2), linearizing the equations over their mean values, and combining them, one obtains the wave equations in an isotropic, non-reactive gas. The one-dimensional acoustic wave equation may accordingly be written as [88]:

$$\frac{\partial^2 p_1}{\partial x^2} - \frac{1}{a_0^2} \frac{\partial^2 p_1}{\partial t^2} = 0 \quad (2.27)$$

In the above equation,  $a_0$  denotes the speed of sound and is defined for a perfect gas with the gas constant  $R'$  and the specific heat capacity  $\gamma$  as:

$$a_0 = \sqrt{\gamma R' T} \quad (2.28)$$

In the frequency domain, a harmonically fluctuating (e.g. sine overlay) quantity,  $g_1(x, t)$ , is defined by its complex amplitude  $\hat{g}$ , and angular frequency  $\omega$ , through  $g_1(x, t) = \Re\{\hat{g}(x)e^{-j\omega t}\}$ , where  $\Re\{\}$  denotes the real part of a complex value. This representation can be used to separate the spatial and temporal variation of the fluctuations. Assuming that acoustic pressure oscillates harmonically, the one-dimensional acoustic wave equation can then be reformulated in the frequency domain by substitut-

ing  $p_1 = \Re\{\hat{p}_1 e^{-j\omega t}\}$  into Eq. 2.27 to obtain the following equation:

$$\frac{\partial^2 \hat{p}}{\partial x^2} - k^2 \hat{p} = 0 \quad (2.29)$$

In Eq. 2.29, the wavenumber is given by  $k = \omega/a_0$ , which is a measure for the number of waves per unit of length. The general solution of the wave equation (Eq. 2.27) is the superposition of a forward travelling wave and a backward travelling wave. The one dimensional solution of Helmholtz equation 2.29 in time can be expressed as [88]:

$$p_1 = \underbrace{A^+ e^{i(kx - 2\pi ft)}}_{\text{forward traveling wave}} + \underbrace{A^- e^{-i(-kx - 2\pi ft)}}_{\text{backward traveling wave}} \quad (2.30)$$

The amplitudes of the forward and backward traveling waves in the previous equation are given by  $A^+$  and  $A^-$ . The frequency of the wave is denoted by  $f = \omega/2\pi$ , which is a measure of the number of waves per unit of time. The acoustic velocity (particle velocity) can be determined then from the continuity equation and reads:

$$u_1 = \frac{1}{\rho_0 a_0} \left( \underbrace{A^+ e^{i(kx - 2\pi ft)}}_{\text{forward traveling wave}} - \underbrace{A^- e^{-i(-kx - 2\pi ft)}}_{\text{backward traveling wave}} \right) \quad (2.31)$$

The acoustic velocity  $u_1$  from Eq. 2.31 should not be confused with the sound speed which is denoted by  $a_0$ . The acoustic velocity indicates the speed at which the particles of the medium oscillate around their rest position. While the sound speed indicates the distance that a sound wave travels per unit time as it propagates through the medium. The correlation,  $\rho_0 a_0$ , in Eq. 2.31 defines the characteristic impedance of the medium and expresses the ratio of sound pressure to sound velocity for a travelling wave.

### *Standing Waves*

For linear acoustics, it can be assumed that the acoustic waves propagate at a constant speed equal to the speed of sound  $a_0$ . In case the damping of the wave can be neglected, the peak amplitudes of the oscillations along the propagation direction of the wave are at the same level. When two propagating acoustic waves with the same amplitude and frequency propagate in opposite directions to each other (e.g. as a result of reflections within a confined system), the interference of these waves results in a standing wave. At the resonant frequencies of a bounded system (e.g. a tube) the standing waves are called acoustic mode. The peak amplitude of the standing wave at any point in the physical space is constant over time. The locations where the modulus of the acoustic oscillations is minimal (e.g. zero) are called acoustic nodes, while the locations where the modulus is maximal are called acoustic anti-nodes. It is worth mentioning that an acoustic mode with an acoustic node with zero amplitude is only

generated if the forward and backward travelling waves have the same amplitude of oscillation. In case the amplitudes are not similar (e.g. as it is the case when the wave is not completely but partially reflected at the boundary of the confined system), the amplitudes at the acoustic nodes will deviate from zero. For a good overview of the basics of acoustic waves, readers are referred to chapters 5 and 6 of the textbook of T. Lieuwen [88].

#### 2.4.1 Acoustic Source Term

The level of acoustic fluctuation in a point of a domain might be measured by the acoustic energy density defined as [89]:

$$e_{ac} = \frac{1}{2}(\rho_0 \vec{U}_1^2 + \frac{p_1^2}{\rho_0 a_0^2}) \quad (2.32)$$

In a reacting flow, the heat release rate oscillation may correlate with the acoustic pressure oscillation and serve as a local source of acoustic energy  $S_{ac}$  [64], which is defined as follows:

$$S_{ac} = \frac{\gamma - 1}{\gamma p_0} (p_1 \dot{q}_1) \quad (2.33)$$

In the above equation,  $\gamma$  represents the specific heat capacity of the mixture. When the heat release rate oscillates in phase with pressure ( $|\Delta\theta_{p_1, q_1}| < 90^\circ$ ) at a point in physical space, the correlations act as the local source of acoustic energy and the oscillations are excited; when they are out of phase ( $|\Delta\theta_{p_1, q_1}| > 90^\circ$ ), the correlation acts as a local sink term. However, knowledge of added or extracted energy to/from the acoustic field at a given point is not sufficient to make a statement about the system's susceptibility to instability. The overall acoustic behavior of the system can be determined by a double integration of the source term over the volume of the system  $V_s$  and the time period of the oscillations  $t_p$ . If the result exceeds the acoustic losses of the system  $L_i$  (e.g. by viscous dissipation or propagation of the acoustic energy out of the boundaries of the system), the amplitude of the acoustic fluctuations increases and the system tends to become unstable [90]:

$$\int_{t_p} \int_V p_1 \dot{q}_1 dV dt > \int_{t_p} \int_V \Sigma L_i dV dt \quad (2.34)$$

Figure 2.3 illustrates a typical time evaluation of the local acoustic pressure in a thermoacoustically unstable combustion chamber, when combustion instability was triggered at  $t = 0$ . The overall development of the instability can be decomposed as follows: The linear zone, near  $t = 0$ , where the acoustic variables are very small compared to the mean variable of the flow. Furthermore, in this zone the response of the system (e.g. oscillation of the heat release rate) is linearly proportional to the acoustic per-

turbation. With time, energy is added to the acoustic field and the amplitude of the oscillations grows exponentially. However, the amplitudes do not grow indefinitely and reach a limit cycle. The transition into the limit cycle zone often reveals an overshoot. In the limit cycle zone the acoustic energy gain is equal to the acoustic losses of the system and the heat release response is saturated [91, 92]. In the this zone the response of the system may not follow a linear response [93].

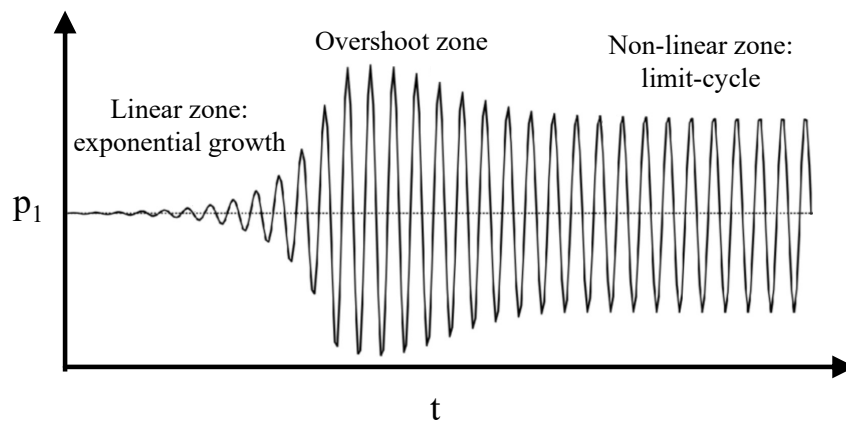


**Fig. 2.3** Pressure oscillations from linear regime to limit-cycle [64]

## CHAPTER 3

### Simulation and Modelling of Reactive Flows

#### 3.1 Direct Numerical Simulation

Direct Numerical Simulation (DNS) resolves turbulent structures of all sizes by directly solving the transport equations presented in the last chapter without further modelling, except for the chemical and thermodynamic state relations and properties. Therefore a very high temporal and spatial resolution is crucial to perform DNS. The required number of cells in each direction  $N_{cells_x}$  to resolve the smallest eddies can be estimated from the ratio of the integral length scale  $l_t$  to Kolmogorov length scale  $\eta$ , and reads [64]:

$$N_{cells_x} \approx \frac{l_t}{\eta} = Re^{(3/4)} \quad (3.1)$$

DNS of the turbulent flow must be performed under consideration of the three-dimensional properties of the configuration, since turbulence is a 3D phenomenon. Hence, the total required number of cells  $N_{cells}$  for a 3D DNS can be estimated from:

$$N_{cells} \approx \left(\frac{l_t}{\eta}\right)^3 = Re^{(9/4)} \quad (3.2)$$

The required temporal resolution is derived from the CFL criterion [94], which describes that the fluid entering a computational cell with a velocity  $u$  is not allowed to leave the cell during one time step:

$$\Delta t < \frac{l_{cell}}{u} \quad (3.3)$$

The high cost of DNS makes it less attractive and currently not applicable for technical configurations with complex geometries. Typical applications to DNS are fundamental investigations on simplified geometries [95].

#### 3.2 Large Eddy Simulation

The basic idea of Large-Eddy-Simulation (LES) is to directly solve the large turbulent eddies, which contain the majority of the turbulent kinetic energy, and to model the

effect of the smaller eddies, which contain a smaller amount of turbulent kinetic energy. In this way, an affordable, but reasonably accurate calculation approach is introduced. In order to distinguish between the large-scale and small-scale turbulent eddies, the spatial LES filter  $F_{LES}$  is introduced. The filter is applied to the governing equations over the computational domain  $V$  to remove the small-scale eddies [96]. The filtered quantity  $\bar{\Phi}$ , which contains the large-scale eddies of the field  $\Phi$ , can be expressed as:

$$\bar{\Phi}_{LES}(x_j, t) = \int_V \Phi(x_j - x'_j) F_{LES}(x'_j) dx'_j \quad (3.4)$$

The removed small-scale eddies are termed as sub-grid scale fluctuation of the field  $\Phi$ , and reads:

$$\Phi'_{LES}(x_j, t) = \Phi - \bar{\Phi}_{LES}(x_j, t) \quad (3.5)$$

In this thesis, the filtering is implicitly conducted by the numerical grid used in the LES. The size of the filter can be estimated from the cubic root of the cell volume  $V_{cell}$  as:

$$\Delta = (V_{cell})^{\frac{1}{3}} \quad (3.6)$$

In case of non-constant density problems, e.g. problems with combustion, terms that are not closed may occur in the following form:

$$\overline{\rho(x_j, t)\Phi(x_j, t)} = \int_V \rho(x_j - x'_j)\Phi(x_j - x'_j)F_{LES}(x'_j) dx'_j \quad (3.7)$$

These terms make the direct calculation of the filtered variable  $\bar{\Phi}$  and the filtered density  $\bar{\rho}$  difficult. A density-weighted Favre filtering can be employed to avoid the correlation term  $\overline{\rho\Phi}$ . The density-weighted Favre-averaged variable is defined as:

$$\tilde{\Phi}(x_j, t) = \frac{\overline{\rho(x_j, t)\Phi(x_j, t)}}{\bar{\rho}(x_j, t)} \quad (3.8)$$

### 3.2.1 Favre-Filtered Governing Equations

By applying Favre filtering to the conservation equations, the Favre-averaged equations of mass, momentum, total enthalpy and species are obtained, which can be expressed as follows:

$$\frac{\partial \bar{\rho}}{\partial t} + \frac{\partial(\bar{\rho}\tilde{u}_i)}{\partial x_i} = 0 \quad (3.9)$$

$$\frac{\partial(\bar{\rho}\tilde{u}_i)}{\partial t} + \frac{\partial(\bar{\rho}\tilde{u}_i\tilde{u}_j)}{\partial x_j} = -\frac{\partial \bar{p}}{\partial x_i} + \bar{\rho}g_i + \frac{\partial \bar{\tau}_{ij}}{\partial x_j} - \frac{\partial \bar{\rho}(\tilde{u}_i\tilde{u}_j - \tilde{u}_i\tilde{u}_j)}{\partial x_j} \quad (3.10)$$

$$\frac{\partial(\bar{\rho}\tilde{h})}{\partial t} + \frac{\partial(\bar{\rho}\tilde{u}_i\tilde{h})}{\partial x_i} + \frac{\partial(\bar{\rho}\tilde{K})}{\partial t} + \frac{\partial(\bar{\rho}\tilde{u}_i\tilde{K})}{\partial x_i} = -\frac{\partial \bar{p}}{\partial t} + \frac{\partial}{\partial x_j} \left( \alpha \frac{\partial \tilde{h}}{\partial x_j} \right) - \frac{\partial \bar{\rho}(\tilde{u}_j\tilde{h} - \tilde{u}_j\tilde{h})}{\partial x_j} \quad (3.11)$$

$$\frac{\partial(\bar{\rho}\tilde{Y}_K)}{\partial t} + \frac{\partial(\bar{\rho}\tilde{u}_j\tilde{Y}_K)}{\partial x_j} = \frac{\partial}{\partial x_j} \left( -\frac{\mu}{Sc_K} \frac{\partial\tilde{Y}_K}{\partial x_j} \right) + \bar{\omega}_K - \frac{\partial\bar{\rho}(\tilde{u}_j\tilde{Y}_k - \tilde{u}_j\tilde{Y}_k)}{\partial x_j} \quad (3.12)$$

In the energy equation, Eq. 3.11,  $K = \frac{1}{2}\tilde{u}_i\tilde{u}_i$  is the kinetic energy and  $\alpha$  is the thermal diffusivity. Equations 3.10 to 3.12 include additional unknown terms, which need to be modelled. These terms are a) sub-grid scale stresses  $(\tilde{u}_i\tilde{u}_j - \tilde{u}_i\tilde{u}_j)$ , b) the unresolved species fluxes  $(\tilde{u}_j\tilde{Y}_k - \tilde{u}_j\tilde{Y}_k)$  and c) the unresolved enthalpy fluxes  $(\tilde{u}_j\tilde{h} - \tilde{u}_j\tilde{h})$ . Additionally, a model for the filtered reaction source term  $\bar{\omega}_K$  is needed to account for the turbulent combustion. The unresolved species and enthalpy fluxes are modelled using the turbulent Schmidt number  $Sc_t$  and the turbulent Prandtl number  $Pr_t$  and a gradient assumption [64]:

$$(\tilde{u}_j\tilde{Y}_k - \tilde{u}_j\tilde{Y}_k) = -\frac{\nu_t}{Sc_t} \frac{\partial\tilde{Y}_K}{\partial x_j} \quad (3.13)$$

$$(\tilde{u}_j\tilde{h} - \tilde{u}_j\tilde{h}) = -\frac{\nu_t}{Pr_t} \frac{\partial\tilde{h}}{\partial x_j} \quad (3.14)$$

### 3.2.2 Sub-Grid Scale Turbulence Models

The sub-grid scale stresses  $(\tilde{u}_i\tilde{u}_j - \tilde{u}_i\tilde{u}_j)$  comprise the effect of turbulent fluctuations with a length scale below the cell size, which has to be modelled. Different approaches to model the unresolved stresses are known from the literature [64, 73], which describe the effect of sub-grid scale fluctuations using the resolved fluid quantities. This thesis uses the  $k$ -equation model [97]. The model is based on a transport equation for the turbulent kinetic energy and is briefly explained below.

#### *K-Equation Model*

A transport equation for the sub-grid scale kinetic energy was proposed by Yoshizawa et al. [97] and Menon et al. [98] to improve the accuracy of the LES sub-grid scale stress models. The balance equation for  $k_{sgs}$  is written as [99]:

$$\frac{\partial(\bar{\rho}k_{sgs})}{\partial t} + \frac{\partial(\bar{\rho}\tilde{u}_j k_{sgs})}{\partial x_j} - \frac{\partial}{\partial x_j} (\bar{\rho}(\nu + \nu_t) \frac{\partial k_{sgs}}{\partial x_j}) = -\rho\tau_{ij}\tilde{S}_{ij} - C_\epsilon \frac{\rho k_{sgs}^{3/2}}{\Delta} \quad (3.15)$$

The sub-grid scale stress tensor is approximated as:

$$\tau_{ij} = -2\nu_t(\tilde{S}_{ij} - \frac{\delta_{ij}}{3}\tilde{S}_{kk}) + \frac{2}{3}k_{sgs}\delta_{ij} \quad (3.16)$$

The sub-grid scale eddy viscosity is calculated using  $k_{sgs}$  and reads:

$$\nu_t = C_k\Delta\sqrt{k_{sgs}} \quad (3.17)$$

The LHS of Eq. 3.15 features the time derivative term, convective term, molecular and turbulent diffusion terms. The first term in the RHS of Eq. 3.15 deals with production of sub-grid turbulence and the last term with dissipation of sub-grid turbulence. The constants in the model are set to  $C_\epsilon = 1$  and  $C_k = 0.09$  as proposed by Yoshizawa et al. [97].

### 3.2.3 Turbulent Combustion Modeling

The thickness of a laminar premixed methane flame is around 0.4 mm for atmospheric pressure and a lean mixture of  $\phi = 0.7$  with a temperature of 700 K, which is a typical mixture temperature in gas turbines. For this mixture, the flame thickness decreases with pressure and is only 0.07 mm at 20 bar, the typical operating pressure of combustion chambers in heavy-duty gas turbines<sup>1</sup>. These thicknesses are much thinner than the affordable cell sizes typically used for the LES of technical configurations. This is why the chemistry and its interaction with turbulence must be modeled to calculate real technical flames. Three methods are commonly used for premixed combustion: a) the Flame Surface Density (FSD) approach [101, 102], b) the Artificial Thickened Flame (ATF) technique [103, 104] and c) the level-set (G-equation) method [105, 106]. In the scope of this work, the FSD approach is used and will be discussed further.

#### *Flame Surface Density*

The flame surface density model (FSD) is based on the flamelet approaches. In this model, the flame propagation can be described via a transport equation for the Favre filtered reaction-regress variable<sup>2</sup> ( $\tilde{b} = 1 - \tilde{c}$ ) [102], where  $c$  is the more commonly used progress variable [107]. The transport equation for the Favre-filtered regress variable [102] can be written as:

$$\frac{\partial(\overline{\rho b})}{\partial t} + \frac{\partial \overline{\rho b \tilde{u}_i}}{\partial x_i} - \frac{\partial}{\partial x_i} (\overline{\rho} D_t \frac{\partial \tilde{b}}{\partial x_i}) = -\overline{w}_c + \frac{\partial}{\partial x_i} \overline{(\rho D \frac{\partial b}{\partial x_i})} = -\rho_u S_l \Sigma_{gen} \quad (3.18)$$

Within the previous equation,  $D$  and  $D_t$  respectively represent the molecular and sub-grid diffusion coefficients. The source term and the molecular diffusion term together ( $-\overline{w}_c + \frac{\partial}{\partial x_i} \overline{(\rho D \frac{\partial b}{\partial x_i})}$ ) can be modelled as the product of the density of the fresh mixture  $\rho_u$ , the laminar flame speed  $S_l$  and the generalized flame surfaced density  $\Sigma_{gen}$ . In the context of premixed combustion, the laminar flame speed  $S_l$  used in Eq. 3.18 is assumed to represent the chemistry and is usually assumed to be a function of the mean pressure and temperature and the equivalence ratio and must be determined prior to the

<sup>1</sup>The data were gained using Cantera [100] to simulate one-dimensional, laminar, freely propagating premixed flames.

<sup>2</sup>The reaction-regress variable is a peculiarity of the CFD code used, therefore it is used in the following discussion.

LES. The generalized flame surface density can be approximated by a sub-grid scale flame wrinkling factor  $\Xi$  and the modulus of the gradient of the filtered regress variable as [108, 109]:

$$\Sigma_{gen} = \Xi |\nabla \bar{b}| \quad (3.19)$$

Thus, the modelling of the interaction of sub-grid turbulence and combustion can be reduced to a model for the flame wrinkling factor on the sub-grid scale. Algebraic expressions are available to model  $\Xi$  (see for example the models proposed by Colin et al. [104], Charlette et al. [110] or Fureby et al. [109]). In the scope of this work, an algebraic model is used to close the turbulence chemistry interaction [111, 112], which reads:

$$\Xi = 1 + \frac{C}{Le} \sqrt{\frac{u'_{sgs} \Delta}{a_l}} \quad (3.20)$$

In the above equation,  $Le$  is Lewis number and  $C$  is a model constant. The sub-grid scale velocity fluctuation  $u'_{sgs}$  is calculated from the sub-grid turbulence kinetic energy:

$$u'_{sgs} = \sqrt{\frac{2k}{3}} \quad (3.21)$$

In this thesis, the influence of acoustic pressure fluctuations on the flame speed can be considered by introducing an algebraic equation. Therefore, it is assumed that the pressure changes in the combustion chamber at the flame position are mainly due to the acoustic oscillation and have isentropic properties. The pressure can be divided into its average value and acoustic fluctuation, which are indicated by the index 0 or 1:

$$p = p_0 + p_1 \quad (3.22)$$

The corresponding temperature can be calculated from the isentropic relation:

$$T = T_0 \left(\frac{p}{p_0}\right)^{\frac{\gamma-1}{\gamma}} \quad (3.23)$$

The modified temperature and pressure can be used to calculate a modified laminar flame velocity, which is composed of the mean laminar flame speed at mean pressure and mean temperature and a change due to the change in acoustic pressure and the associated temperature:

$$S_l = S_{l0} + S_{l1} \quad (3.24)$$

The unstretched laminar flame speed can then be parametrized for the pressure and fitted in form of a linear algebraic equation:

$$\frac{S_l}{S_{l0}} = \alpha \frac{p}{p_0} + \beta \quad (3.25)$$

In the above equation,  $\alpha$  and  $\beta$  are functions of the mean equivalence ratio, pressure and temperature, which were obtained by simulating one-dimensional, laminar freely propagating premixed flames using Cantera [113].

## CHAPTER 4

### Numerical Methods

#### 4.1 Finite Volume Method

The Finite Volume Method (FVM) can be used to discretize the integral form of the governing equations for a finite number of volumes within the solution domain. General transport equations for a scalar  $\Phi$  can be formulated as follows:

$$\underbrace{\frac{\partial(\rho\Phi)}{\partial t}}_{\text{accumulation}} + \underbrace{\frac{\partial(\rho\Phi u_j)}{\partial x_j}}_{\text{convection}} = \underbrace{\frac{\partial}{\partial x_j} \left( \Gamma_\Phi \frac{\partial\Phi}{\partial x_j} \right)}_{\text{diffusion}} + \underbrace{S_\Phi}_{\text{source}} \quad (4.1)$$

In this equation, the first term on the LHS refers to the temporal changes of the transport quantity  $\Phi$ . The second term on the LHS describes the convection of  $\Phi$  by the velocity field  $u_j$ . The first term on the RHS defines the diffusion of  $\Phi$  with the general diffusion constant  $\Gamma_\Phi$  and the last term on the RHS represents the rate of formation of  $\Phi$ . Integration of Eq. 4.1 on a finite volume  $\Delta V$ , into which the calculation area is divided (e.g. the calculation cells) and using the Gaussian theorem [114] to convert the volume integrals into surface integrals, Eq. 4.1 can be rewritten as:

$$\int_{\Delta V} \frac{\partial(\rho\Phi)}{\partial t} dV + \int_{\Delta A} (\rho\Phi u_j) n_j dA = \int_{\Delta A} \left( \Gamma_\Phi \frac{\partial\Phi}{\partial x_j} \right) n_j dA + \int_{\Delta V} S_\Phi dV \quad (4.2)$$

In the above equation,  $dA$  is the surface element and  $n_j$  is the outward unit vector normal to the surface. An approximation of the volume and surface integrals is required to obtain an algebraic equation for each control volume (cell volume). The surface integral of convection and diffusion terms in equation 4.2 can be approximated as the sum of the flux through the surfaces (denoted by index  $f$ ) of the cell volumes as follows:

$$\int_{\Delta A} (\rho\Phi u_j) n_j dA \approx \sum_f \rho_f \Phi_f u_f n_f \Delta A_f \quad (4.3)$$

$$\int_{\Delta A} \left( \Gamma_\Phi \frac{\partial\Phi}{\partial x_j} \right) n_j dA \approx \sum_f \left[ \Gamma_\Phi \frac{\partial\Phi}{\partial x_j} \right]_f n_f \Delta A_f \quad (4.4)$$

The volume integral of the source term may be approximated by evaluating its value in the cell center (denoted by index  $p$ ):

$$\int_{\Delta V} S_{\Phi} dV \approx [S_{\Phi}]_p \Delta V \quad (4.5)$$

## 4.2 Numerical Discretization Schemes

### 4.2.1 Spatial Discretization

Various discretization methods (e.g. upwind difference schemes, central difference scheme, total variation diminishing scheme) can be used to achieve algebraic equations in the FVM approach. The upwind differencing scheme (UDS) [115] assigns the cell face value to center value of the upwind cell with respect to the flow direction  $F_x$ . For the one-dimensional cell arrangement as shown in Fig. 4.1, the face value  $\Phi_f$  in UDS can be determined as [116]:

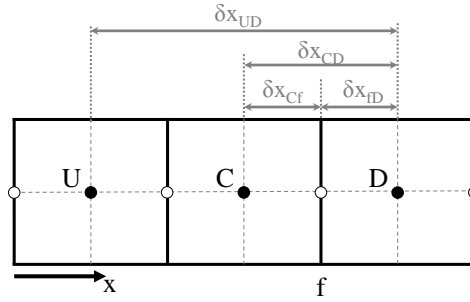


**Fig. 4.1** Sketch of a one-dimensional grid system.

$$\Phi_f = \begin{cases} \Phi_C & \text{for } F_x \geq 0 \\ \Phi_D & \text{for } F_x < 0 \end{cases} \quad (4.6)$$

The use of UDS for momentum fluxes and scalars improves the convergence behaviour of numerical analysis and ensures the boundedness of the solution by implicitly introducing numerical diffusion terms, however, at the cost of the accuracy of the solution [115]. More accurate, but also (more) susceptible to numerical oscillation is the Central Differencing Scheme (CDS). The central differencing scheme relates the cell face value  $\Phi_f$  with the values of the center of the neighboring cells and reads [116]:

$$\Phi_f = \left( \frac{\delta x_{fD}}{\delta x_{CD}} \right) \Phi_C + \left( 1 - \frac{\delta x_{fD}}{\delta x_{CD}} \right) \Phi_D \quad (4.7)$$

To ensure the boundedness of the solution in regions with strong gradients, while maintaining the accuracy of the results within the remaining computation domain, the

total variation diminishing (TVD) scheme [117, 118] can be used, which is a "limited" combination of a low-order differencing scheme (LO) and a high-order (HO) addition and reads [116]:

$$\Phi_f = (\Phi_f)_{LO} + \Psi(r)[(\Phi_f)_{HO} - (\Phi_f)_{LO}] \quad (4.8)$$

In the above equation,  $\Psi(r)$  represents the flux limiter function and  $r$  is the ratio of the upwind-side gradient to the downwind-side gradient (see Fig. 4.1 for notation):

$$r = \frac{\Phi_C - \Phi_U}{\Phi_D - \Phi_C} \quad (4.9)$$

For the equidistant 1D cell system (see Fig. 4.1), that uses a central differencing scheme as the higher order scheme and an upwind differencing scheme as the lower order scheme, Eq. 4.8 can be rephrased for the face value  $\Phi_f$  as:

$$\Phi_f = \Phi_C + \frac{1}{2}\Psi(r)[\Phi_D - \Phi_C] \quad (4.10)$$

The accuracy of the scheme and its boundedness behaviour are given by choice of the flux limiter function,  $\Psi(r)$ . An overview of common flux limiter functions can be found in the textbook of Versteeg and Malalasekera [119]. The range in which the flow limitation function must be within, as a TVD scheme, was introduced by Sweby [117] and highlighted in Fig 4.2.

In this thesis, the standard OpenFOAM *LimitedLinear* and *FilteredLinear* schemes were applied for the discretization of the momentum equation in the combustion chamber, which are briefly described in the following.

The *LimitedLinear* scheme is blended between the CDS and TVD schemes by applying a constant  $k_c$ , which is introduced in the limiter function of this scheme:

$$\Psi = \max \left( \min \left( \frac{2}{k_c} r_{OF}, 1 \right), 0 \right) \quad (4.11)$$

The scheme uses the cell gradient  $(\nabla\Phi)_C$  and the face gradient  $(\nabla\Phi)_f$  to calculate  $r_{OF}$  as following [120]:

$$r_{OF} := \frac{2(\nabla\Phi)_C \cdot \vec{d}}{(\nabla\Phi)_f \cdot \vec{d}} - 1 \quad (4.12)$$

In Eq. 4.12,  $\vec{d}$  is the vector between the current cell  $C$  and its neighbour. For the 1D cell system presented in Fig. 4.1, it can be shown that  $r_{OF}$  is equal to the ratio of the upwind-side gradient to downwind-side gradient (see Eq. 4.9):

$$r_{OF} = \frac{2 \frac{(\phi_D - \phi_U)}{\delta_{UD}} \delta_{CD}}{\frac{(\phi_D - \phi_C)}{\delta_{CD}} \delta_{CD}} - 1 = \frac{\Phi_C - \Phi_U}{\Phi_D - \Phi_C} = r \quad (4.13)$$

The *LimitedLinear* scheme is plotted in the  $\Psi - r$  digaramm in Fig. 4.2 for  $c_k$  equal to 0

and 1. The *LimitedLinear* scheme is converted to a TVD scheme for the value of  $k_c = 1$  and to a CDS scheme for the value of  $k_c = 0$ , when  $r > 0$ . For values of  $r$  below zero, regardless of the value of  $k_c$ , the scheme degenerates to UDS like other conventional TVD schemes [121]. In this thesis, a value of  $k_c = 0.1$  is used.

The *FilteredLinear* scheme violates Sweby's TVD criterion [117] to apply upwinding where it is needed. It is shown for similar schemes (e.g. Albada family limiters [122]) that this violation does not cause problems in practice for momentum transport. The schemes compare the face gradient with both neighbouring cell gradients and introduce between 0-20% upwinding to dampen numerical oscillations. For this scheme,  $r_{OF}$  is defined as:

$$r_{OF} = 2 - 0.5 \frac{\min \left( |(\nabla\phi)_f \cdot \vec{d} - (\nabla\phi)_C \cdot \vec{d}|, |(\nabla\phi)_f \cdot \vec{d} - (\nabla\phi)_N \cdot \vec{d}| \right)}{\max \left( |(\nabla\phi)_C \cdot \vec{d}|, |(\nabla\phi)_N \cdot \vec{d}| \right)} \quad (4.14)$$

The limiter is constrained between 0.8 and 1 and reads:

$$\Psi = \max \left( \min (r_{OF}, 1), 0.8 \right) \quad (4.15)$$

To be able to represent the limiter in the diagram  $\Psi - r$ , the 1D cell system is presumed. It is assumed that  $(\nabla\phi)_C > (\nabla\phi)_N$  and  $(\nabla\phi)_f > 0$ . Equation 4.14 can be reformulated to obtain:

$$r_{OF} = 2 - 0.5 \left( \left| \frac{2}{r+1} - 1 \right| \right) \quad (4.16)$$

As shown in Fig. 4.2, it turns out that the scheme for positive  $r$ -values is converted into CDS. The accuracy is reduced, with negative  $r$ -values, but the scheme is not converted to UDS and has a higher accuracy.

#### 4.2.2 Temporal Discretization

The general transport equation can be rearranged such that everything except the accumulation term is on the RHS of the equation:

$$\frac{\partial\Phi}{\partial t} = \text{RHS}(\phi) \quad (4.17)$$

The time derivatives might be then solved implicitly using the second-order Crank-Nicolson scheme [123], as used in this work. This scheme takes values from the current time step  $\Phi^n$  and the previous time step  $\Phi^{n+1}$  and reads:

$$\Phi^{n+1} = \Phi^n + \frac{1}{2} [\text{RHS}(\Phi^{n+1}) + \text{RHS}(\Phi^n)] \Delta t \quad (4.18)$$

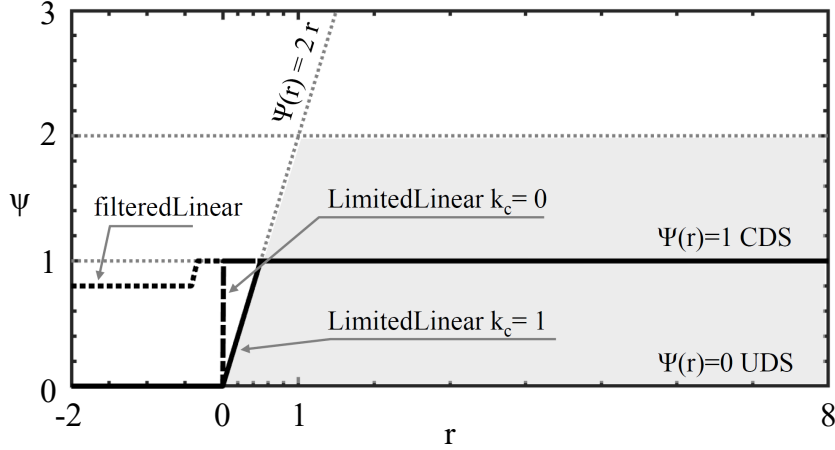


**Fig. 4.2** The limiter function for different discretisation schemes, TVD region based on sweby' criterion is highlighted [117]

The pure second order Crank-Nicolson scheme is often unstable for complex flows in complex geometries. To stabilize the scheme while maintaining a better accuracy than a first-order scheme, an off-centering  $0 \leq C_n \leq 1$  coefficient is introduced:

$$\Phi^{n+1} = \Phi^n + \frac{1}{(C_n + 1)} [\text{RHS}(\Phi^{n+1}) + C_n \text{RHS}(\Phi^n)] \Delta t \quad (4.19)$$

With a coefficient of  $C_n = 1$ , the scheme is fully centred and second-order, with a coefficient of  $C_n = 0$  the scheme is equivalent to Euler-implicit scheme. In this work a coefficient of 0.9 is used.

### 4.3 Boundary Conditions

#### 4.3.1 Non-Reflective Boundary Conditions

Applying the well-known Dirichlet and Neumann conditions at the domain boundaries leads to a complete reflection of the incident acoustic wave at these boundaries. The complete reflection of the wave at the boundary has the effect, that there is no acoustic energy flux through the boundaries of the system, which is unrealistic. The treatment of the boundaries may have a direct impact on the results of a thermoacoustic investigation. Positioning a fully reflective boundary condition in the wrong place can even completely change the resonance of the system. The impact of the boundary conditions on the solution, however, may be reduced by positioning the boundary condition far away from the interesting area [124] and using a sponge zone [125] to attenuate the acoustic waves and avoid numerical reflection. A better way to avoid reflections is to apply non-reflective boundary conditions. The non-reflecting boundary conditions used in this work are based on the NSCBC and the LODI approach [126, 127], which are not

available in standard OpenFoam.

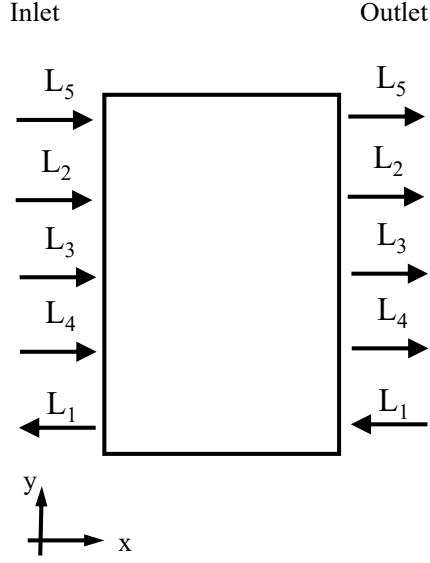


**Fig. 4.3** Boundary conditions located on the x-axis.

The NSCBC method is based on the principle that the solution is advanced in time by solving the fluid dynamic conservation equations at the boundary. The Navier-Stokes equations can be separated into a derivative normal to the boundary and the remaining terms. The derivative normal to the boundary can be related to the amplitude variation of characteristic waves  $L_i$  (defined in Eqs. 4.20 to 4.24) crossing the boundaries [128] as shown in Fig. 4.3.

$$L_1 = (u - c) \left( \frac{\partial p}{\partial x} - \rho c \frac{\partial u}{\partial x} \right) \quad (4.20)$$

$$L_2 = u \left( c^2 \frac{\partial \rho}{\partial x} - \rho c \frac{\partial p}{\partial x} \right) \quad (4.21)$$

$$L_3 = u \left( c^2 \frac{\partial v}{\partial x} \right) \quad (4.22)$$

$$L_4 = u \left( \frac{\partial w}{\partial x} \right) \quad (4.23)$$

$$L_5 = (u + c) \left( \frac{\partial p}{\partial x} + \rho c \frac{\partial u}{\partial x} \right) \quad (4.24)$$

To be able to advance the solution on the boundary in time, the amplitudes  $L_i$  of different waves crossing the boundary must be determined. To specify an approximation of values of  $L_i$ , a Local One-Dimensional Inviscid (LODI) system of equations can be used. The LODI system is obtained from the Navier-Stokes equations neglecting its

transverse, viscous and reaction terms. The LODI system can be written as:

$$\frac{\partial p}{\partial t} + \frac{1}{2}(L_5 + L_1) = 0 \quad (4.25)$$

$$\frac{\partial u}{\partial t} + \frac{1}{2\rho c}(L_5 - L_1) = 0 \quad (4.26)$$

$$\frac{\partial v}{\partial t} + L_3 = 0 \quad (4.27)$$

$$\frac{\partial w}{\partial t} + L_4 = 0 \quad (4.28)$$

$$\frac{\partial T}{\partial t} + \frac{T}{\gamma p} \left( \frac{1}{2}(\gamma - 1)(L_5 + L_1) - L_2 \right) = 0 \quad (4.29)$$

For a planar 1D wave,  $L_3$  and  $L_4$  can be assumed to be zero from Eq. 4.27 and 4.28. If the remaining  $L_i$  are known, they can be replaced in the Navier-Stokes equations and the boundary values are calculated by advancing these equations. However, the LODI relation itself can be used to approximate the boundary values [129]. The latter method is used in this work.

#### *Inflow Boundary Condition Without Excitation*

A perfectly non-reflecting inflow boundary condition leads to a drift of the desired mean inlet velocity  $u^d$  and temperature  $T^d$ . In order to maintain the target values and at the same time achieve a partially anechoic boundary condition, a relaxation parameter  $\sigma$  can be introduced and the amplitude variation of characteristic waves can be written as:

$$L_2 = \sigma_2(T - T^d) , \quad L_5 = \sigma_5(u - u^d) \quad (4.30)$$

For  $\sigma \rightarrow 0$ , the boundary condition tends to behave perfectly non-reflecting, while not maintaining target values. For a large value of  $\sigma$ , the boundaries tend to act fully reflecting. For intermediate values of  $\sigma$ , as chosen for this study, a partially non-reflective boundary condition can be achieved while preserving the target values.

The characteristic waves  $L_2$  and  $L_5$  are defined through Eq. 4.30. These can be inserted into the equations 4.25 and 4.26 and 4.29 in the LODI system to obtain the final equations for pressure (Eq. 4.31), velocity (Eq. 4.32) and temperature (Eq. 4.33). The equations must be solved at the inlet boundary to determine the time-dependent velocity, pressure and temperature.

$$\frac{\partial p}{\partial t} + \frac{1}{2}(u - c) \left( \frac{\partial p}{\partial x} - \rho c \frac{\partial u}{\partial x} \right) + \sigma_5(u - u^d) = 0 \quad (4.31)$$

$$\frac{\partial u}{\partial t} + \frac{1}{2\rho c}(u - c) \left( \frac{\partial p}{\partial x} - \rho c \frac{\partial u}{\partial x} \right) + \frac{\sigma_5}{\rho c}(u - u^d) = 0 \quad (4.32)$$

$$\frac{\partial T}{\partial t} + \frac{T}{\gamma p} \left( \frac{1}{2} (\gamma - 1) (\sigma_5 (u - u^d) + (u - c) \left( \frac{\partial p}{\partial x} - \rho c \frac{\partial u}{\partial x} \right)) - \sigma_2 (T - T^d) \right) = 0 \quad (4.33)$$

### *Inflow Boundary Condition With Prescribed Fluctuations*

To have a partially non-reflecting boundary condition allowing to impose turbulent fluctuations or sinus waves at desired frequencies, the amplitude of the in-going characteristic wave  $L_5$  can be modified for the desired velocity  $u^d = \bar{u}^d + u'^d$  as proposed by Guezennec et al. [130]:

$$L_5 = \sigma_5 (u - \bar{u}^d) - 2\rho c \frac{\partial u'^d}{\partial t} \quad (4.34)$$

In Eq. 4.34,  $u'^d$  denotes the instantaneous fluctuation to be imposed at the boundary. In order to perform forced response simulations within the scope of this thesis, a harmonic velocity oscillation with a frequency of  $f$  and an amplitude of  $A$  and a phase of  $\phi$  is imposed in the following form:

$$u'^d = A \sin(2\pi ft + \phi) \quad (4.35)$$

For perfectly non-reflective inlet boundary conditions ( $L_1, \sigma_5 = 0$ ), the pressure oscillation at the boundary can be determined from Eq. 4.25 and yields:

$$p'^d = \rho c (A \sin(2\pi ft + \phi)) = \rho c u'^d \quad (4.36)$$

### *Outflow Boundary Condition*

At the outlet, the characteristic wave  $L_1$  enters the domain. Setting this value to zero results in a perfectly non-reflecting outlet. However, information about the desired operating pressure  $p^d$  cannot be provided to the system. The partially non-reflective outlet formulation is derived similar to the partially non-reflective inlet boundary condition, using a relaxation parameter whose value affects the reflection at the boundary.

$$L_1 = \frac{\sigma(1 - M^2)c}{D_d} (p - p^d) \quad (4.37)$$

In the above equation,  $M$  is the Mach number, and  $D_d$  the characteristic size of the domain. Substituting  $L_1$  from Eq. 4.37,  $L_2$  and  $L_5$  from Eqs. 4.21 and 4.24 into Eqs. 4.25, 4.26 and 4.29, the final equations to be solved at the exit boundary can be reached to determine the time-dependent velocity, pressure and temperature.

### 4.3.2 Turbulent Boundary Condition

Within the forced response study framework, a turbulence generator which is inspired by Klein et al. [124], is used to generate artificial velocity fluctuations. The resulting velocity fluctuation normal to the inlet boundary is then fed into Eq. 4.34 to obtain a partially non-reflecting turbulence boundary condition. A brief explanation of Klein's method for generating artificial turbulence is given here. For further information on other turbulence generation methods, readers are referred to the review paper by Tabor et al. [131].

The turbulence generator proposed by Klein is based on filtering a field of random numbers to generate velocity time series at each point in the inlet. This filtered random signal features the required spatial length scales and can be further transformed to conform to a prescribed Reynolds stress tensor. In the OpenFOAM implementation to obtain homogenous turbulence, first, three fields of Gaussian random numbers  $r^n$  with zero mean and unity standard deviation with a size of  $(2N_t, 2N_y + M_y + 1, 2N_z + M_z + 1)$  is created, where  $N_t$ ,  $N_y$  and  $N_z$  are the support of the filter function and  $M_y$  and  $M_z$  indicates the grid dimensions at the inflow plane.  $N_t$ ,  $N_y$  and  $N_z$  are selected so that they are twice as large as the time scale  $L_t$  and the length scales  $L_y$  and  $L_z$ , respectively. The time scale and length scale must be known (e.g. from Experiment). The random number field  $r^n$  is convoluted with a filter  $B(i, j, k)$  to obtain a two-dimensional array of spatially correlated data  $R(J, K)$  for  $J = 1, \dots, M_y$  and  $K = 1, \dots, M_k$ :

$$R(J, K) = \sum_{i=-N_t}^{N_t} \sum_{j=-N_y}^{N_y} \sum_{k=-N_z}^{N_z} B(i, j, k) r^n(i, J + j, K + k) \quad (4.38)$$

The three-dimensional filter  $B(i, j, k)$  can be expressed as the product of three one-dimensional filters:

$$B(i, j, k) = b_i \cdot b_j \cdot b_k \quad (4.39)$$

In Eq. 4.39, the one-dimensional filter can be defined using the corresponding time or length scale:

$$b_k = \tilde{b}_k / \left( \sum_{s=-N}^N \tilde{b}_s^2 \right)^{0.5} \quad \text{and} \quad \tilde{b}_k := \exp\left(\frac{0.5\pi \Delta_k k^2}{L_k}\right) \quad (4.40)$$

Thus, inlet data with zero mean, unity standard deviation, and a prescribed integral length scale, is generated. The homogeneous pseudo-turbulence in each time step is then generated by the superimposing the filtered data to the mean velocity.



## CHAPTER 5

### **Large-Eddy Simulation of Acoustic Flame Response to High-Frequency Transverse Excitations**

*This chapter including all figures and tables was previously published in AIAA Journal, 57(1), V. Sharifi, C. Beck and A. M. Kempf, Large-Eddy Simulation of Acoustic Flame Response to High-Frequency Transverse Excitations [35]. The author V. Sharifi ran all simulations, wrote the paper and generated all figures and tables. The authors C. Beck and A. M. Kempf contributed corrections, discussions and proofreading.*

The objective of this numerical study is to analyze the excitation mechanisms of high-frequency thermoacoustic instabilities. Two distinct acoustic wave/flame interaction scenarios are considered, which can arise in a technical combustion system. First, an acoustic oscillation is enforced with the pressure anti-node at the burner centerline, termed as pressure forcing. Second, a transverse acoustic oscillation is enforced with the velocity anti-node at the burner centerline, termed as velocity forcing. The excitations are created by the interaction of two incident acoustic waves for a range of excitation frequencies of practical relevance. The susceptibility of the flame to acoustic oscillations is quantified using the Rayleigh index. Detailed postprocessing is performed to investigate the underlying thermoacoustic mechanisms and to quantify the contributions of each possible mechanism to the total Rayleigh index of the system as a function of different excitation frequencies. It is observed that the main driving mechanism with pressure forcing can be related to the density oscillation and that the main driving mechanism with velocity forcing can be related to the flame surface oscillation relative to the position of the acoustic pressure node. For both forcing cases, the laminar flame speed is varied to change the length of the flame. With pressure forcing, the highest Rayleigh index is found for a specific flame length, associated to a specific laminar flame speed. With velocity forcing, the Rayleigh index increases when the flame speed is reduced and the flame length is increased, respectively.

## 5.1 Introduction

Thermo-acoustic instabilities have been observed in low NO<sub>x</sub> combustors for gas turbines [132, 133] and occur due to the coupling between heat release oscillations and pressure oscillations [13]. The instabilities typically occur at a frequency close to the frequency of the acoustic resonant modes of the combustion chamber [8]. Based on the acoustic mode shape, the frequency range and different strategies for tackling these instabilities, they can be classified into three categories that are relevant for can-type combustors in large gas-turbines: Low Frequency Dynamics (LFD,  $f < 50$  Hz), Intermediate Frequency Dynamics (IFD,  $50 < f < 1000$  Hz) and High Frequency Dynamics (HFD,  $f > 1000$  Hz) [134]. The LFD modes are often Helmholtz modes and do not match any of the longitudinal acoustic modes of the combustion system. The mode shape of IFD normally matches one of the longitudinal eigenmodes of the combustion chamber. The HFD modes, however, have radial and or circumferential components in addition to the longitudinal component. HFDs are less investigated by experiments and simulations mainly for two reasons.

- 1) Experiments with reproducible HFD are hard to set up.
- 2) Simulations of large-scale combustor geometries are normally too expensive for running parameter studies.

There are two major methods to study thermo-acoustic instabilities: self-excited [135, 136] and forced response [137, 55, 138, 139, 140] approaches. While in the self-excited method, the complete combustor must be investigated, in the forced response approach a reduced combustor geometry can be used. The main advantages of the self-excited approach are that all of the excitation- and feedback mechanisms are present and that the flame interacts with the three-dimensional acoustic mode of the combustor. In the forced response method, the acoustic mode is generated through the perturbations prescribed on the boundaries. The main advantages of the forced response approach are the ability to study the dynamics of an individual flame under varied acoustic frequencies, amplitudes and acoustic mode shapes. However, in this method the three-dimensional thermo-acoustic behavior of the real combustor is neglected.

The response of an acoustically compact swirl flame to low-frequency transverse pressure node and anti-node was experimentally investigated by Smith et al. [141], for a frequency range of 20 to 250 Hz. They found that a flame at a pressure node does not contribute to the spatially integrated heat release rate. For a flame at a pressure anti-node, they postulated that the induced axial acoustic fluctuation at the burner outlet plays a more important role than the transverse acoustic oscillation in the chamber for the low-frequencies. Saurabh et al. [142] investigated a similar flame, and

showed that the response of the flame to a pure axial acoustic modulation reduces towards higher forcing frequencies. Thus, the conclusion of Smith et al. [141] might be no more valid in high-frequency regimes. Lespinasse et al. [48] studied the flame dynamics of a laminar V-shaped flame at different locations of a transverse standing wave at 506 Hz and 1012 Hz. They found a symmetrical flame surface modulation when the flame was at a pressure anti-node, and an asymmetric modulation, when it was in other locations. They observed the most visible asymmetry for the flame positioned in a simultaneous pressure and velocity oscillation (positioned between pressure anti-node and velocity anti-node). However, they did not identify the contribution of the observed flame modulation on the instabilities of the system. For the same experiment Baillet et al. [143] showed that the flame at a pressure anti-node can show strong oscillations in sub-harmonic frequencies depending on the excitation amplitude. In the present study this non-linear behavior of the flame is not considered. Rogers et al. [20] took measurements in a rectangular atmospheric combustor, with a bluff-body stabilized premixed flame. They observed a transverse high-frequency oscillation of 3800 Hz and found alternate vortex shedding from the lips of the flame holder with the same frequency of the instability. They suggested the following mechanism: the transverse velocity forms a vortex, which consists of a fresh mixture, and helps to transport the generated vortex into the hot recirculation zone. The amplitude of oscillations increases, if the time it takes for these pockets of fresh mixture to mix with the hot gas, ignite and burn lies in a suitable range relative to the acoustic oscillations. Schwing et al. [21] studied the excitation mechanism in a tubular single burner combustor with a premixed swirl flame. They observed the first transverse acoustic mode with a frequency of 3300 Hz and periodic vortex shedding with an opposed phase in the upper and lower half of the combustor. They proposed the following mechanism: the acoustic transverse velocity forms pockets of combustion products in the unburnt mixture, these pockets will be transported with the mean flow and cause oscillations in the heat release rate further downstream. The periodic movement of the flame brush observed for the swirled flame in this rig motivated Schwing et al. [44, 45] to propose a new mechanism, termed as flame-displacement mechanism. Based on this mechanism, the acoustic transverse velocity shifts the flame to the region with higher pressure, so that the flame always releases heat at high acoustic pressures, and thus the Rayleigh Index is always positive. Additional to the flame-displacement mechanism, Hummel et al. [46] proposed a flame-deformation mechanism for the high-frequency instabilities: The flame is deformed due to the local gradient of the acoustic displacement, so that the local heat release rate is increased in the compressed reaction zone and decreased in the expanded reaction zone. They also proposed a model for non-compact heat release rate oscillations due to the flame-displacement and flame-deformation mechanisms. Berger et al. [47] validated this model by comparing the superposition of the contribution of both mechanisms with

the heat release rate oscillation measured in the experiment. This model is used in a numerical investigation by Hummel et al. [46], implying a more significant contribution from flame-deformation mechanism compared to the flame-displacement mechanism. However, their study is restricted to the observed frequency of the instabilities in their rig, and the effect of the frequency on the importance of the studied mechanisms was not addressed.

Méry et al. [144] analyzed how flame instability is affected by (a) the flame motion due to the transverse oscillation and (b) the flame structure modulation due to the axial oscillation. They found that the flame motion becomes more important for the system with smaller transverse length and higher resonance frequency. They [49] also investigated the dynamics of a cryogenic flame in a scaled rectangular multi-injectors combustor experiment. The combustor was modulated to excite the first transverse eigenfrequency with a pressure node in the vicinity of the central burner. They observed a synchronized up and down displacement of the flames and an out-of-phase oscillation of heat release rate in the upper and lower part of the chamber. Due to the in-phase oscillation of the unsteady heat release rate with the pressure on each sides of the combustor, they conclude that the flame-displacement mechanism or direct pressure effect on the flame might be the main reasons of the heat release rate oscillation. Hakim et al. [55] simulated the same setup and observed that the flame furthest from the center plane produces unsteady heat release rate with a larger amplitude than the central flame, indicating that the direct effect of pressure fluctuations on the heat release rate is more important in this case. They [33] also studied the dynamics of a non-premixed jet flame in a rectangular combustor for a flame positioned in pressure anti-node for 2 and 8 kHz. By calculating the Rayleigh Index for both modulation frequencies, they noted a decrease in the contribution of the flame to the growth of instabilities for the higher frequency case. Zellhuber et al. [34] proposed a theoretical model for the decomposition of the thermo-acoustic source term and used this model in a forced response simulation of a generic reheat combustor. They observed that the density fluctuation and the flame-displacement had a significant contribution to the instabilities. In their further investigation [139], they observed a significant increase in the response of the flame to the acoustic excitation, considering the pressure sensitivity of reaction kinetics in the forced response configuration.

The wavelength of high-frequency acoustic modes can be expected to be of the order or less than the circumferential/ transverse dimension of the chamber. This may lead to a situation where different flames in a can-type combustion chamber with multiple burners experience different acoustic fields in the high-frequency regime, as illustrated in Fig. 5.1. The figure shows the first three azimuthal acoustic modes in cross sections of the combustor. Each mode shape will lead to different acoustic fields for the burners. The present study is motivated by the fact that previous studies on high-frequency trans-

verse forcing were mainly focused on the mechanism of the flame in a pressure node and have not addressed the flame in velocity node nor the effect of forcing frequency on the different mechanisms for acoustic instabilities. To understand how the response of Bunsen-type flames varies under different acoustic conditions of a high-frequency azimuthal mode, a simplified single burner combustor, as illustrated in Fig. 5.2, is used. The simplified combustor consists of a duct and a sudden expansion into a rectangular combustion chamber. To focus on the flame response and to avoid complexities (introduced by upstream or downstream, e.g. plenum, compressor, turbine), non-reflecting boundary conditions are used. The flame is subjected to transverse acoustic modulation from the top and bottom of the combustor, representing the azimuthal acoustic field for the flame in the can-type combustor. Two extreme situations are studied. In the first configuration (pressure forcing), the acoustic pressure anti-node and acoustic velocity node are positioned at the center-line of the flame, corresponding to burners A or C for the 1T mode (see Fig. 5.1). In the second configuration (velocity forcing), the center-line of the flame is subjected to an acoustic velocity anti-node and acoustic pressure node, corresponding to burners B or D for the 1T mode (see Fig. 5.1).

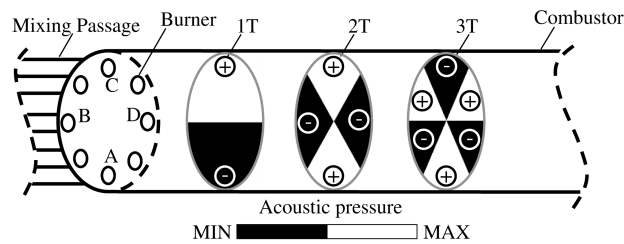


**Fig. 5.1** The first three azimuthal acoustic pressure modes of a can-type combustor.

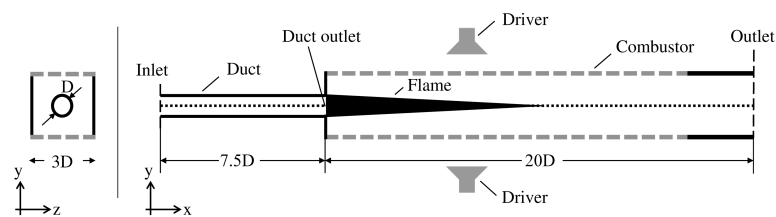


**Fig. 5.2** The simplified combustion chamber. Forcing boundaries are highlighted with dashed lines;  $D = 40$  mm.

## 5.2 Test Cases

The geometry of the simplified combustion chamber is shown in Fig. 5.2. The geometry consists of a cylindrical (premixing) duct and a rectangular chamber. A preheated mixture of air and methane with an equivalence ratio of 0.7 and a temperature of 500 K is fed through the inlet at a pressure of 800 kPa .

Non-reflecting boundary conditions are imposed at the inlet and outlet of the chamber, such that most of the acoustic energy leaves the domain, enabling investigation of the system without influence from upstream and downstream features and avoiding undesired effects of uncontrolled waves on the flame. No self-excited thermo-acoustic instability is observed, indicating that the case is free of intrinsic thermo-acoustic instabilities [95]. The non-reflecting boundary conditions are based on the NSBC and LODI approach [126, 127], which are not available in standard OpenFoam [145], details about their implementation and application for calculating the flame transfer function are given in [146, 63, 147]. In the implementation, the LODI relations are relaxed by a time scale  $\tau$ , which is set as a function of the excitation frequency  $f$ ,  $\tau = 10/f$ , leading to a reflection coefficient of approximately 0.025 at the boundaries.

The turbulence generator by Klein et al. [124] is coupled with the non-reflective boundary condition at the inlet based on "subsonic non-reflecting inflow with vorticity injection" formulation [64] to add artificial velocity fluctuations to the mean velocity profile. The turbulence intensity is set to 10 %, and the length scale is set to 30 % of the duct diameter to mimic the fluid dynamical effect of the fuel injectors in a technical combustion chambers. The operating conditions of the flame in this study are summarized in table 5.1. The implementation of the non-reflecting boundary condition allows

**Table 5.1** Overview of the operating conditions

| <i>fuel</i> | $\dot{m}$ , kg s <sup>-1</sup> | $p$ , kPa | $T_{in}$ , K | $\phi$ , - | $P$ , MW |
|-------------|--------------------------------|-----------|--------------|------------|----------|
| $CH_4$      | 0.69                           | 800       | 500          | 0.7        | 1.4      |

imposing an ingoing characteristic wave without interaction with outgoing waves. To generate a standing wave and represent the acoustic field in a can-type combustor, the methodology introduced by Ducruix et al. [148] is used in the present study. Acoustic forcing is imposed by the modulation of the transverse velocity on the upper and lower boundaries of the rectangular chamber. At these boundaries, ingoing transverse traveling waves are imposed according to eqs. (5.1, 5.2):

$$v_{bot} = \hat{v}_{bot} \cos(2\pi ft) \quad (5.1)$$

$$v_{top} = \hat{v}_{top} \cos(2\pi ft + \Theta) \quad (5.2)$$

Harmonic waves with the desired amplitudes  $\hat{v}_{top}$  and  $\hat{v}_{bot}$  and frequency  $f$  travel from the upper and the lower boundaries towards the flame. The superposition of these two traveling waves causes a standing wave in the combustion chamber. The acoustic pressure and acoustic velocity in such a standing wave have a phase difference of 90° in time and an offset by a quarter of the acoustic wave-length in space. The phase difference between the signal from the top and bottom sides,  $\Theta$  in eq. (5.2), affects the position of the acoustic velocity nodes and pressure nodes. In the pressure forcing case,  $\Theta$  is set to 0, so that the obtained standing wave has its pressure anti-node and its velocity node at

the center-line of the rectangular combustor. In the velocity forcing case,  $\Theta$  is set to  $\pi$ , so that the obtained standing wave has its pressure node and its velocity anti-node at the center-line of the rectangular combustor. The amplitudes of the ingoing waves  $\hat{v}_{bot}$  and  $\hat{v}_{top}$  (each 7 m/s) are chosen such that the maximum amplitude of the resulting standing wave is similar to the conditions in a real combustor and that the linearity between the pressure amplitude and the resulting heat release rate amplitude is ensured. These values correlate to a maximum pressure amplitude of about 2 % of the chamber operating pressure in the position of the acoustic pressure anti-node. The fact that the acoustic amplitudes/ energy inputs from the sides of combustor, used to generate the standing transverse wave, are the same in both cases, a comparison between results of pressure forcing and velocity forcing is possible and meaningful. To study the effect of the forcing frequency on the response of the flame, modulation is imposed at frequencies of 1250, 2500, 3750, 5000 Hz, in order to cover the common range of high-frequency instabilities observed in large industrial can-type combustors. To study the effect of mean flame length on the response of the flame at a forcing frequency of 2500 Hz, the flame length is modified by using different time averaged laminar flame speeds of 0.15, 0.2, 0.3, 0.4, 0.5, 0.6, 0.7, 0.8 m/s. Table 5.2 gives an overview of the 34 forced response simulations performed in the present study.

**Table 5.2** Overview of the operating conditions

| Forcing method   | $f$<br>kHz             | $S_l$<br>m/s                              | CPU effort<br>kh/Simulation | total CPU effort<br>kh |
|------------------|------------------------|---|-----------------------------|------------------------|
| Pressure forcing | 1.25, 2.5<br>3.75, 5.0 | 0.15, 0.2, 0.3, 0.4<br>0.5, 0.6, 0.7, 0.8 | 17                          | 200                    |
| Velocity forcing | 1.25, 2.5<br>3.75, 5.0 | 0.15, 0.2, 0.3, 0.4<br>0.5, 0.6, 0.7, 0.8 | 17                          | 200                    |

## 5.3 Modeling and Simulation

### 5.3.1 Combustion Model

A transport equation for the sub-grid turbulent kinetic energy  $k$  is solved, to account for the unresolved velocity fluctuations. To model combustion, a flame surface density approach [149] is used. The flame propagation is described by a transport equation for the density-weighted reaction regress variable ( $b = 1 - c$ ), where  $c$  is a more commonly used normalized progress variable. To calculate the field of the regress variable  $b$  for premixed conditions, the following transport equation is solved [102]:

$$\frac{\partial(\bar{\rho}\tilde{b})}{\partial t} + \frac{\partial\bar{\rho}\tilde{b}\tilde{u}_i}{\partial x_i} - \frac{\partial}{\partial x_i}\left(\frac{\mu_t}{Sc_t}\frac{\partial\tilde{b}}{\partial x_i}\right) = -\bar{w}_c + \frac{\partial}{\partial x_i}\overline{(\rho D\frac{\partial b}{\partial x_i})} = -\rho_u S_l \Sigma_{gen} \quad (5.3)$$

In the previous equation,  $\tilde{\phi}$  and  $\bar{\phi}$  represents density weighted filtering and filtering of a quantity  $\phi$ , respectively. The laminar flame speed and the density of the unburned mixture are denoted with  $S_l$  and  $\rho_u$ , respectively. The source term for  $b$  is identical to the source term  $\bar{w}_c$  for  $c$ , albeit with a negative sign. The source term and the molecular diffusion term combined can be modeled by the generalized flame surfaced density [108]:

$$\Sigma_{gen} = \Xi |\nabla \bar{b}| \quad (5.4)$$

The interaction between sub-grid turbulence fluctuations and combustion is determined by the sub-grid scale flame wrinkling factor  $\Xi$ , its modeling being inspired by Bradly et al. [111] as used in previous work at Siemens [63]:

$$\Xi = 1 + \frac{C}{Le} \sqrt{\frac{u'_{sgs} \Delta}{a_l}} \quad (5.5)$$

In the above equation, the wrinkling factor  $\Xi$  depends on the filter size  $\Delta$ , the Lewis number  $Le$  which is assumed to be unity, a model constant  $C$  and a sub-grid velocity fluctuation  $u'_{sgs}$  that is calculated using following eq. (5.6):

$$u'_{sgs} = \sqrt{\frac{2k}{3}} \quad (5.6)$$

The mean laminar flame speed  $S_{l0}$  is calculated using Cantera [113] for solving a freely propagating flame for the desired operating conditions. The changes of pressure ( $p = p_0 + p_1$ ) in the combustion chamber are mainly due to the acoustic forcing and are to be isentropic, the corresponding temperature can then be calculated from the isentropic relation  $T = T_0 (p/p_0)^{\frac{\gamma-1}{\gamma}}$ . The subscripts indicate the acoustic 1 and the mean variable 0. For a given equivalence ratio, the unstretched laminar flame speed ( $S_l = S_{l0} + S_{l1}$ ) can then be parametrized for the pressure. The relevant data was obtained by simulating one-dimensional, laminar freely propagating premixed flames using Cantera for a range of pressures from 7.2 bar to 8.8 bar, leading to flame speeds from 0.198 m/s to 0.206 m/s. A fit leads to the following dependency:

$$\frac{S_l}{S_{l0}} = 0.1855 \frac{p}{p_0} + 0.8145 \quad (5.7)$$

The above equation considers the change of laminar flame speed due to acoustic pressure change. Further changes in the turbulent flame speed result from the wrinkling factor.

The temperature is calculated iteratively from NASA polynomials [150] and a transport equation for the filtered specific absolute enthalpy  $\tilde{h}$ . The mixture is defined using the value of the regress variable as unburned reactants ( $b > 0.999$ ), burning (flame brush) ( $0.001 < b < 0.999$ ) and burned products ( $b < 0.001$ ). For the reactants and products the coefficients of the NASA polynomials for the desired equivalence ratio are

known. Within the flame brush, the coefficients are calculated using the regress variable from the coefficients of the polynomial  $a_i$  and the molecular weight  $W$  as:

$$\frac{a_{i,mi}}{W_{mi}} = \frac{\tilde{b}}{W_r} a_{i,r} + \frac{1 - \tilde{b}}{W_p} a_{i,p} \quad \text{for } i : 1 \text{ to } 6 \quad (5.8)$$

The subscripts  $mi$ ,  $r$  and  $p$  denote mixture, reactants and products, respectively. Finally, the temperature is calculated iteratively from eq. (5.9) using the Newton-Raphson method [151].

$$\frac{\tilde{h}W_{mi}}{R\tilde{T}} = a_{1,mi} + \frac{a_{2,mi}}{2}\tilde{T} + \frac{a_{3,mi}}{3}\tilde{T}^2 + \frac{a_{4,mi}}{4}\tilde{T}^3 + \frac{a_{5,mi}}{5}\tilde{T}^4 + \frac{a_{6,mi}}{\tilde{T}} \quad (5.9)$$

For the present study, a reacting, compressible large-eddy simulation is performed using the compressible version of OpenFoam with pressure implicit with splitting of operators pressure velocity coupling [152]. For the convection of momentum, a TVD scheme with Sweby limiter is used [116, 117], which is normally too dissipative for LES, but is very hard to avoid unless dedicated research codes are used [153]. For temporal discretization, a Crank-Nicolson based scheme [154] is used, with a linear blending coefficient of 0.8, where a value of 1 corresponds to the pure Crank-Nicolson method and 0 to the pure implicit Euler method [150]. The modeling and simulation methods were validated in previous work [63] and against experimental data for a similar combustor in the present study (see Appendix A). A grid refinement study (see Appendix B) showed that a cell-size of 1.33 mm and an acoustic Courant–Friedrichs–Lewy number of 0.7 are sufficient to predict the flame length, a crucial parameter for thermo-acoustic investigations.

### 5.3.2 Rayleigh Index and Budget Analysis

Thermo-acoustic instabilities occur due to the coupling of heat release rate oscillations and pressure oscillations. The Rayleigh Index [13] quantifies the susceptibility of a system to thermo-acoustic instabilities and reads:

$$RI = \frac{\gamma - 1}{\gamma p_0 t_p} \int_{t_p} \int_V p_1 \dot{q}_1 dV dt \quad (5.10)$$

The ratio of specific heats  $\gamma$  is assumed to be constant. The period of the acoustic oscillation is represented by  $t_p$ , the combustor volume by  $V$ . The Rayleigh Index has a positive value if the phase difference between the heat release rate oscillation and the pressure oscillation is between  $0^\circ$  and  $\pm 90^\circ$ , i.e. if heat is preferentially released during periods of increased pressure. In a combustion system, the heat release rate may oscillate through different mechanisms [155], including flame-vortex interactions, flame

surface modulation, equivalence ratio oscillations, chemical kinetic, density oscillations and flame-displacement [47, 46, 44, 138].

The local heat release rate in the context of the flame surface density model can be calculated from the heat of reaction per mass of fuel  $H$  and the fuel mass fraction  $Y_f$  in the reactants as [64]:

$$\dot{q} = \rho_u S_l \Xi |\nabla b| H Y_f \quad (5.11)$$

Since this study considers premixed combustion,  $Y_f$  is constant. Equation (5.11) can be linearized as:

$$\dot{q}_1 \approx \frac{\rho_{u1}}{\rho_{u0}} \dot{q}_0 + \frac{S_{l1}}{S_{l0}} \dot{q}_0 + \frac{\Xi_1}{\Xi_0} \dot{q}_0 + \frac{|\nabla b|_1}{|\nabla b|_0} \dot{q}_0 \quad (5.12)$$

By integrating both sides of eq. (5.12) over the volume, the global heat release rate oscillations are determined as outlined below:

$$\dot{Q}_1 = \int_V \dot{q}_1 dV \approx \underbrace{\int_V \frac{\rho_{u1}}{\rho_{u0}} \dot{q}_0 dV}_{\dot{Q}_\rho} + \underbrace{\int_V \frac{S_{l1}}{S_{l0}} \dot{q}_0 dV}_{\dot{Q}_{S_l}} + \underbrace{\int_V \frac{\Xi_1}{\Xi_0} \dot{q}_0 dV}_{\dot{Q}_\Xi} + \underbrace{\int_V \frac{|\nabla b|_1}{|\nabla b|_0} \dot{q}_0 dV}_{\dot{Q}_A} \quad (5.13)$$

The right hand side (RHS) of the equation features the heat release rate oscillation due to density oscillations  $\dot{Q}_\rho$ , due to the oscillations of laminar flame speed  $\dot{Q}_{S_l}$  and due to the oscillations of the sub-grid wrinkling factor  $\dot{Q}_\Xi$ . Assuming a negligible variation of the mean heat release rate within the flame brush, the last term  $\dot{Q}_A$  can be correlated to the oscillation of burning area using the assumption of the regress variable being monotonic over the flame, which relates the integral of the gradient of the regress variable to the burning area  $A$  as:

$$\int_V |\nabla b| dV = A \quad (5.14)$$

It should be noted, that  $\dot{Q}_A$  results primarily from the movement of the flame surface by transverse velocity perturbation and flame/vortex interaction, but that the local fluctuation of flame speed and wrinkling factor can affect it indirectly. To demonstrate that the proposed linearization concept is applicable, the phase averaged fluctuation of global heat release rate  $\dot{Q}_1$  (reference) computed from the source term in the LES (see eqs. 5.11 and 5.3) is compared with the summation of the right hand side of eq. 5.13 and shown for the entire forcing frequencies in Fig. 5.3 for both forcing methods. The integration is performed only over the upper half of the combustor, due to negligibly small amplitude of global heat release rate oscillation over the entire domain in the velocity forcing case. As it can be observed in Fig. 5.3, the linearization show a good agreement compared to the reference data, confirming its appropriateness.

By substituting the local heat release rate oscillation  $\dot{q}_1$  in eq. (5.10) with the RHS

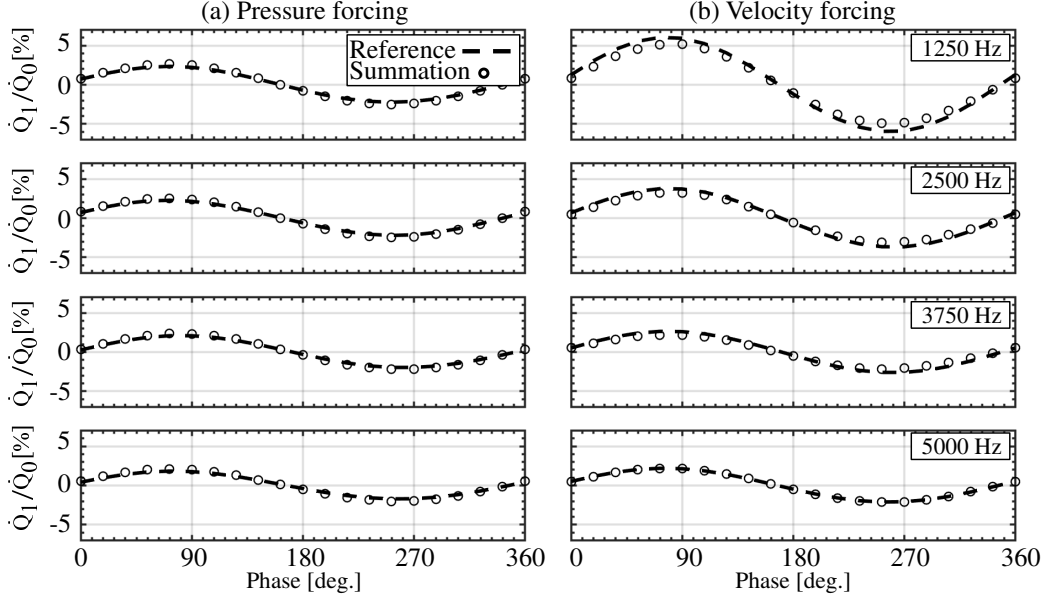


**Fig. 5.3** Comparison of the phase averaged normalized global heat release rate oscillation (reference) with the summation of RHS of eq. 5.13.

of eq. (5.12), one can compute the contribution of each term to the total Rayleigh Index:

$$\begin{aligned}
 RI \approx & \underbrace{\frac{\gamma - 1}{\gamma p_0 t_p} \iint_{t_p V} p_1 \frac{\rho_{u1}}{\rho_{u0}} \dot{q}_0 dV dt}_{RI_\rho} + \underbrace{\frac{\gamma - 1}{\gamma p_0 t_p} \iint_{t_p V} p_1 \frac{S_{l1}}{S_{l0}} \dot{q}_0 dV dt}_{RI_{S_l}} + \\
 & \underbrace{\frac{\gamma - 1}{\gamma p_0 t_p} \iint_{t_p V} p_1 \frac{\Xi_1}{\Xi_0} \dot{q}_0 dV dt}_{RI_\Xi} + \underbrace{\frac{\gamma - 1}{\gamma p_0 t_p} \iint_{t_p V} p_1 \frac{|\nabla b|_1}{|\nabla b|_0} \dot{q}_0 dV dt}_{RI_A}
 \end{aligned} \tag{5.15}$$

As a result, the global Rayleigh Index ( $RI$ ) is the sum of the Rayleigh indices of the contributions from density oscillations ( $RI_\rho$ ), laminar flame speed oscillations ( $RI_{S_l}$ ), wrinkling factor oscillations  $RI_\Xi$  and flame area oscillations ( $RI_A$ ). The Rayleigh index contribution ( $RI_A$ ), resulting from flame area oscillation, includes the flame displacement mechanism proposed by the Sattelmayer group [47, 46, 44] by accounting for the area changes due to transverse acoustic velocity. It must be stressed that ( $RI_\Xi$ ) is affected by the sub-grid turbulence model (eq. 5.5), which was not developed to consider the effect of high-frequency pressure perturbations.

To calculate the contributions to the Rayleigh Index, the respective oscillations are phase averaged at the forcing frequency and are then used for evaluating different terms of eq. (5.15). To ensure the applicability of this decomposition of the Rayleigh Index, a consistency check was conducted with pressure forcing and velocity forcing at 2500 Hz. For this purpose, the global Rayleigh Index was first computed according to the

definition in eq. (5.10) and then from the RHS of eq. (5.15), leading to values of 88.7 W and 91.5 W with pressure forcing and of 65.8 W and 62.8 W with velocity forcing. The linearization and decomposition of the Rayleigh Index has hence led to deviations smaller than 4%, confirming the suitability of the method.

## 5.4 Results

A reference simulation (see Appendix A) without acoustic modulation was carried out first using operating conditions given in table 5.1, which results in a jet-Reynolds number of  $8 \cdot 10^5$ . The simulation did not show any self-excited thermo acoustic instabilities; the standard deviation of the spatially integrated heat release rate was 2% of the mean value.

### 5.4.1 Comparing Pressure Forcing and Velocity Forcing

We first illustrate and compare the results of the pressure forcing and velocity forcing at a frequency of 2500 Hz. Phase averaged fields of unsteady pressure are shown in Fig. 5.4 at four phases during one period of the pressure forcing and velocity forcing, where  $\langle \rangle$  denotes the phase averaging over at least 5000 periods.

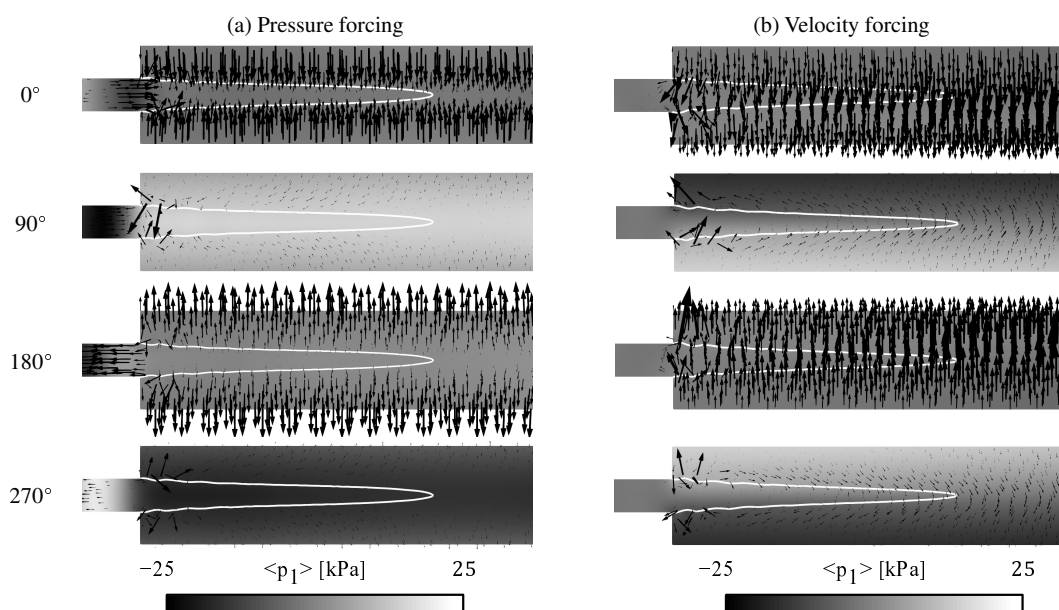


**Fig. 5.4** Phase averaged fields of the unsteady pressure and velocity vectors and the contour of the phase averaged regress variable,  $\langle b \rangle = 0.5$ .

With pressure forcing, a pressure anti-node and velocity node along the center-line of the combustion chamber are created. At  $0^\circ$ , the acoustic transverse velocity in the upper half and in the lower half of the combustion chamber is directed towards the center-line of the chamber. The pressure increases in the flame region and reaches

its maximum at the center-line of the chamber at  $90^\circ$ ; at  $180^\circ$ , the acoustic transverse velocity is directed outwards; at  $270^\circ$ , the pressure reaches its minimum at the center-line of the combustion chamber.

With velocity forcing, the out-of-phase modulation of the velocity at the sides of the chamber leads to a pressure node and a velocity anti-node along the center-line of the combustion chamber. At  $0^\circ$ , the acoustic transverse velocity in the flame region is directed downwards and has its maximum at the center-line; at  $90^\circ$ , the acoustic pressure in the lower half of the combustion chamber reaches its maximum, and the pressure in the upper half reaches its minimum; at  $180^\circ$ , the acoustic velocity is directed upwards and has its maximum at the center-line; at  $270^\circ$  the acoustic pressure is at its maximum at the upper half and is at its minimum at the lower half of the chamber.

To emphasize the resulting change in the flame shape, the flame is visualized by  $\langle b \rangle = 0.5$  at  $90^\circ$  and at  $270^\circ$  in Fig. 5.5a for the pressure forcing and in Fig. 5.5b for the velocity forcing. The dynamic behavior of the flame with pressure forcing can be described as a superposition of symmetrical vortex shedding at the duct outlet and the transverse contraction and expansion of the flame, termed as flame-breathing. The dynamic behavior of the flame with velocity forcing can be described as asymmetrical vortex shedding from the duct outlet and the up and down shifting of the flame, termed as flame-displacement.

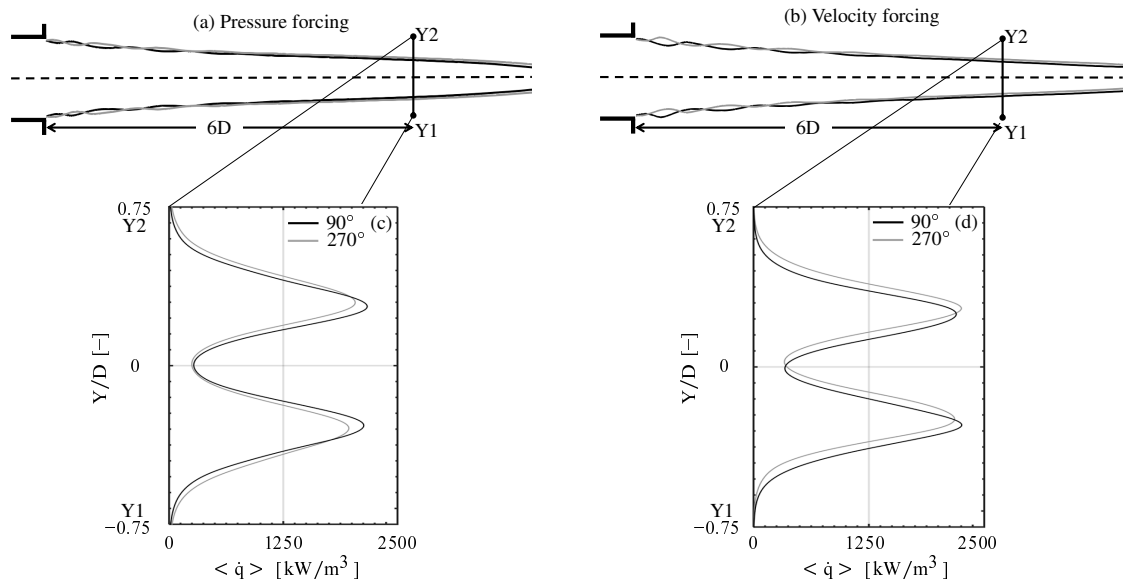


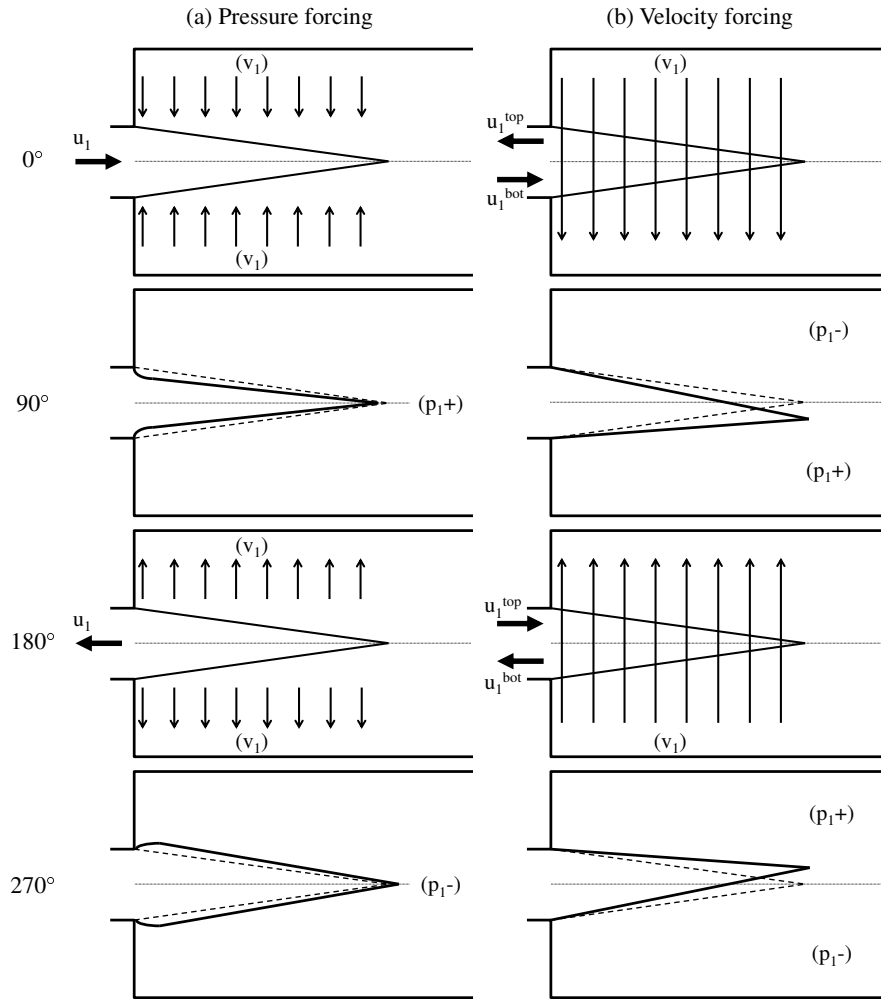
**Fig. 5.5** Phase averaged contour of the regress variable,  $\langle b \rangle = 0.5$  (top) and phase averaged local heat release rate along the Y1-Y2 line (bottom);  $90^\circ$ : black curve,  $270^\circ$ : gray curve.

In Figs. 5.5c and 5.5d, the local heat release rate is plotted along a line, six jet diameters downstream of the duct outlet at  $90^\circ$  and at  $270^\circ$  with pressure forcing and velocity forcing. At this position, the vortical pattern is diminished. Comparing the local heat

release rate at  $270^\circ$  and  $90^\circ$  with pressure forcing, two effects can be observed: (a) a contraction of the flame towards the center-line of the burner, and (b) an increase in the maximal local heat release rate which can be related to the increase in the local density and laminar flame speed (see eq. 5.7) in the flame region due to the increased acoustic pressure. With velocity forcing, it can be seen that from  $90^\circ$  to  $270^\circ$  (a) the entire flame is shifted from the lower half to the upper half of the chamber and (b) the maximum of the local heat release rate is decreased in the lower half of the chamber and increased in the upper half of the chamber. The change in the local heat release rate is related to the associated changes in the local density and the laminar flame speed.

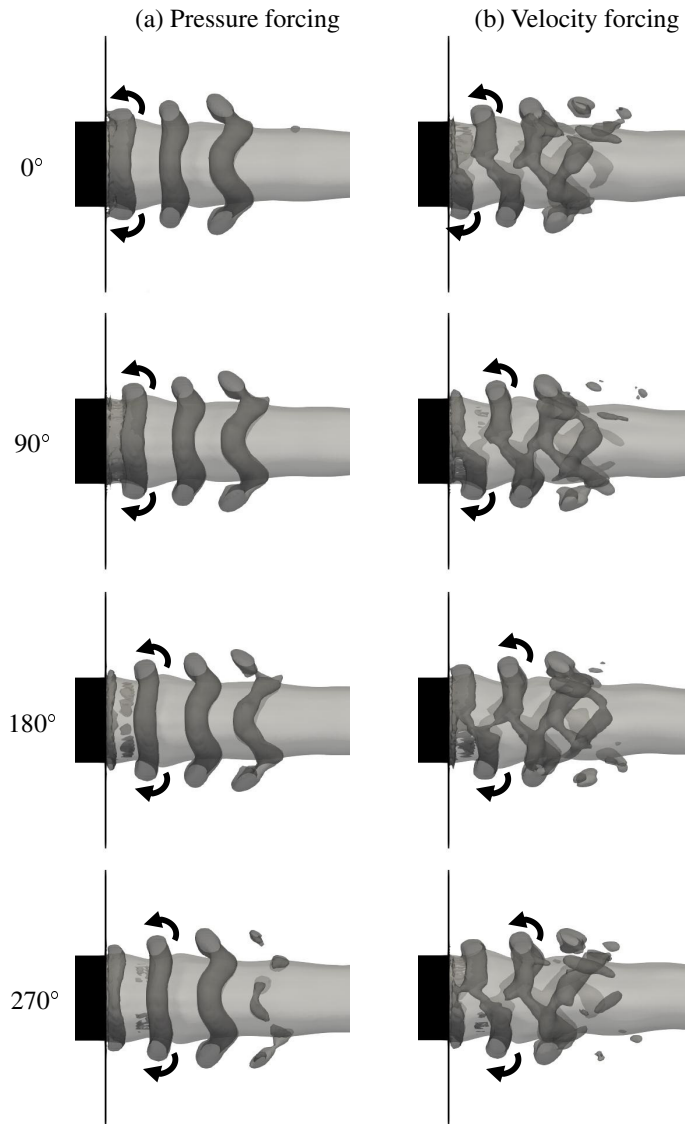
The next two paragraphs explain the flame-breathing in the case of pressure forcing and the flame-displacement in the case of velocity forcing by the mean of the flame shape changes using the simplified schematic in Fig. 5.6, ignoring variation in the flame wrinkling resulted by the axial velocity oscillation at the duct outlet. The flame-displacement mechanism is well known [44, 45, 46, 138], but we focus on the flame surface modulation caused by it.

Figure 5.6a shows the flame at four phases with pressure forcing. At  $0^\circ$ , the acoustic transverse velocity is oriented towards the center-line of the chamber, causing the flame to contract, reaching a flame surface minimum at  $90^\circ$ . At  $90^\circ$ , the acoustic pressure, the density and the laminar flame speed reach their maximum. The decrease in the flame surface causes a reduction in the global heat release rate, but the increase in the density and laminar flame speed increases the local and global heat release rate. At  $180^\circ$ , the acoustic transverse velocity is directed outwards. This leads to an expansion of the flame at  $270^\circ$ . When the flame surface reaches its maximum, the acoustic pressure, density and laminar flame speed reach their minimum in the flame region. The increase of the flame surface increases the global heat release rate, but the decrease in the density and the laminar flame speed decrease the local and global heat release rate. In other words, with pressure forcing, the density and the laminar flame speed oscillations are in phase with pressure oscillations, whereas the flame area modulation due to contraction and expansion (flame-breathing) is out-of-phase with pressure oscillations. Figure 5.6b shows the flame at four phases with velocity forcing. At  $0^\circ$ , the acoustic transverse velocity is directed downwards and pushes the flame down. At  $90^\circ$ , the acoustic pressure reaches its maximum in the lower half of the chamber and its minimum in the upper half. Hence, the density is highest in the lower half of the combustor and lowest in the upper half. At this phase ( $90^\circ$ ), the flame surface located in the lower half of the combustion chamber is bigger than at  $0^\circ$  and the flame surface located in the upper half is smaller than at  $0^\circ$ . From  $180^\circ$  to  $270^\circ$ , the acoustic transverse velocity shifts the flame upwards, until the biggest part of the flame surface is in the upper half of the chamber, where the pressure and density have reached their highest values, while the flame surface area, pressure and density in the lower half have reached their minima. In other words, with



**Fig. 5.6** Illustration of the flame shape changes due to the acoustic transverse velocity, ignoring variation in the flame wrinkling. The position of the time averaged flame is highlighted with dashed lines.

velocity forcing, the flame area, the density and the laminar flame speed oscillations in the upper and lower half of the combustor are in-phase with pressure oscillations. To visualize the periodical vortex shedding at the duct outlet, the  $Q$ -criterion [156] is applied, showing regions with  $Q > 0$  in Fig. 5.7 for four phases during the forcing (for the associated pressure see Fig. 5.4), together with the 0.5-isosurface of the regress variable. The vortex shedding frequency is calculated by using the Fourier transformation of the transverse velocity near the duct outlet in both forcing cases. It is observed that the vortices are shed from the duct outlet with the same frequency as the forcing frequency, as expected. With pressure forcing, vortices are shed symmetrically; with velocity forcing vortices separate with an offset from the upper and lower sides of the duct outlet. The reason of this behavior can be found by looking at the axial velocity modulation in the duct in Fig. 5.6. In general, transverse pressure oscillations in the combustor send axial waves towards the duct. With pressure forcing, the pressure os-



**Fig. 5.7** Phase averaged  $Q$ -isosurface; the dark gray isosurface corresponds to the isosurface of  $\langle Q \rangle = 5 \cdot 10^7 \text{ s}^{-2}$  and light gray to the isosurface of  $\langle b \rangle = 0.5$ . Arrows mimic the rotation direction.

cillates with a uniform phase in the combustor, but with velocity forcing, there is a  $180^\circ$  phase difference between the pressure signal in the upper and lower halves of the combustor (see Fig. 5.6). This results in a uniform modulation of the acoustic axial velocity  $u_1$  in the duct for pressure forcing, and an out-of-phase modulation in the upper and the lower parts of the duct (see  $u_1^{\text{top}}$  and  $u_1^{\text{bot}}$ ) for velocity forcing. The symmetrical and asymmetrical vortex shedding was observed for flames with different shapes (e.g. V-Flame, swirl flame) as well [48, 143, 21], indicating that this behavior does not depend on flame shape. The vortex rings are moving downstream at approximately 50 m/s (at the excitation frequency of 2500 Hz). Thus, the ratio of the vortex ring's displacement time (from the duct outlet to the flame tip) to the excitation period can be estimated to be 16. In the present study, the effect of vortex shedding on the flame is coupled

with flame-displacement and flame-breathing mechanisms, making it hard to isolate the effect of vortex shedding on thermo-acoustic instability. However, the vortex shedding is mainly due to modulation of the axial velocity as mentioned earlier. We assume that the effect of vortex shedding at high-frequency with pressure forcing can be neglected as it is well known that the flame transfer function of an axially modulated flames have a low-pass behavior [141, 142, 138, 157, 138, 146, 67, 88]. The overall contributions of flame/vortex interaction (even, if it is small), flame-displacement and flame-breathing to the instabilities of the system are captured together using ( $RI_A$ ) and discussed.

#### 5.4.2 Effect of Forcing Frequency

The effect of the forcing frequency on the flame shape is illustrated in Fig. 5.8, showing contours of the phase averaged regress variable at  $90^\circ$  and  $270^\circ$ . When the frequency is increased, the waves generated in the flame-front get a smaller wavelength and disappear already further upstream; the flame-breathing and flame-displacement in both forcing cases decrease. This effect of higher frequencies can be explained by the reduced period of the forcing, so that the transverse velocity, which causes the flame-breathing and displacement, acts over a shorter time, leading to a smaller displacement of the flame. The amplitude of different contributions to the heat release rate oscillation

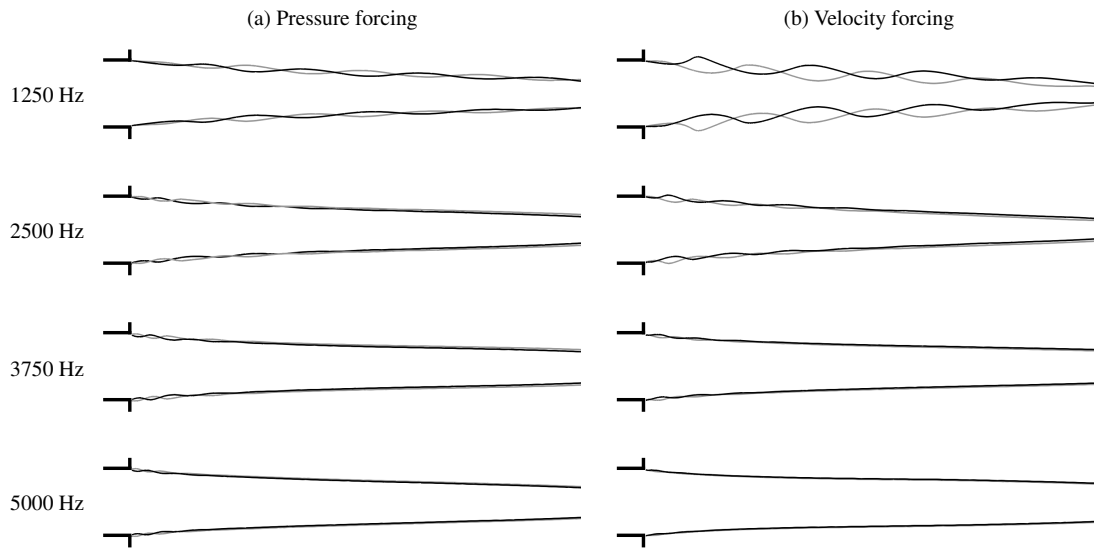


**Fig. 5.8** Phase averaged contours of the regress variable,  $\langle b \rangle = 0.5$ , at  $90^\circ$  (black curves) and  $270^\circ$  (gray curves).

based on the decomposition presented in eq. (5.13) are illustrated in Fig. 5.9 (top). Only the volume integral of the upper half of the combustor is considered. This is because the total heat release rate over the volume of the upper and the lower parts of the combustor are out-of-phase with velocity forcing, as the flame is just shifted "up and down". For computing the amplitudes, acoustic variables in eq. (5.13) are phase averaged. The

amplitude is then estimated using a harmonic fit. The results are then normalized with the mean heat release rate over the same integration volume. The phase differences be-

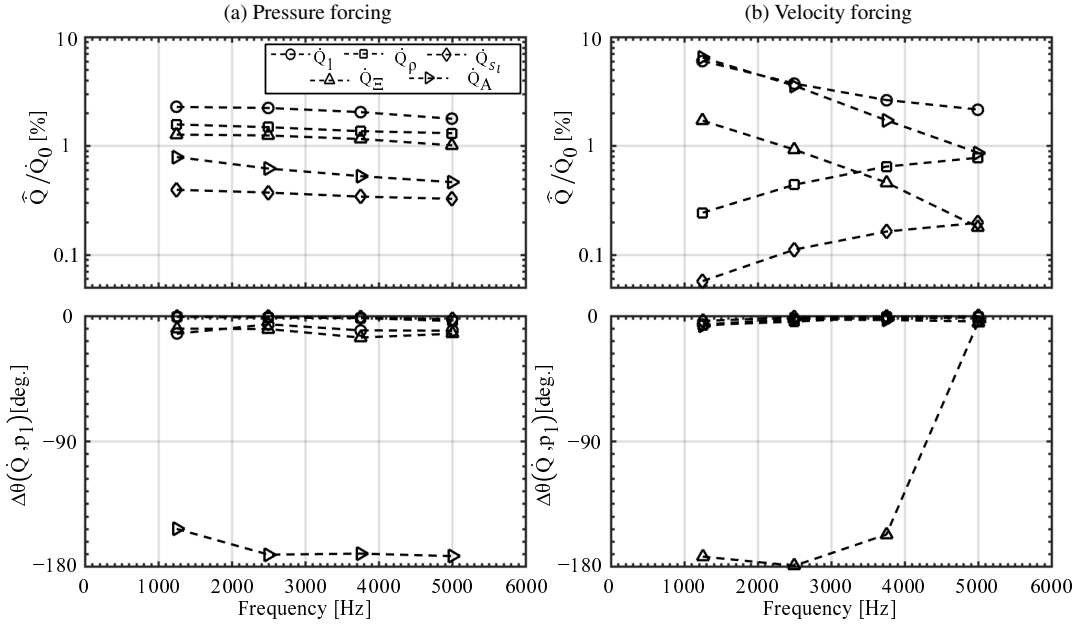


**Fig. 5.9** Normalized amplitude of the global heat release rate oscillation due to respective contributions (top) and their phase difference with pressure oscillations (bottom).

tween the phase averaged pressure signal at a point in the upper half of the combustor volume and the respective contributions to the heat release rate oscillation are shown in Fig. 5.9 (bottom). It can be seen that the spatially integrated heat release rate  $\hat{Q}_1$  (computed from the source term in the LES) has a higher amplitude with velocity forcing. With pressure forcing, the total heat release rate amplitude  $\hat{Q}_1$  and the amplitude of different contributions  $\hat{Q}_\rho$ ,  $\hat{Q}_{S_L}$ ,  $\hat{Q}_\Xi$  and  $\hat{Q}_A$  monotonically decrease, with the term  $\hat{Q}_\rho$  having the highest value. The phase difference between the acoustic pressure oscillation and the respective contributions (except for  $\hat{Q}_A$ ) is less than  $90^\circ$ , indicating a destabilizing coupling. The heat release rate due to the burning area modulation  $\hat{Q}_A$  oscillates out-of-phase with pressure, indicating a stabilizing coupling.

With velocity forcing, the contribution of the burning area oscillation  $\hat{Q}_A$  has the highest amplitude, especially at relatively low frequencies. At higher frequencies, the amplitude of the contribution of density  $\hat{Q}_\rho$  and laminar flame speed  $\hat{Q}_{S_L}$  increases. The reason for this could be found by looking at the transverse acoustic pressure distribution at the upper half of the combustor for different forcing frequencies as shown in Fig. 5.10 (right). With increasing frequency (decreasing wavelength), the pressure anti-node moves towards the flame brush, subjecting it to a higher pressure amplitude. In turn, the amplitude of density and laminar flame speed oscillations increases at the flame position, leading to an increase in  $\hat{Q}_\rho$  and  $\hat{Q}_{S_L}$  with frequency. With velocity forcing, the phase difference of pressure and respective contributions to the heat release rate is

less than  $90^\circ$  (except for  $\hat{Q}_\Xi$ ), revealing the destabilizing effect.

The pressure amplitude at the location of the flame brush decreases with frequency in the pressure forcing case, as shown in Fig. 5.10 (left), but the change is not as significant as in the velocity forcing case (right). Accordingly the  $\hat{Q}_\rho$  and  $\hat{Q}_{S_l}$  curves are shallower with pressure forcing, as illustrated in Fig. 5.9 (top left). To illustrate how

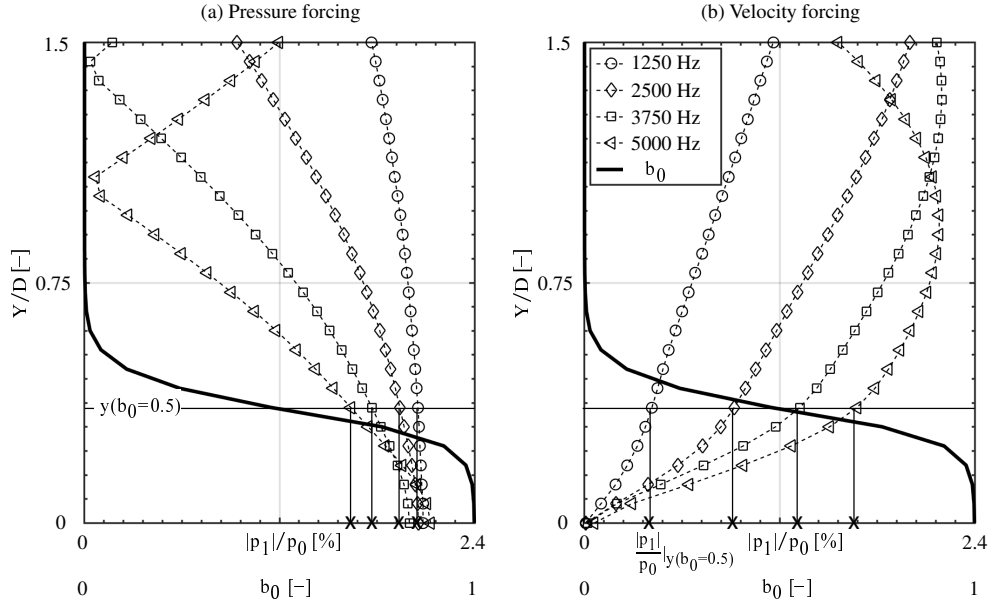


**Fig. 5.10** Acoustic transverse pressure distributions at  $90^\circ$  and mean regress variable at the upper half of the combustor over a transverse line six jet diameter downstream of the duct outlet.

different mechanisms contribute to the Rayleigh Index, the Rayleigh Index of each contribution is shown in Fig. 5.11 as a function of the frequency for both forcing scenarios. The flame has a higher Rayleigh Index with pressure forcing than with velocity forcing, indicating that not only the amplitude of heat release rate oscillation (discussed above) but also the amplitude of local pressure is essential to estimate the contribution of the heat release rate oscillation on the instability of the system. For the can-type combustor described in the introduction (see Fig. 5.1), this would mean that a flame positioned near a pressure anti-node and velocity node could contribute more to the acoustic instability of the system than a flame that is positioned near the velocity anti-node and the pressure node.

With pressure forcing, Fig. 5.11a shows how the total Rayleigh Index  $RI$  decreases with increased forcing frequency and that  $RI_\rho$ ,  $RI_{S_l}$  and  $RI_\Xi$  are positive, while  $RI_A$  is negative for all forcing frequencies. This indicates that oscillations in density, laminar flame speed and wrinkling factor destabilize, whereas the flame surface oscillations have a stabilizing effect. The contribution of the density oscillations  $RI_\rho$  can be seen as the main driving mechanism in this case.

With velocity forcing, Fig. 5.11b reveals that the total Rayleigh Index remains al-

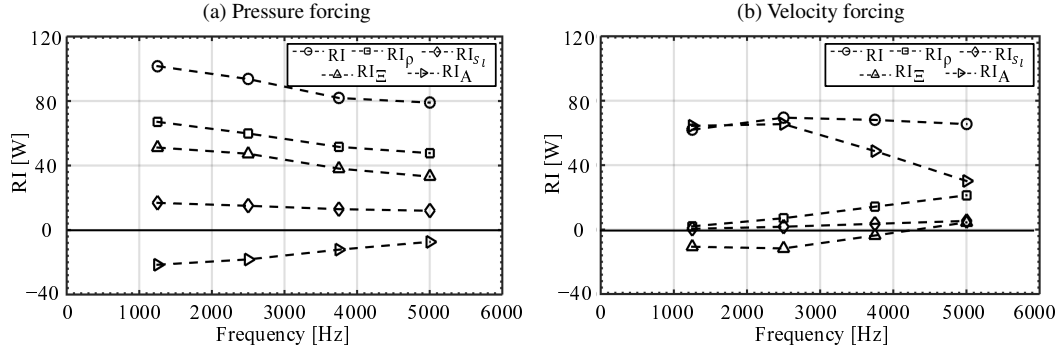


**Fig. 5.11** Total Rayleigh Index and the Rayleigh Indices of different contributions over forcing frequencies.

most constant for all frequencies and that  $RI_A$  has the highest (destabilizing) contribution to the total Rayleigh Index. The change in flame surface within the top- and bottom half of the combustor can be therefore identified as the main driving mechanism, especially at lower forcing frequencies. In this case, the value of  $RI_A$  decreases with increasing forcing frequency. In contrast, the effect of density ( $RI_\rho$ ) and laminar flame speed ( $RI_{S_l}$ ) increases with frequency, due to the higher pressure amplitude acting on the flame brush at higher frequency, as shown in Fig. 5.10 (right).

Weaker contributions to the total Rayleigh Index are due to the wrinkling factor ( $RI_E$ ) and the laminar flame speed ( $RI_{S_l}$ ), as also shown in Fig. 5.11. The effect of acoustic pressure on the laminar flame speed increases the total Rayleigh Index by at least 15 % with pressure forcing, and 2 % with velocity forcing and is expected to remain positive with increasing frequency, until the acoustic time-scale becomes comparably short as the chemical time-scale - which would require further investigations. The contribution of the wrinkling factor oscillations  $RI_E$  is positive with pressure forcing and negative with velocity forcing (except for 5000 Hz). The reason for this behavior is not clear yet and needs to be investigated further. It should be noted that a) there may also be an effect of sub-grid turbulence models, which are rarely designed to correctly consider the effect of (relatively weak) high-frequency pressure oscillations, that b) the mechanisms identified in this section may not be applicable to other types of flames (e.g. V-flames and swirled flames), and that c) in real experiments, results may be affected by the acoustic impedance of the upstream features.

### 5.4.3 Effect of the Flame Length on the Rayleigh Indices

The effect of the flame length on the instability is often discussed, but it is hard to alter the flame length in a realistic burner. In the present case, the flame length is modified by scaling the laminar flame speed, but it must be stressed that this scaling may have side-effects, so that the findings can only be considered as an indication for

the effects of flame length. The laminar flame speed is multiplied with factors from 0.75 to 4, shortening the flame accordingly. After conducting the reference simulations with each modified laminar flame speed without acoustic modulation, the flame is excited with a forcing frequency of 2500 Hz. The normalized Rayleigh Index, as a function of the normalized flame speed and resulting flame length, is plotted in Fig. 5.12. The Rayleigh Indices are normalized using the associated mean global heat release rates, calculated by integrating eq. 5.11 over the entire combustor volume of the reference simulations. The label of Fig. 5.12 also shows the resulting normalized mean flame length achieved by the non-forced simulations with respect to their laminar flame speed.

With pressure forcing, the total Rayleigh Index of the system first increases and then decreases with increasing flame length, implying that a flame speed and hence a flame length may exist that leads to the maximum instability for flames located in the pressure anti-node. With pressure forcing, the normalized  $RI_\rho$  and  $RI_{S_i}$  are almost constant for the studied flame speeds and flame lengths. The change in the normalized total Rayleigh Index is mainly due to the change in the contribution of the burning area oscillations  $RI_A/\dot{Q}_0$ . Most importantly, the change in the flame speed and flame length does not change the relative importance of the different mechanisms: the density oscillation remains to be the main driving mechanism and the area oscillation the main damping mechanism for all flame speeds and flame lengths.

With velocity forcing, the total Rayleigh Index first increases sharply before apparently reaching an asymptotic value for low flame speeds and long flames. For all flame speeds and flame lengths,  $RI_A/\dot{Q}_0$  makes the highest contribution and the main driving mechanism remains the change in flame surface changes within the top- and bottom half of the combustor, while other mechanisms are not a function of flame speed and length.

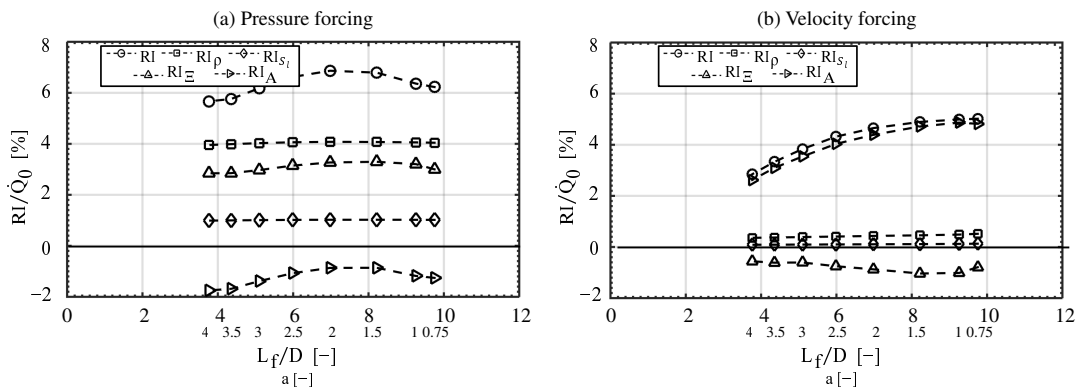


**Fig. 5.12** Normalized Rayleigh Index over the normalized flame length at 2500 Hz. The mean laminar flame speed for each simulation is scaled by the factor  $a$ .

## 5.5 Conclusion

In this work, forced response simulations were used to study mechanisms for thermo-acoustic instabilities in a Bunsen-type flames. Two forcing methods were utilized — pressure forcing with the flame located in the pressure anti-node and velocity forcing with the flame located in the velocity anti-node. The Rayleigh Index was calculated for both forcing methods to compare the thermo-acoustic susceptibility of the flame. The Rayleigh Index was higher for the flame positioned in the pressure anti-node (pressure forcing). It was also found that the sensitivity of the flame to thermo-acoustic instabilities decreased for higher excitation frequencies with pressure forcing, while there was almost no dependency of the Rayleigh Index on the forcing frequency in the case of velocity forcing. A method was presented to quantify the contributions of the mechanisms that gave rise to heat release rate oscillations. With pressure forcing, density oscillations were identified to be the main driving mechanism and flame-breathing was identified as the main stabilizing mechanism. The driver with velocity forcing was the flame-displacement mechanism, while the contribution of the density mechanism increased for higher excitation frequencies, since the flame brush faced higher acoustic amplitudes as the wavelength decreased. The destabilizing displacement-mechanism [44, 158, 46, 47] and the stabilizing flame-breathing mechanism, were explained by the change in the flame area.

To study the effect of laminar flame speed oscillations on flame instabilities, a simple model was introduced that considers acoustic pressure oscillation in the calculation of laminar flame speed, leading to destabilizing effects for both forcing methods, whereby the destabilization was higher with pressure forcing. Finally, the laminar flame speed was altered to obtain some evidence how the flame length may affect instability. With pressure forcing, a specific flame speed and flame length was found to show the highest Rayleigh Index. With velocity forcing, lower laminar flame speeds and longer flames were more prone to high-frequency instabilities.

## Acknowledgments

The authors gratefully acknowledge, the financial support of the state of North Rhine-Westphalia and the German Ministry of Economics and Technology (BMWi) for the collaborative project "Untersuchung der Entstehungsmechanismen zu Hochfrequenzinstabilitäten" of the Clean Energy Center (CEC) stage 2 (Project funding reference number 03ET7011L), as well as the computing time granted by the Center for Computational Sciences and Simulation (CCSS) of the University of Duisburg-Essen and provided on the supercomputer magnitUDE (DFG grant INST 20876/209-1 FUGG) at the Zentrum fuer Informations- und Mediendienste (ZIM).

## CHAPTER 6

### **High-Frequency Instabilities in a Cylindrical Single-Jet Combustion Chamber**

*This chapter including all figures and tables was previously published in 29. german flame day, V. Sharifi, C. Beck and A. M. Kempf, High-Frequency Instabilities in a Cylindrical Single-Jet Combustion Chamber [159]. The author V. Sharifi ran all simulations, wrote the paper and generated all figures and tables. The authors C. Beck and A. M. Kempf contributed corrections, discussions and proofreading.*

The investigation of high-frequency thermoacoustic instabilities (HFI) reveals a lack of simple experiments with acoustically well-defined boundary conditions relevant for state of the art stationary gas turbines. The present work aims to design a suitable atmospheric combustion chamber aided by Large-Eddy Simulations (LES) for future HFI-experiments. The starting point was a simple adiabatic cylindrical combustion chamber with perfectly premixed flame, whose complexity was gradually increased to a feasible experiment. Previous forced-response investigations on a jet-stabilized flame showed that a flame located in the pressure anti-node can be coupled most strongly with pressure oscillations. In order to reproduce a similar flame/acoustic interaction in a self-excited configuration, the flame was arranged in the middle of a cylindrical chamber. This made it possible to excite acoustic radial modes of the system, which generated a pressure anti-node at the flame position. The diameter of the chamber was chosen such that the first radial mode has a frequency of 3 kHz, a frequency which is often observed in real gas turbines during HFI. In the adiabatic combustion chamber, the equivalence ratio was first varied ( $\theta = 0.6, 0.7, 0.8, 0.9$ ) until high-frequency oscillations with a significant amplitude occurred. For  $\theta = 0.7$ , oscillations with an amplitude of more than 4 kPa were observed in the first acoustic radial mode of the system. For the higher equivalence ratios of  $\theta = 0.8$  and  $0.9$ , additional instabilities were observed in the second acoustic radial mode. For realistic combustion chamber wall temperatures of 1100 K, the system had stabilized at  $\theta = 0.7$ , whereas at  $\theta = 0.9$  the instabilities had disappeared in the second radial mode and HFI occurred mainly in the first acoustic radial mode. Based on the findings on the temperature influence on the instabilities, a geomet-

ric modification was proposed which could successfully dampen the instabilities. The use of a realistic upstream plenum was required to study the system experimentally. Different geometries inspired by the experimental setup, corresponding to hard and soft acoustic boundary conditions for the combustion chamber, were used. It was observed that with harder acoustic boundary conditions the amplitudes of instabilities increased. This effect was not observed for the downstream boundary conditions. The influence of the consideration of non-ideal premixing on the HFI appearance was also investigated. If the reactants were not perfectly premixed, the instabilities showed an increase in amplitude, but the acoustic mode shape was not affected. A configuration susceptible to high-frequency instabilities was proposed based on the LES studies which satisfies the experimental requirements and is currently being investigated by experiment.

## 6.1 Introduction

Thermoacoustic instabilities are one of the main problems for further advances in lean premixed low NO<sub>x</sub> gas turbine combustion systems. These instabilities are caused by the coupling of heat release fluctuations and the resonances of the combustion chamber and are destructive in nature. They limit the operating range and performance of gas turbines and increase their emissions [23]. HFI are less investigated, mainly due to lack of simple reliable experimental test cases. Sjunesson et al. [18, 160] investigated the thermoacoustic behavior of a bluff-body stabilized propane premixed flame in a rectangular combustion chamber at Volvo in Sweden. High-frequency oscillations with a frequency of 1400 Hz were observed for a certain operating condition. The Schlieren images showed a periodic symmetrical vortex shedding from the top and bottom of the flame holder. It should be noted that the mode shape was not addressed in the experiment and that the symmetrical flow pattern may be due to the pure longitudinal mode, as reported by other authors [61, 161, 162]. Schwing et al. [21, 44] investigated the excitation mechanisms in an atmospheric, self-excited cylindrical combustor with a premixed flame. They varied the swirl number, the preheating temperatures and the mass flows in order to investigate their influence on the occurrence of instabilities. For all operating conditions they observed first transverse instabilities with frequencies between 2400 and 3400 Hz with an amplitude greater than 1 kPa by exceeding a critical equivalence ratio. The flame vortex interaction, the flame displacement mechanism and density mechanism were proposed to be important mechanisms for the observed instabilities [21, 47, 46]. It should be noted that the type of flame stabilization (e.g. vortex-stabilized, bluff-body stabilized, jet-stabilized) can have a decisive influence on the thermoacoustic mechanisms that can cause the instabilities [70]. A swirl-stabilized flame is therefore not necessarily a suitable test case for investigating the flame dynam-

ics of a jet-stabilized flame, which is the method of flame stabilization in the combustor of the new generation of Siemens heavy-duty gas turbines. Buschhagen et al. [53, 52] developed a cylindrical single-jet combustion chamber with premixed flame at a pressure of 700 kPa, which tends to exhibit HFI. A choked orifice plate and a choked nozzle on upstream and downstream acoustically separated combustion chambers from the rest of the test facility. The experiment showed pressure fluctuations in the range between 4.8 and 6.5 kHz, the mode shape of which was not addressed experimentally. Although this test case could be the ideal starting point for the investigation of HFI, there are some doubts about the observed instabilities. There is no operating condition with stable combustion reported from the experiment. This raises the issue that the observed instabilities may have only occurred because of acoustically blocked inlet and outlet, leading to minimization of acoustic fluxes through the combustion chamber boundaries and accumulation of acoustic energy regardless of flame/acoustic coupling.

## 6.2 Design Process of the Generic Configuration

The following section describes the design process and the criteria from the experimental and computational point of view that the self-excited HFI test case must satisfy. One of the requirements for the test case is the use of atmospheric combustion in order to reduce the costs of the experimental investigation by using the available atmospheric test facility in the Siemens laboratory. Forced-response studies on a jet-stabilized flame [35] revealed that the Rayleigh index, as measure of susceptibility of the flame to thermoacoustic instabilities, was highest for the flame positioned in the pressure anti-node, evidencing that the flame in pressure anti-node amplifies the high-frequency instabilities more strongly. To reproduce such a flame/acoustic interaction, the flame was positioned in the center of a cylindrical chamber. Assuming an axisymmetric behavior of the flame, it is more likely that the acoustic radial Eigenmode of the combustion chamber is excited in such a configuration. Thus the flame is positioned in the acoustic pressure anti-node. In order to avoid extremely long flames and the associated decrease in the coupling capability of the flame [35], a turbulence generator inspired from the technical system was applied. This type of turbulence generator is characterized by a high shear rate and no uniform swirl rotation. The duct diameter  $D$  was chosen such to mimic the fluid dynamical effect in a technical combustion chamber. The Eigenfrequency of the first pure radial Eigenmode (R1) in a cylindrical chamber with a diameter  $D_c$  can be estimated using the speed of sound  $c$  from the following equation:

$$f = \frac{\beta_{R1}c}{D_c} \quad (6.1)$$

where  $\beta_{R1} = 1.22$  is the characteristic value of the Bessel function of the R1 mode.

The diameter of the cylindrical combustion chamber has been chosen so that the R1 mode of the chamber has a frequency of 3 kHz at an assumed chamber temperature of 2000 K. Around this frequency, HFI are often observed in real gas turbines. As there is no information about the reflection coefficients at the boundaries of the system at this stage of the design, assumptions were made. To reduce the influence of acoustic boundary conditions, a downstream plenum inspired by the test facility was used to place the outlet far from the chamber. A generic plenum was also introduced on the upstream side. However, it will be shown later that the acoustic behavior of upstream plenum can crucially influence the appearance of HFI. Figure 6.1 illustrates the sketch of the generic combustion chamber (SiGenUDE) designed on the basis of the above assumptions and criteria. It consists of an upstream plenum, a premix duct, a turbulence generator, a cylindrical chamber, a downstream plenum and an exhaust gas channel. The outlet of the system is placed at the end of a chimney (not shown in the figure) and is 60 D downstream.

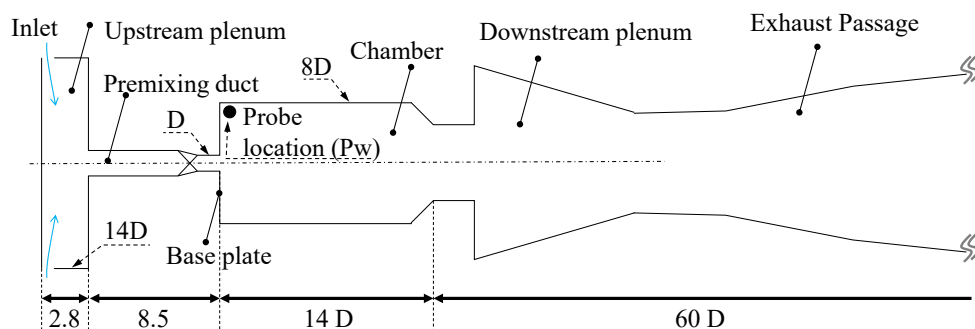


**Fig. 6.1** Schematic of SiGenUDE.

### 6.3 Modeling and Simulation

We performed a compressible reactive LES with the implicit open source code OpenFOAM [145]. A compressible version of the PISO pressure velocity coupling is employed [152]. Convection of momentum is discretized using a total variation diminishing scheme, filtered Linear [163]; The temporal discretization is done by the Crank–Nicolson scheme [123]. The computational domain was discretized in 14M cells with a cell size of 1 mm in the flame zone and 2 mm in the rest of the cylindrical chamber. The cell sizes in the cylindrical chamber and in the premixing duct were selected to guarantee at least 130 cells over a wavelength of the desired R1 mode. The time step was based on the acoustic CFL criterion equal to 0.3 in the flame region. A transported sub-grid kinetic energy model [164] was employed to model the sub-grid stresses. The inlet boundary condition was defined as acoustically fully reflective. Since the area of the inlet boundary was small compared to the plenum wall area, it was assumed that the

reflective boundary condition would cause small errors. Partially non-reflecting boundary conditions [102] were assigned to the pressure field at the outlet of the system to simulate an infinitely long outlet by eliminating acoustic reflections. A flame surface density (FSD) model [149] was utilized to model the turbulence/combustion interaction. In order to reduce the complexity of the simulation, the simulation was initially carried out without the mixing process and the walls were assumed to be adiabatic. However, the influence of wall temperature and mixing was considered later. The mixture of methane and air was fed in via the inlet (see Fig. 6.1) at a temperature of 500 K. The mixture mass flow was adjusted such that an average axial velocity of 120 m/s is achieved at the end of premixing duct in order to mimic the aerodynamic effect of the burners in technical combustion chambers.

## 6.4 Results

### 6.4.1 Influence of Equivalence Ratio on the Instabilities

The global equivalence ratio is reported in the literature [18, 45] as an important controlling factor for thermoacoustic instabilities. In the adiabatic combustor, simulations with equivalence ratios  $\theta = 0.6, 0.7, 0.8, 0.9$  were performed in order to achieve oscillations with high amplitudes. The simulations were performed for at least 500 ms to reach the limit cycle. A frequency analysis of the last 200 ms of the pressure signal recorded at point Pw (see Fig. 6.1) was performed and the corresponding Fourier spectrum is shown in Fig. 6.2.

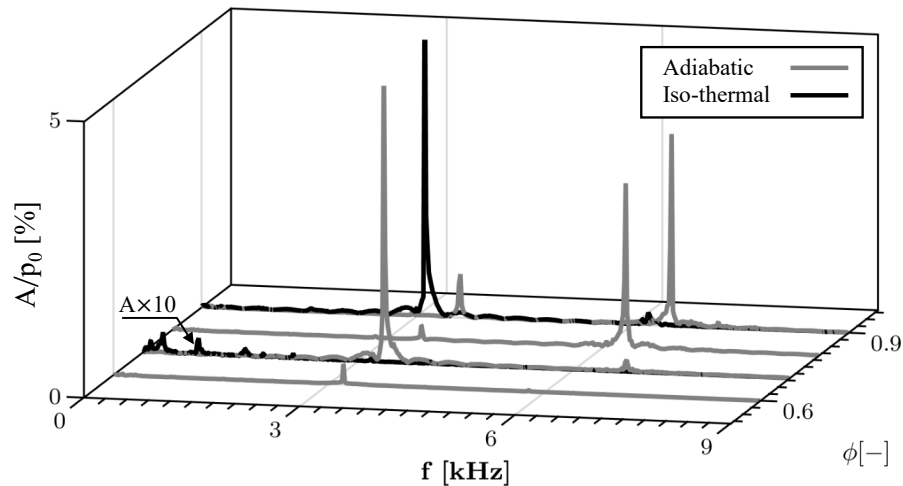


**Fig. 6.2** Spectra of pressure signal captured at Pw (see Fig. 6.1); the amplitude  $A$  are normalized with the mean chamber pressure  $p_0$ .

The logarithmic representation of the distributions of the acoustic pressure amplitude  $A$  at the preferred frequency for the studied equivalence ratios is pictured in Fig. 6.3. In order to obtain the amplitude information, the FFT was applied to the time signal

of the pressure over at least 20 cycles at each cell. The phase information can easily be deduced from the plots by the position of the node lines. For the lowest equivalence ratio  $\theta = 0.6$  the system showed the smallest amplitude. It can be observed that the simulation with an equivalence ratio of  $\theta = 0.7$  led to high-frequency oscillations with a normalized amplitude of 5% at a frequency of 3.3 kHz corresponding to the first radial Eigenmode (see Fig. 6.3). By increasing the equivalence ratio to  $\theta = 0.8$ , oscillations with largest amplitudes occurred at the second radial natural frequency with a frequency of 6.3 kHz. For the simulation with  $\theta = 0.9$ , the system shows unstable operation in both the first and second radial modes. For further investigations, we have chosen the case with  $\theta = 0.7$  (termed as reference case), since for this case a) the instabilities were observed in the first radial mode, which simplifies the numerical and experimental investigations of the flame/acoustic interaction and b) the largest amplitude was observed.

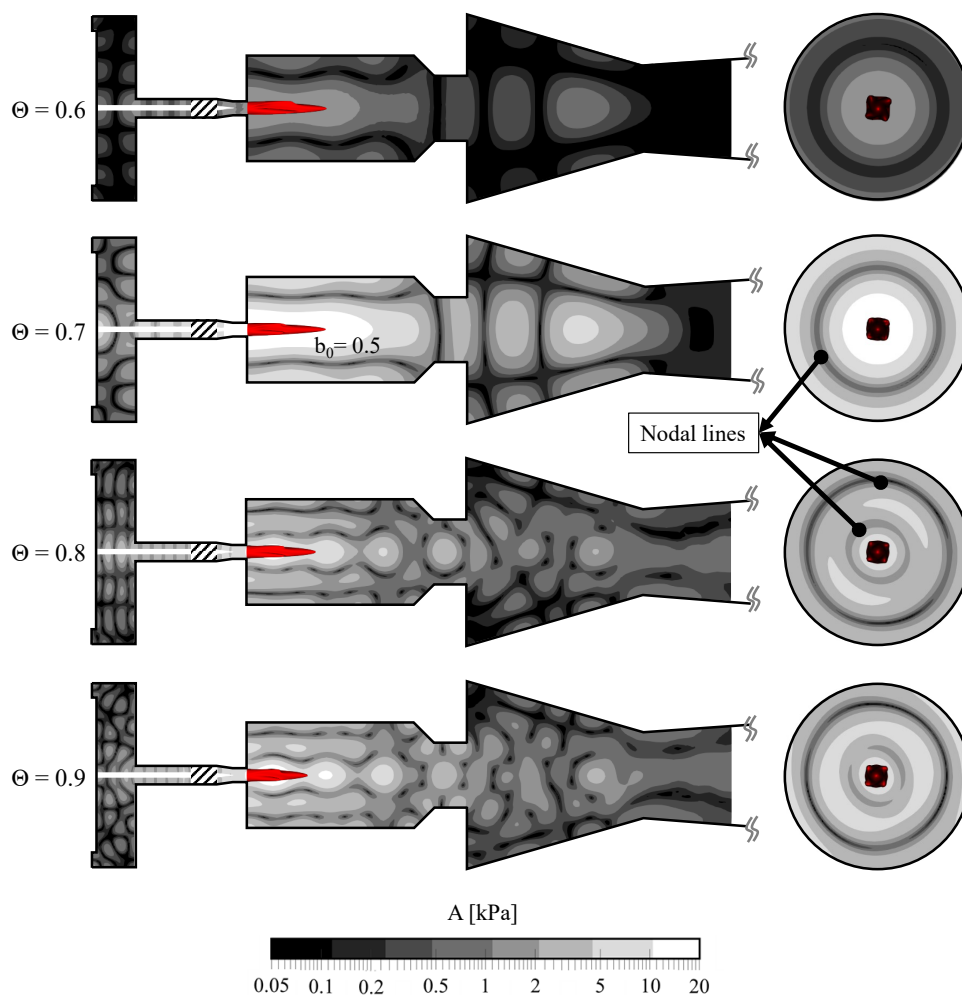


**Fig. 6.3** Amplitude distribution of the acoustic pressure for the peaks with largest amplitudes (see Fig. 6.2).

Figure 6.4a shows the normalized line of sight integration  $dQ$  of the phase-averaged heat release rate field during an oscillation period for the reference case. For the nor-

malization, the maximum value of  $dQ$  at phase  $270^\circ$  is used. The results indicate a clear oscillation of the intensity of the local heat release rate and a periodic flame convection due to the interaction between the flame and the periodically separated vortices moved downstream. The normalized fluctuation of the phase-averaged global heat release rate  $\dot{Q}_1$  and the volume-averaged unsteady pressure  $p_1$  for a period of oscillation are plotted in Fig. 6.4b. For the spatial averaging of the unsteady pressure, a volume around the flame is considered in which the pressure oscillates in phase. In addition, this figure shows the total heat release rate of the contribution from density oscillation  $\dot{Q}_{\rho_1}$ , which is defined by the following equation [35]:

$$\dot{Q}_{\rho} := \int \frac{\rho_1}{\rho_0} \dot{q}_0 dV \quad (6.2)$$

It can be noticed that the heat release rate oscillates almost in phase with the pressure, indicating a positive thermoacoustic coupling. It can be also seen that the amplitude of the contribution of the density oscillation is in the same order as the amplitude of the oscillation of the heat release rate, which is an indication that the density mechanism is the main driving mechanism.

#### 6.4.2 Influence of Chamber Wall Temperature on Instabilities

In order to be able to investigate the configuration experimentally, the temperature of the combustion chamber walls had to be reduced to a realizable temperature. The influence of wall heat transfer on the occurrence of thermoacoustic instabilities of the reference case is investigated by setting the temperature of the chamber walls to  $T_w = 1700, 1400, 1100$  K, whereby the temperature of 1100 K represents a realistic wall temperature that can be achieved in the experiment without TBC. The area-averaged pressure amplitude for the investigated wall temperatures is shown over the area-averaged combustor temperature in Fig. 6.5. It is found that the reduction of the wall temperature reduces the area-averaged pressure amplitude and could even stabilize the system at the lowest wall temperature of  $T_w = 1100$ .

An evaluation of the acoustic mode shapes of the simulations with  $T_w = 1700$  and 1400 K (see Fig. 6.6b) reveals that the pressure amplitude has the same general mode shape (R1) as in the configuration with adiabatic walls with homogeneous sound speed field. However, their spatial distribution changes as the wall temperatures decrease. The mode shape shrank in the axial direction and the acoustic pressure amplitude with large values was shifted towards the base-plate. As a result, the end part of the reacting zone is not subjected to the large pressure amplitude of the pressure oscillation, which reduces the thermoacoustic coupling capability of the system. This might be a reason for the reduction of the volume-averaged pressure amplitude. At the minimum wall temperature of  $T_w = 1100$  the system is fully stabilized and at the selected Eigenfrequency no

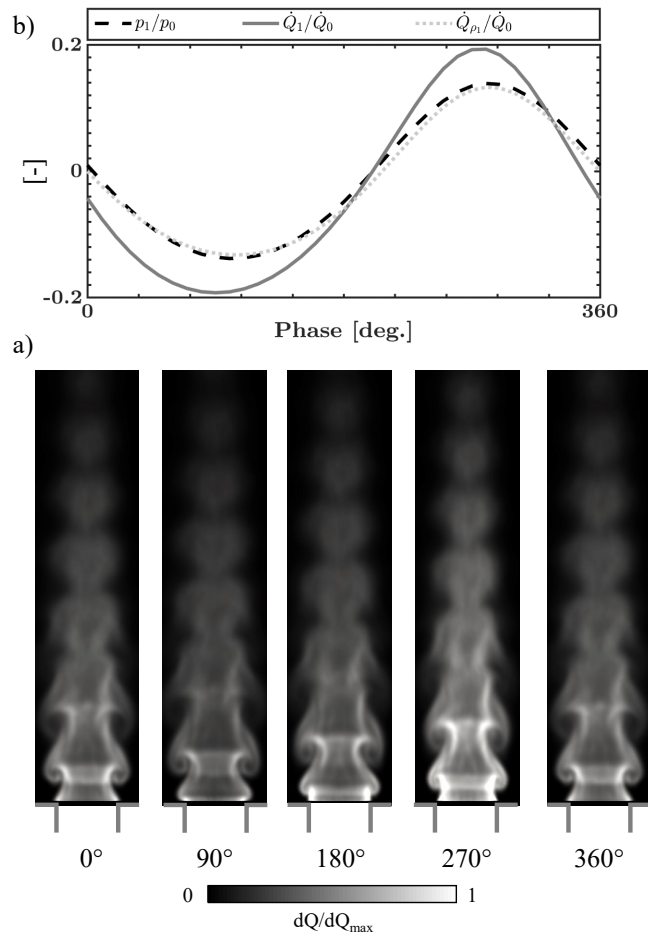


**Fig. 6.4** a) Phase-averaged line of sight fields of heat release, b) Phase-averaged global heat release rate  $\dot{Q}_1$ , the contribution of density oscillation  $\dot{Q}_{\rho_1}$ , and volume averaged unsteady pressure  $p_1$ .

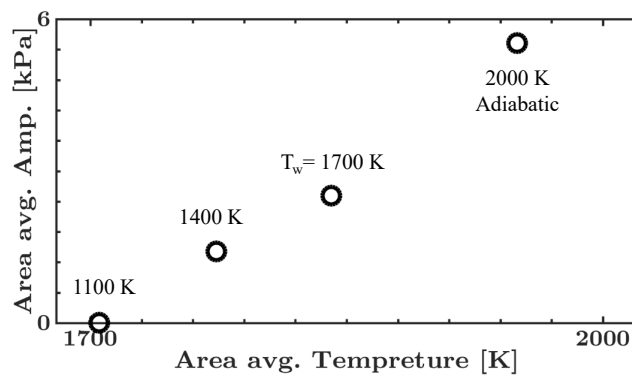


**Fig. 6.5** Area-averaged pressure amplitude over the area-averaged combustion chamber temperature.

comparable acoustic pressure amplitude attained. Since no higher chamber wall temperatures than 1100 K are feasible in the experiment, a hypothesis was made based on the observation that an increase in the equivalence ratio reduces the flame length and thus brings the flame back to the pressure nodes with large amplitudes. Further in-

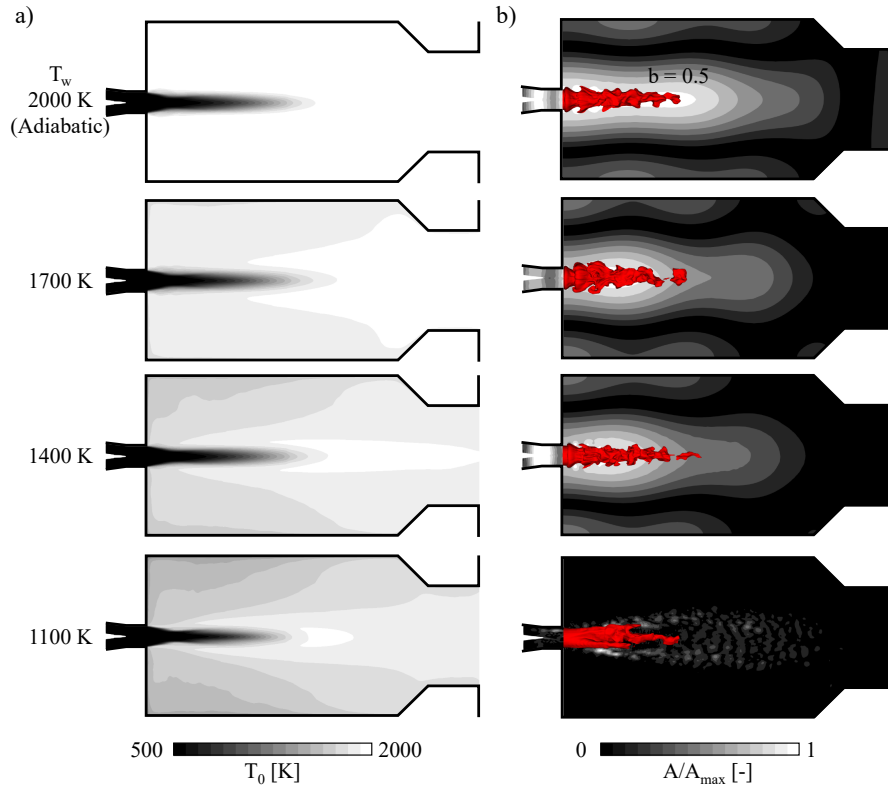


**Fig. 6.6** a) Fields of the time-averaged temperature and b) the amplitude of the acoustic pressure, normalized with the maximum amplitude in the combustor at each simulation.

investigations confirmed that it was possible to recover the oscillation by increasing the equivalence ratio from 0.7 to 0.9 in the system with  $T_w = 1100$  K. The pressure spectra for the configuration with isothermal walls with the equivalence ratio 0.7 and 0.9 are shown in Fig. 6.2 and compared with the corresponding results from the adiabatic configuration. While the use of isothermal walls with  $T_w = 1100$  K led to a stabilization of the oscillations with  $\theta = 0.7$ , with  $\theta = 0.9$  the oscillations with higher amplitudes arose at the first Eigenfrequency. It is to be mentioned that in this case ( $\theta = 0.9$ ,  $T_w = 1100$  K) the amplitude at the second Eigenfrequency was greatly diminished.

## 6.5 A strategy to Dampen Thermoacoustic Instabilities

The acoustic transverse oscillations are attenuated when it propagates at a frequency lower than a cut-off frequency  $f_{R1}^c$ . In a cylinder, the cut-off frequency depends on the speed of sound  $c$  (which in turn is a function of temperature) and the cylinder diameter  $D_c$ , ( $f_{R1}^c \propto c/D_c$ ) [64]. The cooling of the combustion chamber walls led to an inhomogeneous temperature field with lowest area-averaged temperature in the vicinity of the combustion chamber base plate, the average temperature increases in axial direction, as shown in Fig. 6.6a. This temperature distribution induced an increase in the cut-off frequency along the axis. The transverse oscillations that were resonant up-

stream of the chamber were attenuated in the downstream location and could no longer survive. Thus, changes in the cut-off frequency might be a strong lever to dampen thermoacoustic instabilities. To make use of this physical effect, the cylindrical combustion chamber of the unstable adiabatic reference case ( $\theta = 0.7$ ) was modified to increase the cut-off frequency along the axis by 60% by making it conical. The downstream and upstream features remained unchanged. The conical chamber geometry (top) can be deduced from the axial velocity field shown in Fig. 6.7b and compared with the cylindrical chamber geometry (bottom). The time evolution of pressure fluctuations is shown in Fig. 6.7a and reveals that the geometrical modification prevented the system from becoming thermoacoustically unstable.

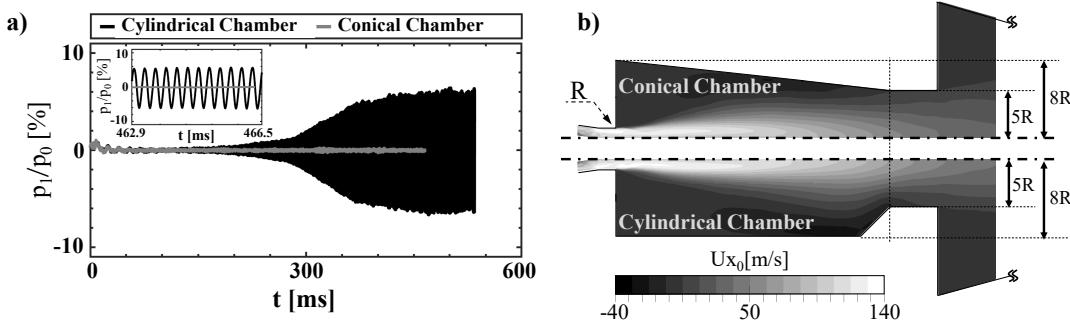


**Fig. 6.7** a) Pressure history captured at  $P_w$ , b) Time-averaged axial velocity;  $R$  is the radius of the duct.

**Influence of Technical Mixing on the Instabilities** The phase difference of the oscillations of the equivalence ratio with pressure oscillations in a technically premixed system might cause this interaction to be stabilizing, which is to be assessed. The impact of injecting fuel and performing a technically premixed simulation was investigated by simulating the reference case including the mixing process. The injector holes are discretized with 0.2 mm cells, corresponding to 5 cells over the injector hole diameter. The operating conditions of in this study are summarized in Table 6.1. The results revealed

**Table 6.1** Overview of the operating conditions.

| $\dot{m}_{air}, \text{g s}^{-1}$ | $\dot{m}_{fuel}, \text{g s}^{-1}$ | $T_{in}, \text{K}$ | $\phi, -$ |
|----------------------------------|-----------------------------------|--------------------|-----------|
| 101.5                            | 4.13                              | 500                | 0.7       |

that when the mixing was considered, the system exhibited self-excited instabilities with higher amplitudes compared to the premixed reference configuration as shown in Fig. 6.8a. The time-averaged equivalence ratio and its phase-averaged fluctuation are shown in Fig. 6.8b. Although the global equivalence ratio is set to 0.7, the flame root in particular is subjected to a slightly increased time-averaged local equivalence ratio due to the non-ideal pre-mixing, leading to an increase in the energy density of the flame, which

is directly related to the tendency of the flame to become unstable. The fluctuation field of the equivalence ratio is characterized by the pockets of rich and lean mixture formed by the interaction of the acoustic pressure waves at the injecting position with the fuel mass flow. These variations at the flame zone lead to at least two mechanisms by which the heat release rate could oscillate, a) directly by oscillation the heat of reaction and b) indirectly by oscillation of the laminar flame speed. To evaluate these mechanisms, the total heat release rate of the contribution from mixture fraction oscillation  $\dot{Q}_{ft_1}$  and laminar flame speed oscillation  $\dot{Q}_{sl_1}$  were defined analog to Eq. 6.2 and are plotted in Fig. 6.8c. It can be seen that although the amplitudes of these oscillations are small, they are in phase with the pressure oscillations, which indicates the destabilizing effect of the mixing in this configuration.

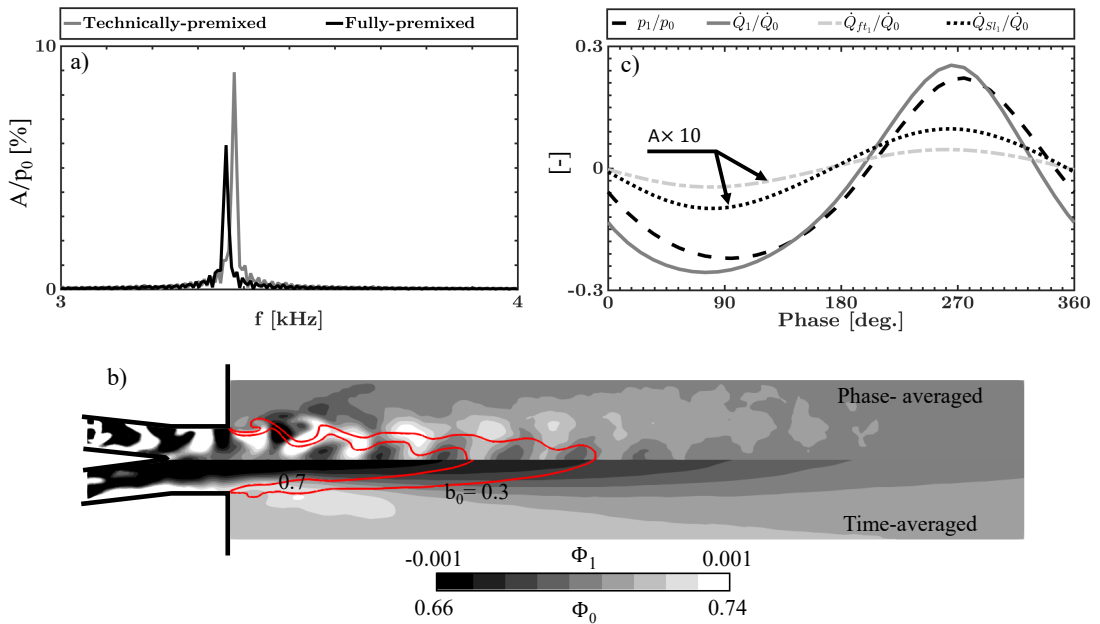


**Fig. 6.8** a) Spectra of the pressure signal captured at Pw, b) Time-averaged equivalence ratio and its phase-averaged fluctuation and c) Phase-averaged global heat release rate, the contribution of oscillation of mixture fraction  $\dot{Q}_{ft_1}$ , laminar flame speed  $\dot{Q}_{sl_1}$  and volume averaged unsteady pressure  $p_1$ .

## 6.6 Influence of Upstream Acoustic Boundary Conditions on Instabilities

A pressure anti-node was to be expected at the inlet of the computational domain of the reference case (see Fig. 6.3) since the inlet boundary condition was defined as acoustically hard, which is not feasible in the experiment. An additional cylindrical plenum (upstream outer plenum) was placed around the existing plenum (upstream inner plenum) to achieve a more realistic acoustic condition at the connection between upstream inner and outer plenum. In order to approach the behavior of the acoustically closed inlet in the reference configuration, a new upstream inner plenum was proposed.

In the new plenum, the annular gap was replaced by four holes around the circumference to reduce the opening section and correspondingly the acoustic fluxes from the upstream inner plenum. The sketches of the three different upstream plenums examined in this study are shown in Fig. 6.9. The results of the simulations in term of unsteady pressure evolution and phase plane of the oscillations are compared in Fig. 6.10. The result revealed that the system with Acoustically Open Inner Plenum (AOIP) could not develop into HFI with high amplitude. The system with Acoustically Almost Closed Inner Plenum (AACIP) exhibited HFI with an amplitude and frequency comparable to the reference case with Acoustically Closed Inner Plenum (ACIP), evidencing that the induced acoustic flux from the upstream inner plenum to the outer plenum directly influences the thermoacoustic behavior of the system. It is worth mentioning that with AOIP the pressure oscillates at lower frequencies with a larger amplitudes than at higher frequencies (see Fig. 6.10d).

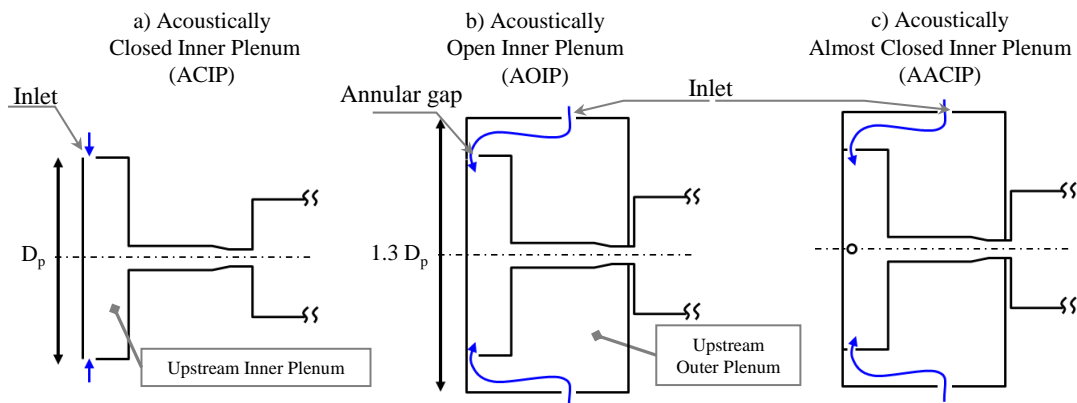


**Fig. 6.9** Schematic of studied upstream plenums.

## 6.7 The Final Configuration

The final geometry was proposed based on lessons learned and considering the rig geometry. For this geometry the diameter of the holes in the inner upstream plenum were modified so that they do not exceed the allowable pressure loss requirements of the test rig. Figure 6.11a shows the time-averaged and instantaneous velocity field which serves to illustrate the air distribution in the final configuration. The air mass flow entering the system is divided into the combustion air and the air for cooling the chamber. In the simulation, the chamber walls are set to 1100 K. The simulations were carried out with a global equivalence ratio of 0.9 taking into account the mixing process. An overview of the boundary conditions for this simulation is given in Table 6.2. The simulation resulted in a comparable mode shape and amplitude of the acoustic mode, which is shown in Fig. 6.11b. The configuration is currently being investigated

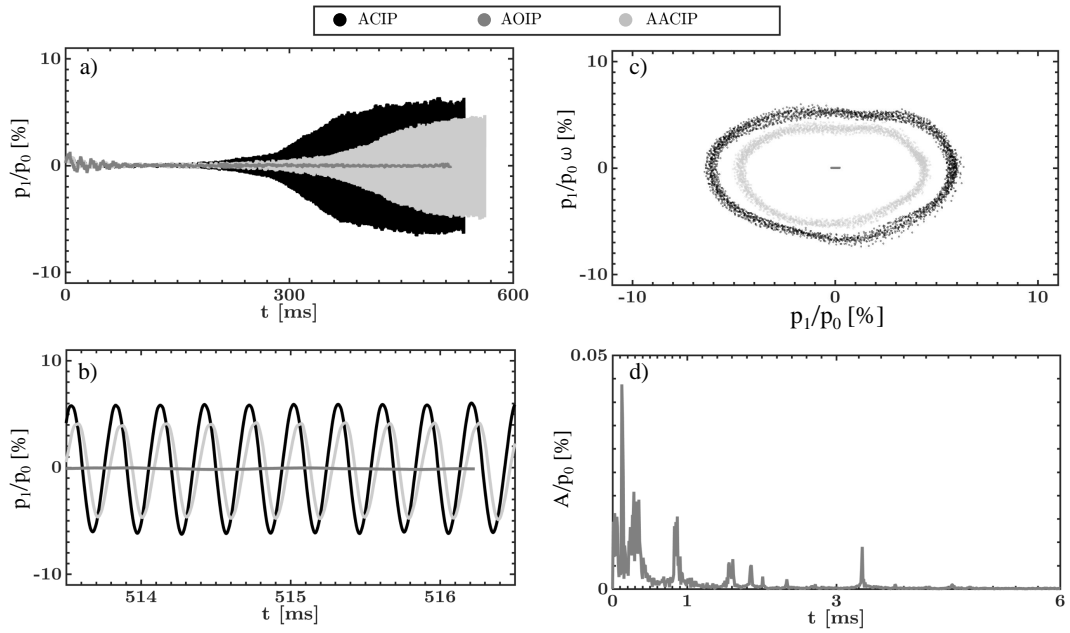


**Fig. 6.10** a) and b) pressure history, c) Phase plane of the established oscillations; ( $\dot{\phantom{p}}$ ) and  $\omega$  denote derivative with respect to time and limit cycle angular frequency d) Spectra of the pressure signal.

experimentally.

**Table 6.2** Overview of the operating conditions.

| $\dot{m}_{air}, \text{g s}^{-1}$ | $\dot{m}_{fuel}, \text{g s}^{-1}$ | $T_{in}, \text{K}$ | $\phi, -$ | $T_w, \text{K}$ |
|----------------------------------|-----------------------------------|--------------------|-----------|-----------------|
| 562                              | 5.25                              | 500                | 0.9       | 1100            |

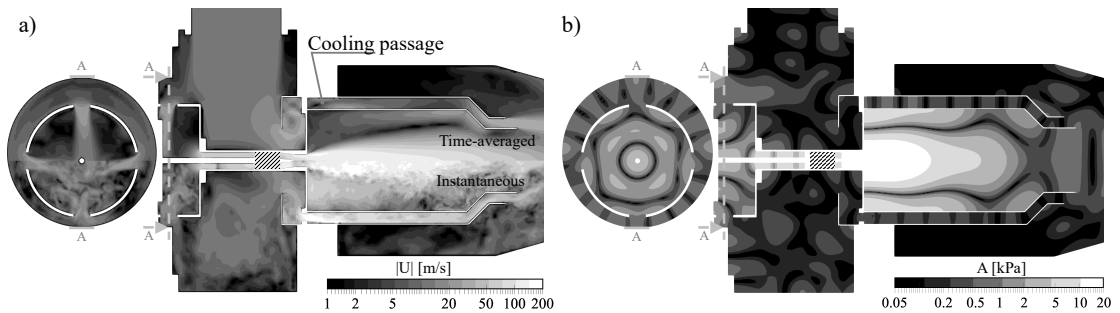


**Fig. 6.11** a) Fields of velocity and b) Amplitude distribution of the acoustic pressure at limit cycle.

## 6.8 Conclusion

In this work LES were used to support the design and investigation of HFI in a cylindrical atmospheric single jet combustion chamber. The impact of different parameters such as equivalence ratio, wall temperature, technical mixing, and acoustic transmittance of upstream boundary conditions were addressed. It was found that it is possible

to achieve high amplitude instabilities in the system by increasing the equivalence ratio. The consideration of the technical mixing proved to be destabilizing. It was also found that the reduction of the wall temperature had a stabilizing effect on the instabilities, which could be compensated by increasing the equivalence ratio. The impact of temperature on the cut-off frequency has inspired us to modify the geometry of the combustion chamber. It was found that it would be conceivable to make a very unstable adiabatic cylindrical combustion chamber stable by making it conical. The treatment of the upstream boundary conditions had a decisive influence on the instabilities. When the boundary condition was changed to acoustically open, the instabilities were diminished. The instabilities could be recovered by using a new plenum geometry, which was acoustically almost closed. A configuration susceptible to high-frequency instabilities was developed which meets the experimental requirements and is currently being investigated. The initial experiment yielded very promising results regarding the occurrence of the first radial mode at the desired frequency.

## 6.9 Acknowledgments

The authors gratefully acknowledge the financial support of the state of North Rhine-Westphalia and the German Ministry of Economics and Technology for the collaborative project *Untersuchung der Entstehungsmechanismen zu Hochfrequenzinstabilitäten* of the Clean Energy Center stage 2 (project funding reference number 03ET7011L), as well as the computing time granted by the Center for Computational Sciences and Simulation of the University of Duisburg-Essen and provided on the supercomputer *magnitUDE* (Deutsche Forschungsgemeinschaft grant INST 20876/209-1 FUGG) at the Zentrum fuer Informations- und Mediendienste.

## CHAPTER 7

### **Design and Testing of a High Frequency Thermoacoustic Combustion Experiment**

*This chapter including all figures and tables was previously published in AIAA journal, V. Sharifi, C. Beck, B. Janus, and A. M. Kempf, Design and Testing of a high-frequency Thermoacoustic Combustion Experiment [165]. The author V. Sharifi ran all simulations, wrote the paper and generated all figures and tables. The authors C. Beck, B. Janus and A. M. Kempf contributed corrections, discussions and proofreading.*

This paper presents a novel experiment in an atmospheric cylindrical single-jet combustor, designed to exhibit high-frequency radial thermoacoustic instabilities. The experimental configuration was designed based on an *a priori* set of comprehensive numerical investigations, the experiments were conducted with pressure and temperature probes, and large-eddy simulations of the final experiments were performed. The results from simulation and experiment were compared and showed a reasonable agreement in the amplitude, frequency and mode shape of the self-excited instability in the unstable operating point, and no thermoacoustic oscillations in the stable operating point. Various parameters have been varied to assess their effect on thermoacoustics - including variations of mass flow rate, of equivalence ratio and combustor wall temperatures. For the unstable cases, direct effect of pressure on density was found to drive the thermoacoustic oscillations.

#### 7.1 Introduction

Avoiding thermoacoustic high-frequency Instabilities (HFI) is a challenging issue in gas turbine design. They constrain the operation range and efficiency of gas turbines and indirectly increase their emissions [8]. High-frequency oscillations, known as screeching, have also been problematic in numerous jet engines and rocket systems [20, 166, 167, 168, 169, 170]. In rocket engines, HFI is best known from the development of the F-1 engine for the Saturn V rocket in the 1950s and 1960s [171]. More than 2,000 full-scale engine tests were performed to investigate and mitigate HFI and design a stable combustion system. From these tests, it was determined that the insta-

bilities were due to the interaction of the transverse oscillation with the fuel injection. It was found that these instabilities can be successfully suppressed by a combination of a suitable injector design and a baffle system [171, 169].

The main problem in developing a combustor that is robust to HFI is the limited knowledge of the underlying driving mechanisms for this type of instabilities. The lack of relevant and well-documented experimental test data is the primary hurdle to a better understanding of the HFI mechanism in gas turbine combustors. Self-excited thermoacoustic test data can be provided either from a) full or large scale test rigs or b) laboratory-scale combustors. The available experimental data of the large-scale test rigs is hardly suitable for getting insight into the thermoacoustic mechanisms. Because 1) the test rig must be switched off immediately after the occurrence of detectable high-frequency vibrations, the preset operating conditions cannot be regarded as stationary or associated with the instabilities, and 2) the available test data from the large-scale tests are limited to a pressure signal at one or two positions as, normally, optical access is not available. In addition, the effort to use numerical simulations to get more insight into the combustion of the large test cases is too big, due to uncertainties associated with the boundary conditions. It should be noted that, the system is normally very sensitive — a small percentage increase in the equivalence ratio can determine whether the system is thermoacoustically stable or unstable [18, 44].

Lab-scale tests could provide a more useful understanding of thermoacoustic instabilities. Sjunesson et al. [18] introduced a rectangular combustion system with bluff body flame stabilization, known as the Volvo test case. The walls of the combustion chamber were cooled, although the wall temperatures were not addressed in the study. The acoustic properties of the upstream and downstream boundary conditions were also not reported. The system operated in a thermoacoustically stable regime for an operating condition with an air velocity of 17.3 m/s and an equivalence ratio of 0.61. High-frequency oscillations, at 1400 Hz, were observed when the velocity and equivalent ratio were increased to 36 m/s and 0.72, respectively. The mode shape of the instabilities was not reported, but Schlieren images showed a clear interaction of the flame with periodically shed vortices. Ghani et al. [57] simulated a simplified version of the Volvo test case. They used a compressible third order CFD code with a two-step mechanism for combustion modelling. The heat transfer from the combustor walls was neglected and the inlet and outlet boundaries were assumed to be fully reflective. They could capture the high-frequency oscillations (1360 Hz corresponding to the first longitudinal and second transverse modes) and the periodic vortex shedding. They concluded that the observed flame-vortex shedding was due to the longitudinal part of the oscillations. The investigation by Jourdin et al. [61] showed that the observed flame-vortex interaction in the experiment could be due to the interaction by the pure longitudinal mode with an oscillation frequency of 1.4 kHz, which emphasizes ambiguous numerical results

due to the lack of information from the experiment. Further difficulties in simulating of the Volvo test case are discussed by other authors [161, 162, 172] Due to the flame stabilization technique applied in the Volvo case, the data is probably not applicable to a premixed jet flame as examined in the present paper.

Rogers et al. [20] investigated a V-flame in a rectangular combustor, which showed high-frequency oscillations of 3800 Hz. They observed alternate vortex shedding from the lips of the flame holder with the same frequency of the instability. The transport of fresh combustible mixture to the flame through the vortices is addressed as a coupling mechanism. High-frequency instabilities in jet engine afterburners are described by Blackshear et al. [170]. They reproduced the HFI in a generic test rig. Adiabatic compression and flame-vortex interaction are discussed as the driving mechanisms of the observed instabilities. Urbano et al. [136, 173] numerically investigated the high-frequency instability of a model liquid rocket engine with multiple injectors. They found that the response of the flames located in the pressure anti-nodes is strongest, while the flames located at a pressure node feed almost no acoustic energy into the system. They suggested that for the flame located at the pressure node, the resulting pressure changes at the jet outlets lead to fluctuating jet velocities, which in turn leads to oscillations of the heat release rate.

The self-excited cylindrical combustor of the Sattelmayer group [44, 21] considered a premixed swirl-stabilized flame under atmospheric conditions. They investigated the impact of the swirl number, the preheating temperatures and the mass flow rates on the susceptibility of the burners to HFI. They observed transverse instabilities with frequencies between 2.4 and 3.4 kHz for the studied swirl numbers, preheat temperatures and mass flow rates by increasing the equivalence ratio of the mixture. They found that the system became unstable even in a fuel-lean mixture by increasing the swirl number and the mass flow rate. However, increasing the preheating temperature resulted in a more robust system. Further investigations showed that the displacement and deformations mechanism [46, 47] could be the driving mechanisms for the instabilities observed in the experiment. Where the lab-scale experiment of the Sattelmayer Group is well defined, the type of flame stabilization (e.g. swirl-stabilized, bluff-body-stabilized, jet-stabilized) might have a decisive influence on the mechanisms that cause the instabilities [70]. Thus, to investigate the flame dynamics of a jet-stabilized flame (as used in Siemens gas turbines), it is probably not possible to consider an unstable jet burner with a swirl-stabilized flame experiment.

Buschhagen et al. [53] designed a cylindrical single-jet combustor with a premixed flame. To achieve acoustically well defined boundary conditions, they used a choked orifice plate upstream and a choked nozzle downstream of the test combustor. The system exhibited HFI in the frequency range between 4.8 and 6.5 kHz, the mode shape of which was not determined experimentally. In this experiment, no operating condition

with stable combustion was reported and further investigations could not show a clear trend for instabilities with varying parameters. Thus, the question might arise as to whether or not the observed instabilities were caused only due to acoustically blocked inflow and outflow: The acoustically closed boundaries reduced the acoustic energy flux from the combustor, which could lead to an accumulation of acoustic energy in the system. In other words, the observed thermoacoustic instabilities might have occurred independently of the coupling capability of the flame and only by minimizing the acoustic energy fluxes or losses, which is not typical for gas turbines.

Considering the limitations of the existing experiments, the main challenge for the work presented here was to develop a suitable lab-scale experiment that resembles the state-of-the-art Siemens combustors and is able to exhibit thermoacoustic high-frequency instabilities. To design the experiment, a large number of large eddy simulations were performed until a suitable configuration was found. In the course, the simulation tools were improved to enable a realistic prediction of high-frequency acoustics. This paper aims to study the experiment results and the prediction capabilities of the numerical methods for high-frequency flame dynamics. The decisive role of the combustor wall temperature is highlighted and the contribution of possible mechanisms causing thermoacoustic coupling is addressed.

## 7.2 Experiment

### 7.2.1 Design - based on *a priori* LES

The configuration examined and discussed in this paper was developed based on comprehensive numerical studies. The design procedure, supporting simulations and their results were published in our previous works [35, 159]. This section briefly summarizes the main considerations and findings of these studies. Forced-response analyses [35] were performed to investigate the excitation mechanisms of HFI in a jet flame. The order of importance of several mechanisms that have contributed to the instabilities of the flame has been identified. It was revealed that the flame can excite HFI most strongly when located in an acoustic pressure anti-node (and simultaneously an acoustic velocity node). This finding was used in the design of a thermoacoustically unstable combustor. For a self-excited configuration, the reproduction of such a flame acoustic interaction was achievable by placing a flame on the center-line of a cylindrical combustion chamber, when the flame was excited in the radial mode of the chamber. The radius of the chamber was chosen such that frequencies of practical interest, which are often observed in gas turbines during thermoacoustic instabilities, could occur. The forced-response study [35] had also indicated that extremely long flames at pressure anti-nodes were less susceptible to thermoacoustic instabilities. In order to avoid extremely long flames and to achieve fluid dynamic similarity with the technical combustor

tor, a physical turbulence generator, inspired by the technical system, was used. Large upstream and downstream plenums were used to be able to place the terminating boundaries of the system far away from the flame to minimize their potential interaction with high-frequency oscillations and minimize the resulting errors. In this way, a generic, adiabatic and premixed configuration was developed. LES of the generic configuration at atmospheric pressure with different equivalence ratios of a mixture of methane and air was performed. It was observed that the system was able to exhibit radial thermoacoustic instabilities at the desired frequency of 3 kHz for an equivalence ratio of 0.7. In the next step, the generic configuration was modified to obtain an experimentally feasible configuration. Studies were carried out on the effects of upstream boundary, wall cooling and the impact of the realistic mixing of fuel with air on the susceptibility of the system to HFI. The system was found to be more susceptible to HFI with a plenum allowing reduction of acoustic losses. We also observed that the configuration with the (numerically) acoustically open upstream boundary condition was not susceptible to instabilities. Further investigations on the cause of such behavior are necessary. However, at this point, we believe that the main reason for this behavior is as follows: For the first radial mode in our system with the centric burner, the center-line of the combustion chamber is exposed to a pressure anti-node. The acoustic pulsations (generated in the combustor) travel upstream through the mixing tube. A boundary condition with higher reflection coefficient reduces the acoustic energy flux from the boundary, which means more acoustic energy is preserved in the system, making the system more susceptible to thermoacoustic instabilities. The analytical investigation of Li et al. [174] for the longitudinal acoustic waves (as is the case in our mixing tube) showed that the predicted amplitude of instabilities decreases significantly when the acoustic losses at the boundaries are increased, which is in line with our observation. An improved upstream plenum was designed to provide an almost closed boundary condition while being experimentally realisable. The downstream acoustic boundary had almost no effect on the HFI. This could be a consequence of acoustic mode cutoff caused by increasing temperature in longitudinal direction, thus decoupling modes from downstream boundary conditions, as investigated by Schulze et al. [68]. The impact of wall cooling turned out to be stabilizing in nature. The decrease in wall temperature led to an axial redistribution of the amplitude of the first radial mode. For the adiabatic configuration (see Fig. 7.1), the entire flame was positioned directly on the high amplitude of the pressure-anti-node of the acoustic mode. With decreasing wall temperature the mode shape shrinks in the axial direction and the area of the high acoustic pressure amplitude shifted towards the base plate of the combustor. Thus, the end part of the reaction zone was not exposed to the high pressure amplitude of the pressure oscillation, which might adversely affect the thermoacoustic coupling capability of the system. To make a general statement, this effect has to be investigated further.

For wall temperatures below a critical value, complete damping of the instabilities occurred. It was found that the critical wall temperature was a function of the equivalence ratio. Increasing the equivalence ratio of the mixture (from 0.7 to 0.9) resulted in a reduction of the critical temperature (from 1100 K to 850 K). Considering the realistic mixing of the fuel with air had a supporting effect on the instabilities and led to higher HFI amplitudes, although the mode shape and frequency were not changed noticeably. The final configuration was designed on the basis of all insights and an operating point was identified at which the system exhibited HFI with a considerable amplitude. This configuration is presented in the next section.

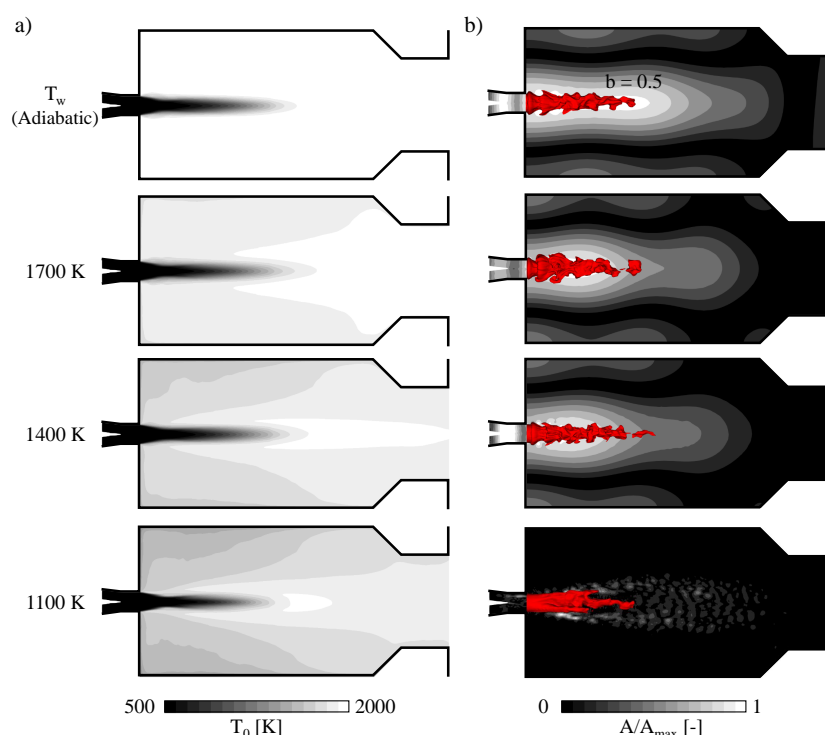
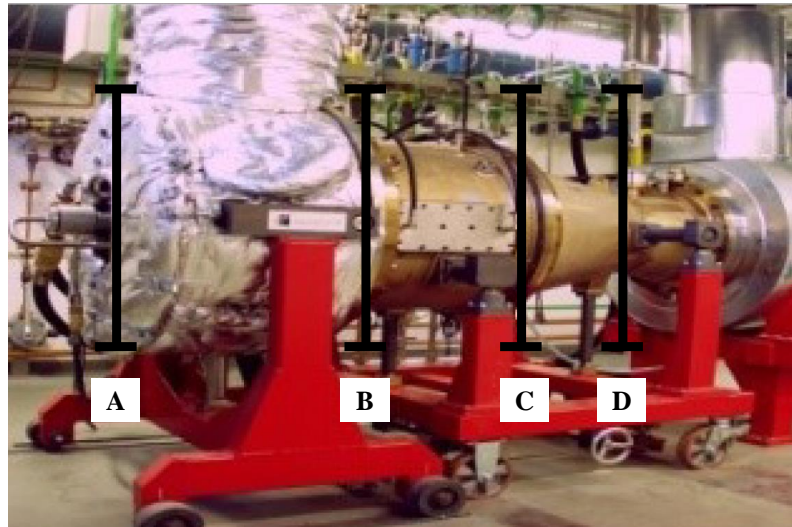


**Fig. 7.1** Fields of a) the time-averaged temperature and b) the amplitude of the acoustic pressure, normalized with the maximum amplitude in the combustor at each simulation [159].

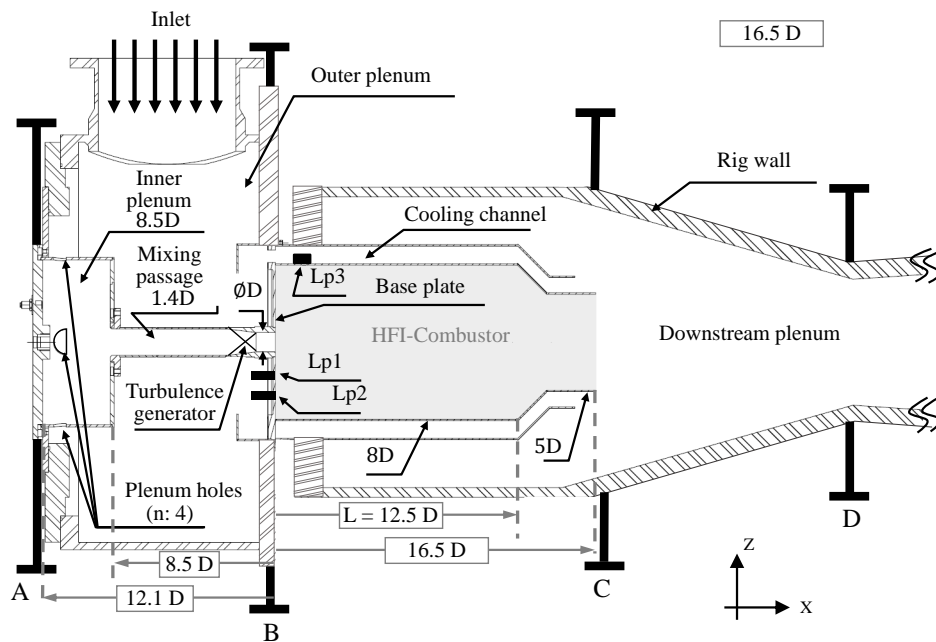
### 7.2.2 Experimental setup and diagnostics

The single-jet metallic HFI combustor of Siemens and the University Duisburg-Essen, SiMetUDE, was designed to generate self-excited radial high-frequency thermoacoustic instabilities. It was tested experimentally in the atmospheric combustion laboratory of Siemens AG in Mülheim. The first experiment served to examine whether the instabilities predicted by numerical simulation would occur in practice. Therefore, an effort was made to make the experiment as simple and inexpensive as possible. This experiment should then serve as a starting point for further, more sophisticated experiments with optical access in the future. The experimental test facility and the schematic

of the combustor are illustrated in Fig. 7.2.



(a) Image of the experimental facility.



(b) Schematic of the combustor, showing the locations of the pressure sensors Lp1, Lp2 and Lp3;  $D = 0.04$  m.

**Fig. 7.2** Single-jet Metallic HFI combustor.

The combustor consists of an outer and an inner upstream plenums, a mixing passage, a turbulence generator, a cylindrical flame tube (HFI-Combustor), a downstream plenum and an exhaust channel. The exhaust gases were released into the environment through a chimney. The outlet boundary of the computational domain was located at a distance of  $60D$  downstream of the chamber, where  $D$  is the diameter of the mixing passage on the base plate of the HFI-combustor (see Fig. 7.2b) and is equal to  $0.04$  m. The mixing passage and turbulence generator were not designed specifically for this study, but were chosen to imitate the aerodynamic effect of the burners in tech-

nical combustion chambers. The outer plenum was thermally insulated as shown in Fig. 7.2a and the inner surface of the rig wall was coated with refractory concrete. Hence, they can be assumed to be adiabatic. The metallic HFI-Combustor consisted of a cylindrical part and a base plate. The base plate was provided with a 1 mm thermal barrier coating. A cooling channel was placed concentrically around the flame tube. The amount of cooling air could be controlled by the number of open cooling holes located between the plenum and the chamber. For the results presented in this paper, all cooling holes were closed, but one cable passage for instrumentation remained open. The air supplied to the rig plenum was divided into combustion air, cooling air and leakage. The combustion air was led into the cylindrical combustor through four holes (of semi-circular cross-section) at the circumference of the inner plenum. The inner plenum was designed to reduce the acoustic energy fluxes (losses) out of the cylindrical combustor. The fuel (natural gas) was injected and mixed with the combustion air through several nozzles at the turbulence generator. The turbulence generator was characterized by a high shear rate and no swirl, so that a jet stabilized flame is resulting that is relevant to large-scale Siemens combustion systems. The total air mass flow rate was measured using a standard nozzle. The air was preheated to a temperature of 500 K. To measure pressure fluctuations, the HFI-Combustor was equipped with 3 piezoelectric high-frequency pressure transducers, Megitt type CP 235, as shown in Fig. 7.2b. The pressure transducer in the HFI-Combustor was positioned such that the pressure field of the first radial mode could be addressed from the measurements. Thus, Lp1 and Lp2 were placed on the base plate at a radial distance of 50 mm and 100 mm from the center-line of the combustor, while Lp3 was mounted on the cylindrical wall at an axial distance of 100 mm from the base plate. The transducers were installed in a hollow adaptor and were cooled with purged air. With the current arrangement of the transducers, the longitudinal mode of the combustor could not be measured. To measure the static temperature, the combustor wall was instrumented with 26 thermocouples of NiCrNi Type K on the cold side, six on the base plate and twenty on the cylindrical HFI-Combustor wall. The static pressure was measured with Rosemount 1151 pressure transmitters at the plenum and upstream and downstream of the turbulence generator. The combustion air mass flow rate was computed based on a correlation between the mass flow rate and the pressure drop across the turbulence generator, following the standard procedure in this facility (The correlation was obtained from an effective area test performed prior to the HFI experiment). At three different mass flow rates, corresponding to bulk velocities of 115, 125, and 135 m/s at the jet outlet, we have varied the fuel mass flow rate to achieve equivalence ratios between 0.6 to 1.2. The sentences have been rephrased to avoid confusions. The experimental data was recorded after a warm-up period of at least 5 minutes, to ensure that steady wall temperatures and pressures were achieved.

### 7.2.3 Experimental Results

The occurrence of the first thermoacoustic radial mode, as predicted by numerical simulations, was the main objective of the testing. To detect self-excited thermoacoustic instabilities in experiments, pressure recordings and their Fourier transforms were used. The pressure fluctuations were sampled at a rate of 50 kHz. The Fourier transform was applied on the pressure signal every 60 ms during the recording. When self-excited high-frequency instabilities occurred for an operating point, a peak frequency was visible in the Fourier transform around 3 kHz and the amplitudes of the oscillations fluctuated around a mean value. Figure 7.3 shows an exemplary Fourier transform of the signal recorded by the three pressure transducers for an operating point with an equivalence ratio of  $\phi = 0.86$ , combustion air mass flow rate of  $\dot{m}_c = 118$  g/s and a total air mass flow rate of  $\dot{m}_{tot} = 187$  g/s with a temperature of  $T_{air} = 500$  K. In addition, the averaged Fourier transform of the 10 second pressure signal with a window of 60 ms is shown in Fig. 7.3. The averaged Fourier transform is used to distinguish the actual peaks from the instantaneous noise amplitude. The system clearly showed a peak at Lp1 and Lp3 with a frequency of 3.17 kHz for this operating point. At Lp2, the pressure fluctuation amplitude at 3.17 kHz is very small since Lp2 is located at the pressure node of the radial mode of the combustor. In Fig. 7.3, one can see that the instantaneous and average spectra from Lp1 and Lp3 showed different amplitudes at 3.17 kHz. Consequently, the level of the amplitude is not constant at this frequency. This is in line with the observation of the transient increase and decrease of the amplitude levels of the high-frequency oscillations in the experiment of Buschhagen et al. [53]. In addition to the high-frequency oscillations, the experimental results showed peaks at lower frequencies of 1.41 kHz, 0.76 kHz and 0.21 kHz.

An estimate of the mode shapes corresponding to the observed frequency can be made by solving the Helmholtz acoustic equation [64]. To this end, a tubular cylinder with a length of  $16.5D$  and a radius of  $4D$  with acoustically closed and open ends was considered. A uniform sound speed of 769 m/s was assumed, corresponding to a temperature of 1600 K. The estimated Longitudinal (Lg), Tangential (T) and Radial (R) resonant frequencies are listed in table 7.1.

**Table 7.1** Eigenfrequencies in Hz; Longitudinal (Lg), Tangential (T) and Radial (R) acoustic modes.

|        | 0Lg  | 1Lg  | 2Lg  | 3Lg  |
|--------|------|------|------|------|
| 0T, 0R | 0    | 293  | 880  | 1466 |
| 1T, 0R | 1418 | 1448 | 1669 | 2040 |
| 0T, 1R | 2951 | 2965 | 3079 | 3295 |

By comparing the peak frequencies observed in the experiment (see Fig. 7.3) with

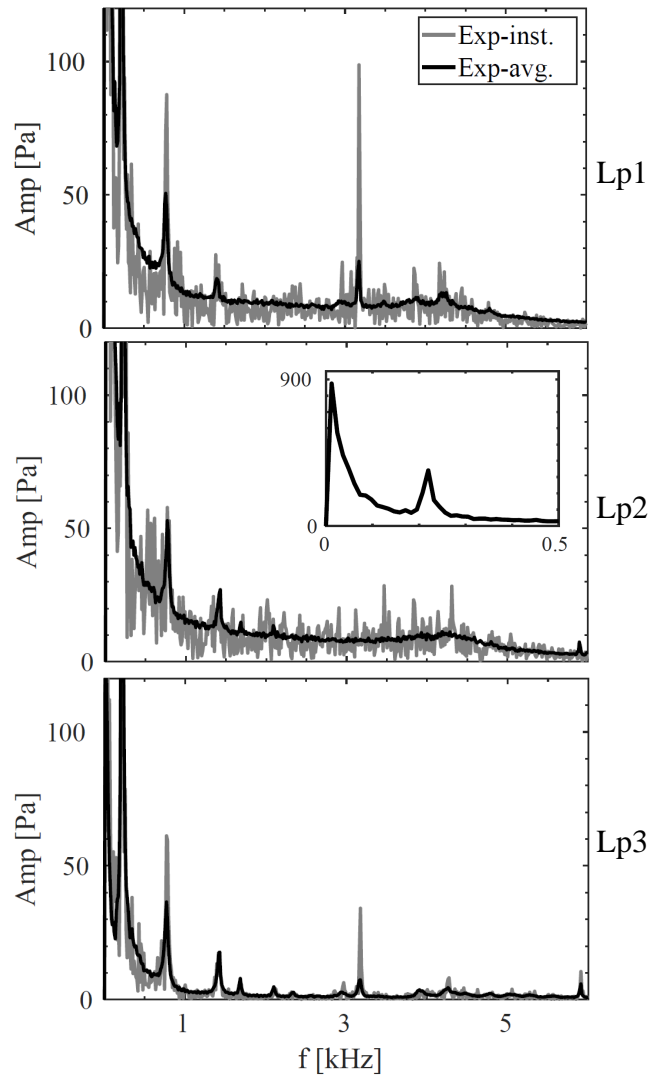


**Fig. 7.3** Fourier transform of the signals recorded by the three pressure transducers Lp1, Lp2 Lp3.

the estimated resonant frequencies (see table 7.1), one can conclude that the first and second peaks may correspond to the first and second axial modes of the combustor, and that the peak in the spectrum at 1.4 kHz may correspond to the first azimuthal mode, while the peak at 3.1 kHz may be the frequency of the first radial mode. The radial characteristic of the mode shape of the 3.1 kHz oscillations could be supported by examining the amplitude and phase information of the pressure signals over the radius of the HFI-Combustor. From Fig. 7.3 it can be seen that the peaks at 3.1 kHz are clearly visible at Lp1 (in the middle of the combustor) and Lp3 (on the combustor wall), with a slightly larger amplitude at Lp1. In between (at Lp2) no clear peak is identifiable at the desired high-frequency (3.1 kHz), characterizing the first radial acoustic mode. The phase difference of the pressure signal at Lp1 and Lp3 (at both sides of the acoustic pressure node) was measured to be  $160^\circ$  pointing to a standing mode with a portion of traveling waves. No statement can be given about the longitudinal character of the

transverse mode on the basis of the available pressure measurements.

The measured temperatures of the cylindrical wall of the HFI-Combustor are shown in Fig. 7.4 at different axial and circumferential positions of the combustor. An asymmetry of the wall temperature at each axial position is shown, with the strongest asymmetry at  $0.08L$ , where  $L$  denotes the length of the cylindrical part of the HFI-Combustor. The largest deviation in the wall temperature was detected in the upper position, where holes for measurement instrument cables were located. The cold air from this hole for cooling the combustion chamber is the main reason for the observed wall temperature asymmetry. The mean wall temperature in the cylindrical part of the combustor and in the base plate were 1135 K and 940 K, respectively (In section 7.3.3.2, it will be shown that such an asymmetry in the combustor wall temperature can significantly reduce the amplitude of the oscillations).

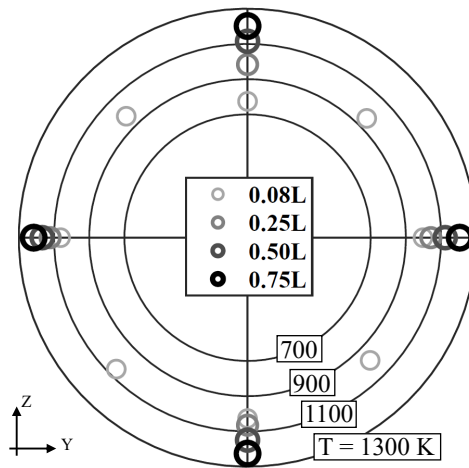


**Fig. 7.4** Wall temperature of the cylindrical part of combustor at the measured axial and tangential positions,  $L$  denotes the length of the cylindrical part of the HFI-Combustor.

In the following, we show only the amplitudes of the Fourier spectrum of the pressure signals recorded at  $Lp1$ . Since this work deals with high-frequency thermoacoustics, the low-frequency oscillations are also not considered any further. Figure 7.5 shows amplitude of high-frequency acoustic oscillations for different equivalence ratios. The equivalence ratio was reduced toward lean mixtures to the value of the data point to record data points. The grey-scale of the symbols in this figure indicates the frequency observed.

The results show that the system is most unstable at a slightly sub-stoichiometric condition. With leaner and richer mixtures, the amplitudes of instabilities were reduced. For an equivalence ratio of less than 0.68, no high-frequency thermoacoustic were observed any longer.

Figure 7.6 shows the mean wall temperature of the cylindrical chamber for  $U_j = 115$  m/s, representing an estimation of the temperature inside the combustor. It can be seen

that the temperatures first increased with increasing equivalence ratio to the stoichiometric condition and then decreased as expected. This tendency was reflected in the frequency of instabilities (see Fig. 7.5), which is linked to the natural frequency of the system and depends on the fluid temperature. In terms of changes in jet velocities (combustion mass flow rate), Fig. 7.5 shows that an increase in the jet velocity generally led to an increase in the susceptibility of the system to high-frequency instabilities and that the occurrence of instabilities with higher amplitude was shifted towards leaner mixtures. A similar behavior of instabilities with respect to mass flow rate was also observed by Sattelmayer [44, 21]. To illustrate the influence of jet velocities (combustion mass flow) on the susceptibility of the system to thermoacoustic instabilities even more clearly, Fig. 7.7 shows the results for a constant equivalence ratio of  $\phi \approx 0.86$  for different jet velocities. The figure shows that a 40 % increase of the jet velocity results in an increase of about 30 % in the amplitude of high-frequency oscillations. This behavior can be explained by the power density inside the combustion system, which increases with mass flow rate and tends to strengthen the high-frequency instabilities of the combustion [175]. Overall, the experiment showed that this combustor features high-frequency thermoacoustics, as predicted by the simulations before the combustor was built.

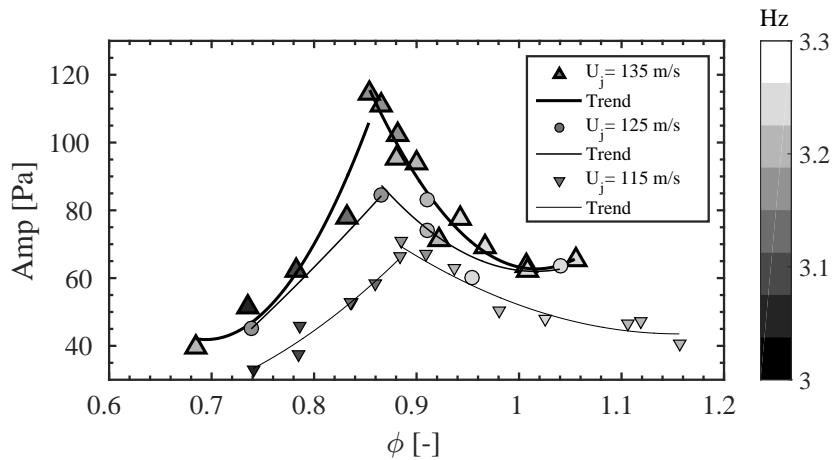


**Fig. 7.5** Amplitude of the acoustic oscillations at Lp1 versus the global equivalence ratio, the greyscales illustrate the frequency of the oscillations.

## 7.3 Numerical Investigation

### 7.3.1 Test Cases and Operating Points

The numerical investigations presented and discussed in the following subsections are based on the experimental setup and were performed subsequent to the experiments. The simulations were mainly performed to evaluate their predictive capability with respect to high-frequency thermoacoustic instabilities. In order to avoid uncertainties,

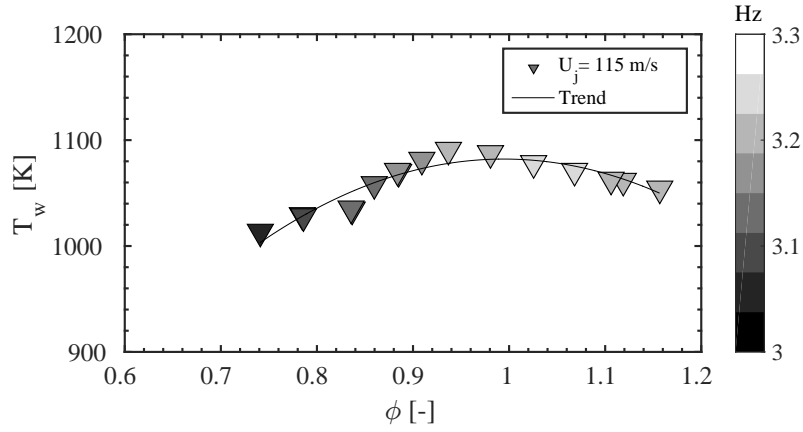


**Fig. 7.6** Average HFI-Combustor wall temperature as a function of equivalence ratio.

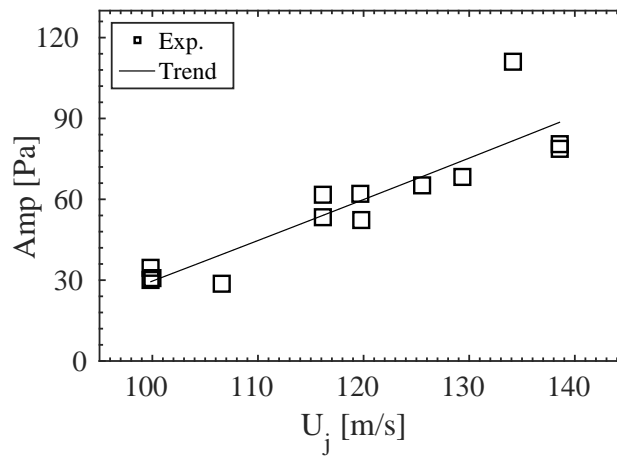


**Fig. 7.7** Amplitude of the acoustic oscillations at Lp1 versus the estimated bulk jet velocity at  $\phi \approx 0.8$ .

the computational configuration was chosen to be as similar as possible to the experimental configuration, avoiding any oversimplification. The main difference between the experimental and computational setup was the (negligible) amount of air leakage in the experiment, which was not considered in the simulation (The purge air for cooling the pressure transducers, which directly changed the temperature distribution within the combustion chamber, was considered). The air mass flow rate at the inlet of the computational domain was adjusted to achieve the desired combustion air mass flow rate of the experiment. To test the capability of the numerical methods for predicting high-frequency thermoacoustic oscillations, an unstable operating point was selected. The operating point considered for LES corresponds to a preheated fresh air temperature of 497 K and a combustion air mass flow rate of  $\dot{m}_c = 107$  g/s, which corresponds to a bulk velocity of 120 m/s and Reynolds number of  $Re_j = 1.2 \cdot 10^5$  at the jet outlet. Since the natural gas composition used in the experiment consisted mainly of methane (94%), pure methane was assumed for the simulation. Methane was injected at a temperature of 297 K with a fuel mass flow rate of  $\dot{m}_F = 5.2$  g/s through injection holes perpendicular

to the main flow. The investigated operating point has a thermal power of  $P_{th} = 0.2$  MW with a global equivalence ratio of  $\phi = 0.85$ . To ensure that the predicted high-frequency instabilities for the unstable point were not caused by numerical oscillations, a stable point (with respect to HFI) was also simulated, with a preheated air temperature of 499 K, a global equivalence ratio of  $\phi = 0.63$ , a combustion air mass flow rate of  $\dot{m}_c = 103$  g/s and a fuel (methane) mass flow rate of  $\dot{m}_F = 3.8$  g/s. The computational domain spanned from the cylindrical pipe after the air compressor and air preheater to the cylindrical part of the exhaust pipe (see Fig. 7.2). The inlet boundary was thus set far away from the region of interest. The fixed mass flow rate was set at the inlet of the test rig. Since most of the turbulence was generated by the geometrical turbulence generator device, no artificial turbulence was superimposed to the inlet. The exhaust pipe of the experimental setup is discharged into the environment and is located about 225D downstream of the HFI chamber. To simplify the simulations, the entire exhaust pipe was not simulated. The outlet boundary of the computational domain was located at a distance of 60D downstream of the HFI chamber. To avoid reflections at this boundary a partially non-reflecting boundary conditions [145] were assigned to the pressure field at the outlet of the system to simulate an infinitely long outlet by eliminating acoustic reflections. It is assumed that neglecting the acoustic reflection at the end of the exhaust pipe of the experiment, introduces small errors. This is especially applicable to high frequencies, which are of interest in this work, since they can be attenuated more strongly due to their small wavelength. Furthermore, the numerical design simulations before the experiment (see Sec. 7.2.1) revealed that the downstream acoustic boundary has almost no influence on the HFI, evidencing that the reflection level at this boundary is less critical for high-frequency instabilities. The cylindrical part of the HFI-Combustor wall was divided into 16 sections and the base plate into 2 sections for which measured temperatures known from the experiment were applied. The mean wall temperature for the unstable operating point was 1070 and for the stable operating point 870 K. In the simulation, heat conduction inside the solid material and heat losses due to radiation were neglected. The other parts of the combustor were assumed to be adiabatic as they were either coated or isolated. To investigate the impact of the HFI-Combustor wall temperature asymmetry observed in the experiment, an idealized configuration with the same combustion mass flow rate and equivalence ratio as the unstable point was simulated. In this configuration, the temperature of the HFI-Combustor walls was set to a uniform temperature corresponding to the mean wall temperature of 1070K. In this simulation the entry of the purge air was not considered, to avoid disturbances in the temperature fields.

### 7.3.2 Modeling and Simulation

Computations were carried out with the compressible and reactive LES of the implicit code OpenFOAM [145]. A Flame Surface Density model (FSD) was used to account for combustion. In this model, flame propagation is expressed using a transport equation (Eq. 7.1) for the Favre-filtered reaction regress variable  $\tilde{b}$  and reads:

$$\frac{\partial(\bar{\rho}\tilde{b})}{\partial t} + \frac{\partial\bar{\rho}\tilde{b}u_i}{\partial x_i} - \frac{\partial}{\partial x_i}(\bar{\rho}D_t\frac{\partial\tilde{b}}{\partial x_i}) = -\bar{w}_c + \frac{\partial}{\partial x_i}(\overline{\rho D_m\frac{\partial b}{\partial x_i}}) = -\rho_{ub}S_l\Sigma_{gen} \quad (7.1)$$

The reaction regress variable can be expressed using the well-known reaction progress variable  $c$  and is defined as:

$$b := 1 - c = 1 - \frac{T - T_{fr}}{T_b - T_u} \quad (7.2)$$

In Eq. 7.2, the subscripts  $b$  and  $u$  represent the conditioning of the burned gases and the fresh gas, respectively. In Eq. 7.1,  $D_m$  and  $D_t$  respectively represent the molecular and sub-grid diffusion coefficients. The source term and the molecular diffusion term can be modelled with the generalized flame surfaced density  $\Sigma_{gen}$ . The laminar flame speed  $S_l$  used in Eq. 7.1 is representative of chemistry and was assumed to be a function of the mean pressure, the mean temperature and the local equivalence ratio and were tabulated prior to LES by simulating one-dimensional, laminar freely propagating pre-mixed flames in Cantera [100] using GRI 3.0 mechanism [77]. The generalized flame surface density can be expressed by the flame wrinkling factor  $\Xi$  and the magnitude of the regress variable gradient as:

$$\Sigma_{gen} = \Xi|\nabla\bar{b}| \quad (7.3)$$

Thus, the modelling of the interaction of sub-grid turbulence and combustion can be reduced to a model for the flame wrinkling factor on the sub-grid scale. This work used an algebraic expression [147, 146] inspired by Bradley [111] that reads:

$$\Xi = 1 + \frac{C}{Le} \sqrt{\frac{u'_{sgs}\Delta}{a_l}} \quad (7.4)$$

In the above equation,  $Le$  is the Lewis number,  $C$  is a model constant and  $\Delta$  the cut-off length. The value of the constant was set to 0.5, as suggested in previous work [35, 146]. The sub-grid scale velocity fluctuation  $u'_{sgs}$  is calculated from the sub-grid turbulent kinetic energy:

$$u'_{sgs} = \sqrt{\frac{2k_{sgs}}{3}} \quad (7.5)$$

The transport equation for the sub-grid scale kinetic energy, proposed by Yoshizawa

et al. [97] and Menon et al. [98] was solved [99]:

$$\frac{\partial(\bar{\rho}k_{sgs})}{\partial t} + \frac{\partial(\bar{\rho}\tilde{u}_j k_{sgs})}{\partial x_j} - \frac{\partial}{\partial x_j}(\bar{\rho}(\nu + \nu_t)\frac{\partial k_{sgs}}{\partial x_j}) = -\rho\tau_{ij}\tilde{S}_{ij} - C_\epsilon \frac{\rho k_{sgs}^{3/2}}{\Delta} \quad (7.6)$$

In the above equation,  $\nu$  represents the molecular viscosity and  $\nu_t$  represents the sub-grid scale eddy viscosity, which can be expressed as:

$$\nu_t = C_k \Delta \sqrt{k_{sgs}} \quad (7.7)$$

The constants in the model were set to  $C_\epsilon = 1$  and  $C_k = 0.09$  as proposed by Yoshizawa et al. [97].

The temperature is iteratively calculated from NASA polynomials and a transport equation for the filtered specific absolute enthalpy, as described in previous work [35, 146]. The heat losses from the boundaries are considered by setting the Dirichlet boundary condition for the isothermal walls.

The computational domain was discretized using 20 million cells. The unstructured grid consisted of regions with different cell sizes, mostly hexahedrons in the inner part of the domain and collapsed hexahedrals close to the surface, to generate body-fitted meshes. The cell sizes in the cylindrical chamber and the premixing passage were chosen specifically to ensure at least 130 cells over a wave length of the desired first radial mode. The mixing passage and the flame region were discretized using 1 mm cells, the cell size for which the combustion model was validated [35]. The near wall region of the HFI-Combustor was discretized with 0.5 mm cells. The small nozzle of the turbulence generator were discretized so that at least 6 cells were guaranteed over the diameter of the holes. A finer discretization was not affordable at these locations.

Convective fluxes of momentum were discretized with the *filteredLinear* scheme [116], which is a limited combination of a low-order (LO) and a high-order (HO) schemes.

$$\Phi_f = (\Phi_f)_{LO} + \Psi[(\Phi_f)_{HO} - (\Phi_f)_{LO}] \quad (7.8)$$

In Eq. 7.8, the flux limiter function is represented by  $\Psi$ . The scheme compares the face gradients with the gradients of two adjacent cells. Based on this comparison, between 0-20% upwinding was introduced through the flux limiter to suppress numerical fluctuations [163].

For advancing the solution in time, a blended scheme was used which employs an off-centering coefficient  $0 \leq C_n \leq 1$  and is defined as:

$$\Phi^{n+1} = \Phi^n + \frac{1}{(C_n + 1)} [\text{RHS}(\Phi^{n+1}) + C_n \text{RHS}(\Phi^n)] \Delta t \quad (7.9)$$

In the above equation,  $\Phi^n$  and  $\Phi^{n+1}$  represent the solution in the current and next

time steps, respectively, and RHS denotes the discretized transport equation without the accumulation term. The scheme turns to a Crank–Nicolson scheme [123] or Euler implicit scheme [176] when  $C_n = 1$  or  $C_n = 0$ , respectively; In the present paper a coefficient of 0.9 was used and a fixed time step was chosen, which corresponds to an acoustic Courant–Friedrichs–Lewy (CFL) number of 0.3 in the flame region. The modeling and simulation methods were validated in previous work [147, 35].

For the simulation of the unstable and stable point, the simulations were performed separately from their corresponding initial states. For the initialization of the flame, a ring-shaped region (with the diameter of the premix passage  $D$ , a length of  $6D$  and a thickness of  $0.25D$ ) was initialized with the adiabatic flame temperature at the corresponding equivalence ratio. The upstream region of this volume was adjusted to the fresh mixture and the downstream volume to the burnt mixture with an average temperature corresponding to the wall of the combustion chamber. The pressure field and the velocity field are initialized with atmospheric pressure and 0 m/s. The numerical setup (i.e. the method of discretization, numerical parameters, and the mesh strategy and cell sizes) was kept identical for both simulations.

To evaluate the thermoacoustic mechanisms, we used the procedure described in previous work [35] on forced thermoacoustic and modified it to include additional terms. The local heat release rate  $\dot{q}$  in the context of the flame surface density can be defined as [64]:

$$\dot{q} = \rho_u S_l \Xi |\nabla b| H ft \quad (7.10)$$

In Eq. 7.10,  $H$  represents the heat of reaction per mass of fuel and  $ft$  the fuel mass fraction. By linearization of the equation around the mean heat release rate  $\dot{q}_0$  and integrating it over the combustor volume  $V$ , the contribution of density oscillations  $\dot{Q}_\rho$ , laminar flame speed oscillations  $\dot{Q}_{S_l}$ , oscillations of the sub-grid wrinkling factor  $\dot{Q}_\Xi$ , oscillations of burning area  $\dot{Q}_A$  and fuel mass fraction oscillations  $\dot{Q}_{ft}$  to the global heat release rate oscillations  $\dot{Q}_1$  can be determined and reads:

$$\begin{aligned} \dot{Q}_1 = \int_V \dot{q}_1 dV \approx & \underbrace{\int_V \frac{\rho_{u1}}{\rho_{u0}} \dot{q}_0 dV}_{\dot{Q}_\rho} + \underbrace{\int_V \frac{S_{l1}}{S_{l0}} \dot{q}_0 dV}_{\dot{Q}_{S_l}} + \\ & \underbrace{\int_V \frac{\Xi_1}{\Xi_0} \dot{q}_0 dV}_{\dot{Q}_\Xi} + \underbrace{\int_V \frac{|\nabla b|_1}{|\nabla b|_0} \dot{q}_0 dV}_{\dot{Q}_A} + \underbrace{\int_V \frac{ft_1}{ft_0} \dot{q}_0 dV}_{\dot{Q}_{ft}} \end{aligned} \quad (7.11)$$

The index 0 represents the mean value and 1 its fluctuations. Considering the phase-averaged variables, the terms with superscript 1 refer to the acoustic oscillations. The Rayleigh Index can be expressed as the multiplication of the pressure oscillations  $p_1$

and heat release rate oscillations  $q_1$  [64]:

$$RI = \frac{\gamma - 1}{\gamma p_0 t_p} \int \int_{t_p V} p_1 \dot{q}_1 dV dt \quad (7.12)$$

In Eq. 7.12,  $\gamma$  indicates the specific heat ratio and  $t_p$  the period of the acoustic oscillations. By replacing  $q_1$  with its linearized form, in the definition of the Rayleigh index (Eq. 7.12), one can compute the contribution of density oscillations ( $RI_\rho$ ), laminar flame speed oscillations ( $RI_{S_l}$ ), wrinkling factor oscillations  $RI_\Xi$ , flame area oscillations ( $RI_A$ ) and fuel mass fraction oscillations ( $RI_{f_t}$ ) to the total Rayleigh Index:

$$RI \approx \underbrace{\frac{\gamma - 1}{\gamma p_0 t_p} \int \int_{t_p V} p_1 \frac{\rho_{u1}}{\rho_{u0}} \dot{q}_0 dV dt}_{RI_\rho} + \underbrace{\frac{\gamma - 1}{\gamma p_0 t_p} \int \int_{t_p V} p_1 \frac{S_{l1}}{S_{l0}} \dot{q}_0 dV dt}_{RI_{S_l}} + \underbrace{\frac{\gamma - 1}{\gamma p_0 t_p} \int \int_{t_p V} p_1 \frac{\Xi_1}{\Xi_0} \dot{q}_0 dV dt}_{RI_\Xi} + \underbrace{\frac{\gamma - 1}{\gamma p_0 t_p} \int \int_{t_p V} p_1 \frac{|\nabla b|_1}{|\nabla b|_0} \dot{q}_0 dV dt}_{RI_A} + \underbrace{\frac{\gamma - 1}{\gamma p_0 t_p} \int \int_{t_p V} p_1 \frac{f_{t1}}{f_{t0}} \dot{q}_0 dV dt}_{RI_{f_t}} \quad (7.13)$$

In eq. 7.13,  $RI_\rho$  deals with the impact of density oscillations on heat release rate oscillations and can be linked to the flame shape deformations mechanism proposed by Hummel et al. [46].  $RI_A$  includes the contribution of flame surface area changes due to transverse acoustic velocity e.g. by flame displacement mechanism [44] or by flame breathing mechanism [35]. This term also considers the flame surface area changes due to vortex shedding [35].  $RI_{S_l}$  is capable of considering changes in laminar flame velocity by various pathways, e.g. due to pressure/chemical mechanism [38, 35], change in equivalent ratio oscillations, or due to strain modulation [42]. For the combustion model used in this paper (eq. 7.2), the laminar flame velocity is assumed to be a function of mean pressure, mean temperature and local equivalent ratio.  $RI_{f_t}$  take the local changes in the equivalence ratio on the heat release rate oscillation, which can be linked to the equivalence ratio coupling Mechanism [155, 177, 31]. It must be stressed that  $RI_\Xi$  is affected by the sub-grid turbulence model (eq. 7.4, which was not developed to consider the effect of high-frequency pressure perturbations.

### 7.3.3 Numerical Results

Each simulation was run for at least three flow-trough times in order to achieve a limit cycle with a stable amplitude. This required a physical time of 1 second, at a cost of 1.5 million core hours.

### 7.3.3.1 Comparison with Experiment

The 10 ms of the pressure signal acquired from LES of the unstable point is compared to the raw pressure signal from the experiment in Fig. 7.8a, indicating a similar qualitative behavior. Quantitative comparison of the results can be achieved by comparing the Fourier transform of the signals as shown in 7.8b. The Fourier transforms were performed on 60 ms of the signals. It was found that the LES predicted a significant peak at 3052 Hz with a comparable oscillation amplitude to the experimental result of 3162 Hz. In addition, LES was able to predict peaks in the mid-frequency range in the experiment. Table 7.2 lists the differences between the predicted peak frequencies of the LES and those observed in the experiment for the pressure oscillations recorded at Lp1. The frequency of the radial mode was underestimated by 110 Hz. It should be, however, noted that precise predictions of the frequency are only possible by predicting the correct temperature in the system. A first estimation of the impact of the mean temperature on the frequency of the radial mode can be determined based on a simple acoustic analysis. In a tubular cylinder the eigenfrequency of the first acoustic radial mode can be approximated from [178]:

$$f_{R1} = a \frac{\beta_{0,1}}{\pi D_c} \quad \text{with} \quad a = \sqrt{\gamma R' T} \quad (7.14)$$

In Eq. 7.14,  $a$  denotes the sound speed and  $\beta_{0,1} = 3.83$  [178] represents the root of the derivative of the Bessel function for the first radial mode. For a mixture in a tubular cylinder with a radius  $D_c$  assuming a constant heat capacity ratio  $\gamma$ , the natural frequency is a function of the sound speed and consequently of the mixture temperature. Thus, for a pure radial mode with a frequency of 3052 at 1600 K, a deviation of the mean temperature of about 120 K can cause a frequency deviation of 110 Hz.

The temperatures measured by the circumferential sensors at each axial position were averaged and shown in Fig. 7.9, indicating an increase in wall temperature in the axial direction. Considering the estimated temperature trend, neglecting the axial distribution of the wall temperature in the last section of the HFI combination could have led to an underestimation of the temperature in the combustor.

**Table 7.2** LES vs. experiment: Differences in amplitudes and frequencies of observed peaks.

|                | 1. peak  |        | 2. peak  |        | 3. peak   |        | 4. peak   |        |
|----------------|----------|--------|----------|--------|-----------|--------|-----------|--------|
|                | Amp [Pa] | f [Hz] | Amp [Pa] | f [Hz] | Amp. [Pa] | f [Hz] | Amp. [Pa] | f [Hz] |
| Experiment     | 235      | 219    | 52       | 790    | 29        | 1403   | 63        | 3160   |
| LES            | 82       | 219    | 46       | 820    | 14        | 1401   | 116       | 3050   |
| Deviation in % | 65       | 0      | 11       | -3.8   | 52        | 0.14   | -84       | 3.5    |

A comparison of the mode shapes obtained from LES and experiment can be seen

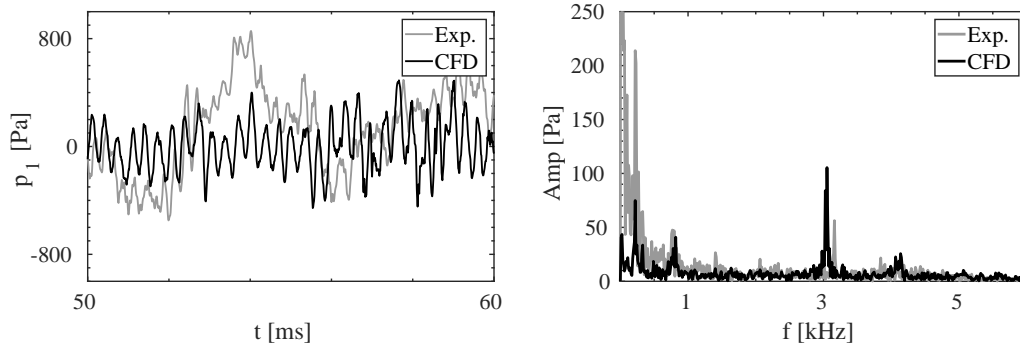


**Fig. 7.8** Comparison of the experimental data with the LES results for the unstable operating point at Lp1, signal over time (left) and the Fourier transform (right).

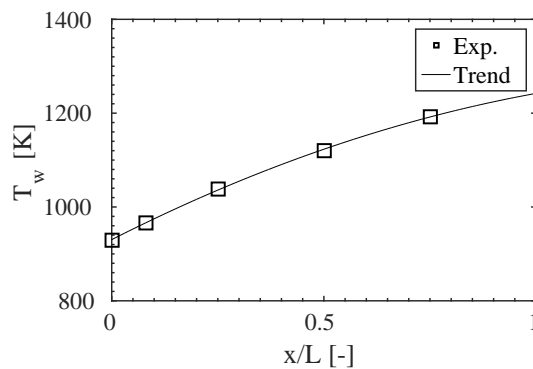


**Fig. 7.9** Mean measured temperature as a function of the HFI-Combustor length,  $L$  denotes the length of the cylindrical part of the HFI-Combustor.

in Fig. 7.10, which illustrates the amplitude of the acoustic oscillations at the peak frequency of 3 kHz at the location of the pressure transducers. It should be noted that Lp1 and Lp2 are mounted at a radial distance of 1.25 D and 2.5 D from the chamber centerline on the base plate (at  $x=0$  L) of the combustor. Lp3, on the other hand, is mounted on the combustion chamber wall at an axial distance of  $x=0.25$  L. At these axial positions the amplitudes of the acoustic oscillations along the chamber radius, predicted by the LES, are presented. It can be seen that the characteristic amplitude behavior of the first radial mode with its maximum toward the center (at Lp1) of the combustor and at the chamber wall (at Lp3) and its minimum in between (at Lp2) could be reproduced by the LES.

In order to verify a) that the observed oscillations were not obtained by chance or error cancellation and b) that LES was able to predict the stable combustion, the LES of the stable point was also carried out. The temporal evolution of 10 ms of the pressure signal and the Fourier transform of 60 ms of the pressure signals are presented and compared in Fig. 7.11. The pressure signals were recorded at Lp1 for this purpose. As expected, no significant high-frequency in either the simulation or in the experiment (compare with Fig. 7.8), which confirms the physical relevance of the predicted ther-

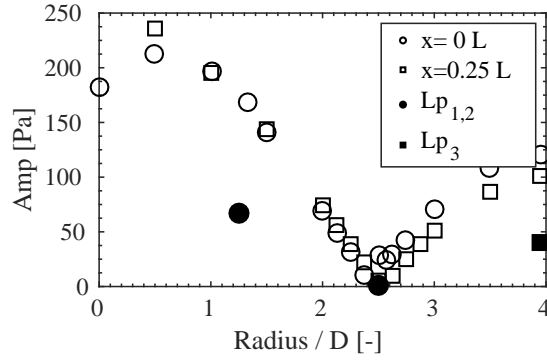


**Fig. 7.10** HFI-Amplitude versus HFI-Combustor radius. Filled points: experiment, hollow points: CFD.

moacoustic instabilities at the unstable operating point. Here, it can also be observed that the LES was able to predict the intermediate frequency peaks.

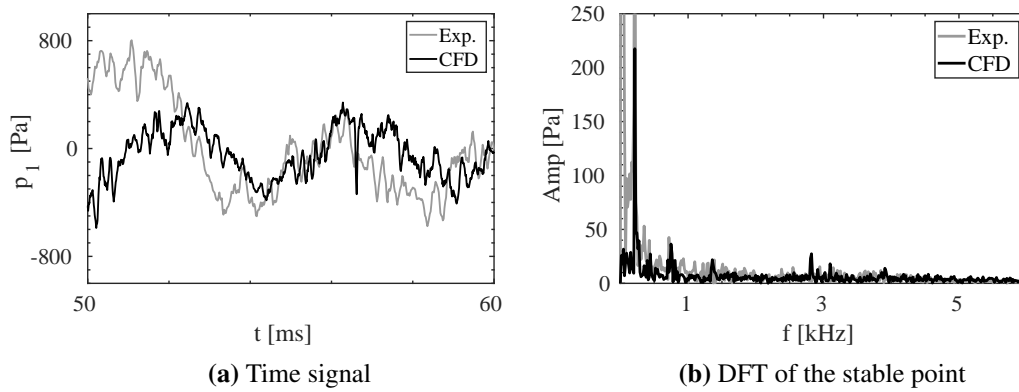


**Fig. 7.11** Comparison of the experimental data with the LES results for the stable point at Lp1.

### 7.3.3.2 Realistic vs. uniform combustor wall temperatures

Fuel staging is one of the well-known method for the mitigation of thermoacoustic instabilities in combustors of gas turbines [11]. The disturbance of the temperature fields and thus the disturbance of the acoustic mode shapes are the key elements to this damping method. Accordingly, we have investigated the influence of temperature non-uniformities on the high-frequency thermoacoustic instabilities observed in the experiment. To this end, LES was performed with an idealized configuration for the unstable operating point. For the idealized LES, a uniform temperature of 1070 K was set for the wall of the HFI-Combustor, which corresponds to the mean wall temperature of the unstable operating point. In addition, the cooling holes in the transducers were closed to prevent the entrance of cold purge air. For convenience, we name this configuration with uniform wall temperature, UTC, and the configuration with realistic (measured) wall temperature, RTC, which was discussed in the last chapter in 7.3.3.1. It must be

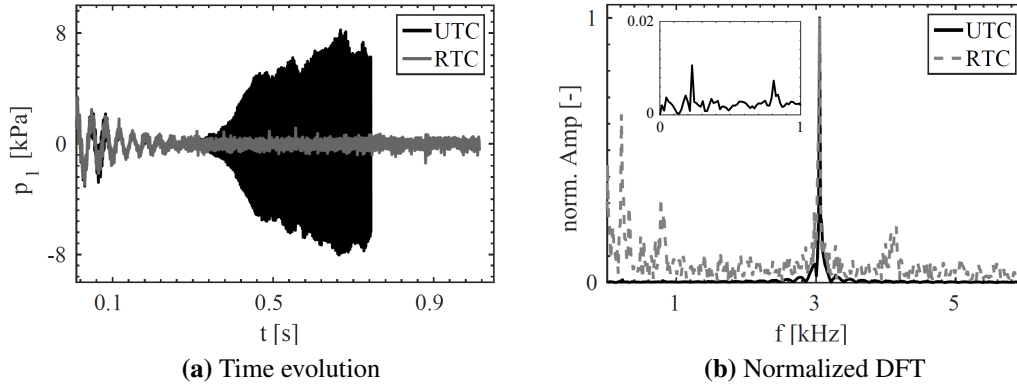


**Fig. 7.12** Comparison of the pressure signal for UTC and RTC.

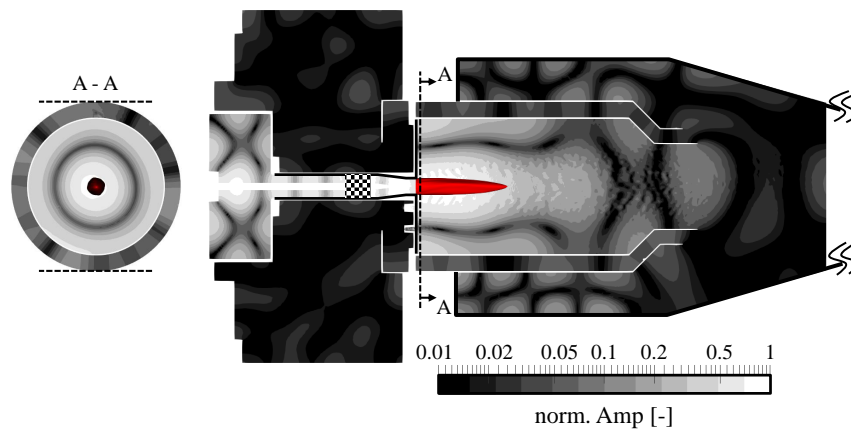
clear to the reader that no experimental data are available for UTC. In contrast, there are experimental data available for RTC, which are discussed in Fig. 7.8.

The time evaluation of the pressure signals are compared in Fig. 7.12a for both configurations. The figure illustrates that for UTC the initial fluctuation was then organized and the amplitude of the high-frequency oscillations increased exponentially until a limit cycle amplitude with a frequency of 3 kHz was reached, as shown in the Fourier transform of the signal in Fig. 7.12b. In contrast, the growth rate of high-frequency oscillations in the RTC was lower and a smaller amplitude was reached in the limit cycle. Both configurations exhibited a comparable peak frequency for high-frequency oscillations, as shown in Fig. 7.12b. The amplitude of the Fourier transform was normalized by the maximum amplitude of 3 kHz, which is 105 Pa for RTC and 6440 Pa for UTC. The peaks observed at the intermediate frequencies of 0.2 kHz and 0.8 kHz for the RTC were also present in the Fourier transform of UTC, but with a significantly lower amplitude than the peak at high-frequency instabilities for this configuration.

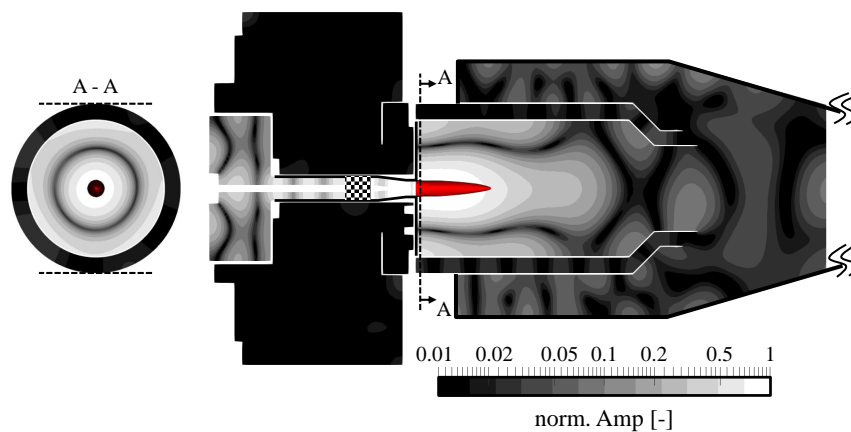
Figure 7.13 illustrates the fields of normalized amplitude distribution of the high-frequency oscillations. The amplitude distribution was obtained by performing the Fourier transform on the last 50 periods of the pressure signal at each computational cell. The fields of the pressure amplitude distribution were normalized with the maximum amplitude observed in each simulation over the center-line of the HFI-Combustor. In addition, the average position of the flame was visualized by the iso-surface of the regression variable  $\bar{b} = 0.5$ . As expected, the evaluated mode shapes of the two simulations have the same characteristics of the first radial mode as they occurred with similar frequencies. However, the pressure-anti-node area around the flame was more dominant with UTC than with RTC. The figure reveals that the heat release rate region for UTC is more compact (for a better comparison see Fig. 7.21), meaning the flame in the UTC had a higher local energy density. The reason for a shorter flame could be the presence of larger vortices in the case of UTC (see 7.15b), which are mainly caused by the larger pulsation amplitude in this case. This results in a bigger flame surface and a

shorter flame with the same amount of global heat release rate. Figure 7.15 shows the line-of-sight integration of the phase-average heat release rate for four phases during an acoustic cycle. The volume-integrated pressure oscillations for these phases are also illustrated in this figure. For the 1R mode, acoustic pressure anti-node is generated at the center-line of the combustor at the burner outlet (see Fig. 7.13). The acoustic pressure pulsation can travel upstream through the mixing passage as an axial wave, which causes symmetric vortex shedding at the burner outlet [35]. The axial characteristic of the acoustic can be observed from the axial acoustic velocity and its phase, illustrated in Fig. 7.14.

In Fig. 7.15, one can observe oscillations in the total intensity of heat release, especially at the UTC, with maximum intensity at  $90^\circ$  and minimum intensity at  $270^\circ$ . This is due to density fluctuations caused by pressure fluctuations.



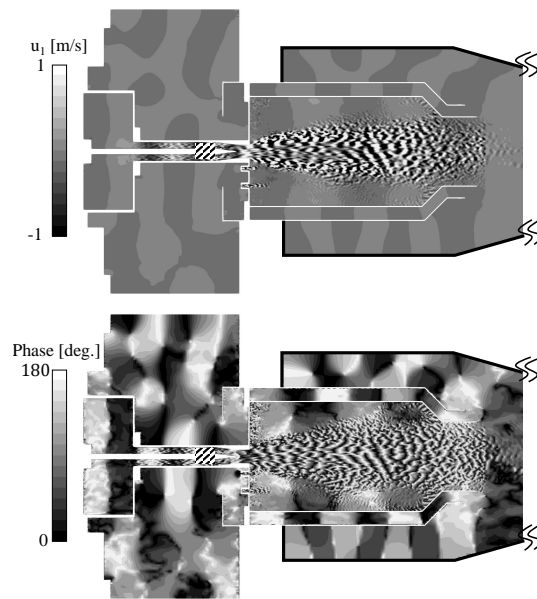
(a) RTC, normalization factor 0.28 kPa.



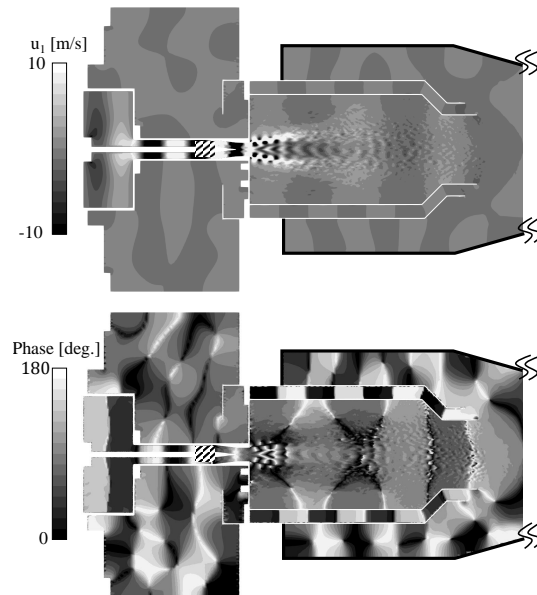
(b) UTC, normalization factor 9.1 kPa.

**Fig. 7.13** Comparison of the acoustic mode shape obtained from DFT for the RTC and UTC; Amplitude distribution is normalized with the maximum amplitude along the center-line of the HFI-Combustor (norm. Amp = normalized amplitude).

The instantaneous and time-averaged fields of the axial velocity are illustrated in Fig. 7.16. The air flowed through the premixing passage into the combustor. The



(a) RTC.



(b) UTC.

**Fig. 7.14** Comparison of the axial acoustic velocity and its phase obtained from DFT for RTC and UTC.

fuel was mixed through nozzles in the turbulence generator device. The instantaneous velocity fields clearly show the resulting vortical structures that enter the combustor. The velocity fields in the chamber are characterized by a high shear layer between the jet and the surroundings, which is typical for non-swirled flame stabilization methods. With the RTC, the inlet of the purge air, which had an air mass flow rate of 10 g/s is clearly visible.

The time-averaged and instantaneous temperature fields for the simulations of RTC and UTC of are shown in Fig. 7.17 and Fig. 7.18 respectively. Time averaging was per-

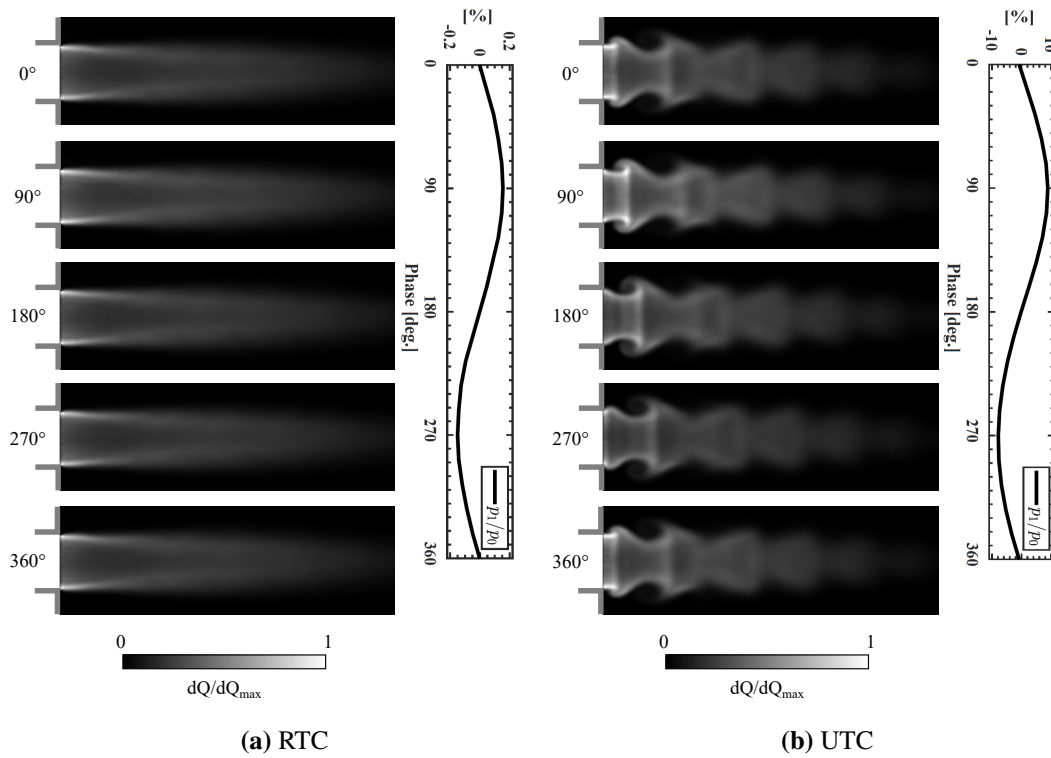


**Fig. 7.15** Phase-averaged line of sight fields of heat release rate for different phases of the unsteady pressure  $p_1$ .

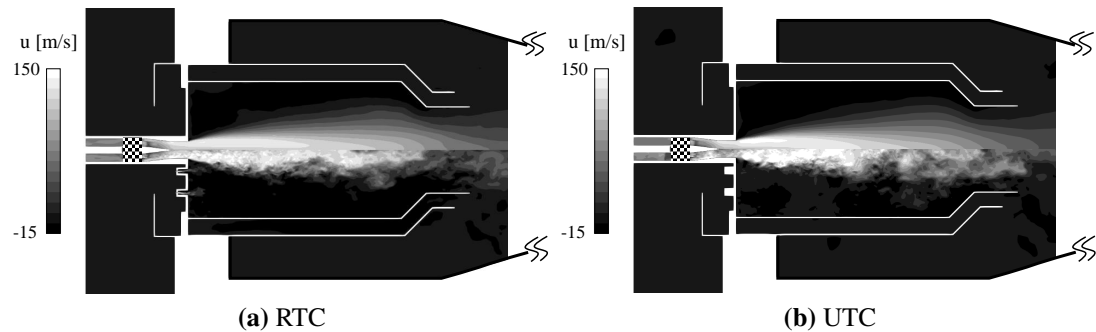


**Fig. 7.16** Comparison of instantaneous (lower half) and time-averaged (upper half) fields of the axial velocity for RTC and UTC.

formed on the last 200 ms of the simulations. In comparison to the UTC, the asymmetry of the mean temperature field is more pronounced for the RTC. This asymmetry might be caused by a) inhomogeneities in wall temperatures and b) entrance of cold purge air. In UTC, an asymmetry in the temperature fields can also be observed, but it is much less dominant than in RTC. This is due to the fact that the jet that enters the combustor is not axisymmetric, which is due to the characteristics of the turbulence generator device that was used.

To quantitatively demonstrate the asymmetry within the combustor, Fig. 7.19 compares the normalized mean temperature and axial velocity over the radius of the com-

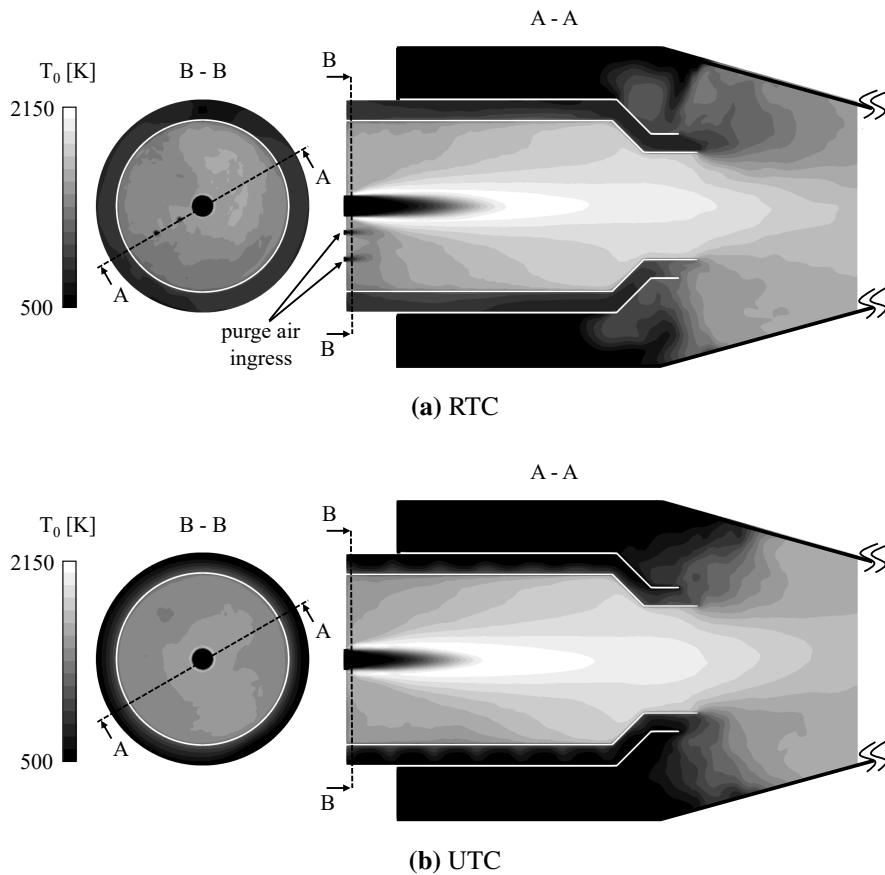


**Fig. 7.17** Comparison of the time-averaged temperature field for RTC and UTC.

bustor at the top and bottom parts of the combustor over the line A-A (see Fig. 7.17) for both configurations. While the temperature and velocity on both sides of the chamber were almost identical in the UTC, they varied considerably in the RTC. As in Fig. 7.19a, the temperature deviation of the sides of the combustion chamber near the base plate is significant for the RTC (see X/D 0 to 1). Note that the amplitude of the radial mode is more significant near the base plate and decays further downstream. Thus this disturbance may be more relevant here. This deserves special attention and needs further investigation.

It should be noted that for the idealized configuration, no experimental results are available. However, since it was shown in the last section that the numerical methods used were able to predict high-frequency thermoacoustics, we may trust the results of this idealized simulation. A final proof of why the system with identical combustion boundary conditions (mass flow rate and equivalence ratio) but non-uniform wall temperatures was less susceptible to high-frequency instabilities could not be given here and further investigation is required. However, it turned out that uniform temperatures on the walls were crucial to develop a test case for radial thermoacoustic instabilities with high amplitudes.

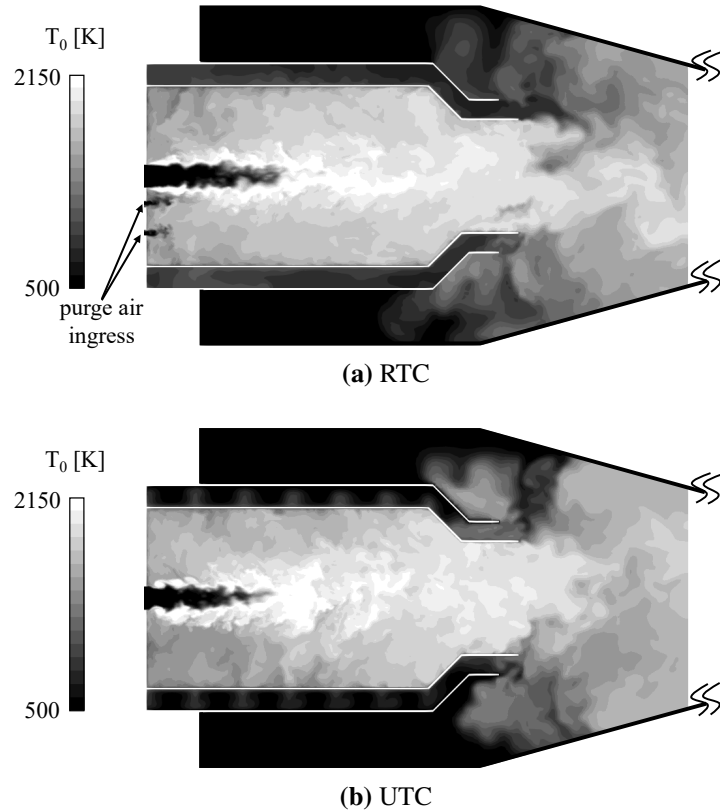


**Fig. 7.18** Comparison of the instantaneous temperature field for RTC and UTC.

#### 7.3.4 Mechanism of instabilities

To shed light on the mechanisms of high-frequency instabilities, it is possible to evaluate the different terms that cause oscillations in the heat release rate. In general, heat release rate can directly oscillate due to oscillations in the density, flame speed, equivalence ratio and flame surface. It should be mentioned that these parameters may mutually influence each other and indirectly cause the heat release rate oscillations, but here the more direct impact is discussed.

For evaluating thermoacoustic instabilities in the high-frequency range, it is mainly assumed that the acoustic wavelength is smaller than the characteristic flame length. In this case, the Rayleigh index (see Eqs. 7.12 and 7.13) should be considered because the evaluation of the global heat release oscillation would not be meaningful. This is especially the case at combustor with multijet burners under 1T mode. However, in our case for the 1R mode, the single flame is located in the acoustic pressure anti-node (see Fig. 7.13). Hence, the pressure in the flame region oscillates spatially in phase, as it is characteristic for standing waves. Therefore, it makes sense to deal with the global oscillations of the heat release rate (see Eq. 7.11) for this case. The normalized fluctuations of the phase-averaged global heat release rate  $\dot{Q}_1$  and the volume-averaged pressure  $p_1$  for two periods of oscillation are shown in Fig. 7.20 for RTC and UTC. For the spatial averaging of the pressure, a volume around the flame was considered in

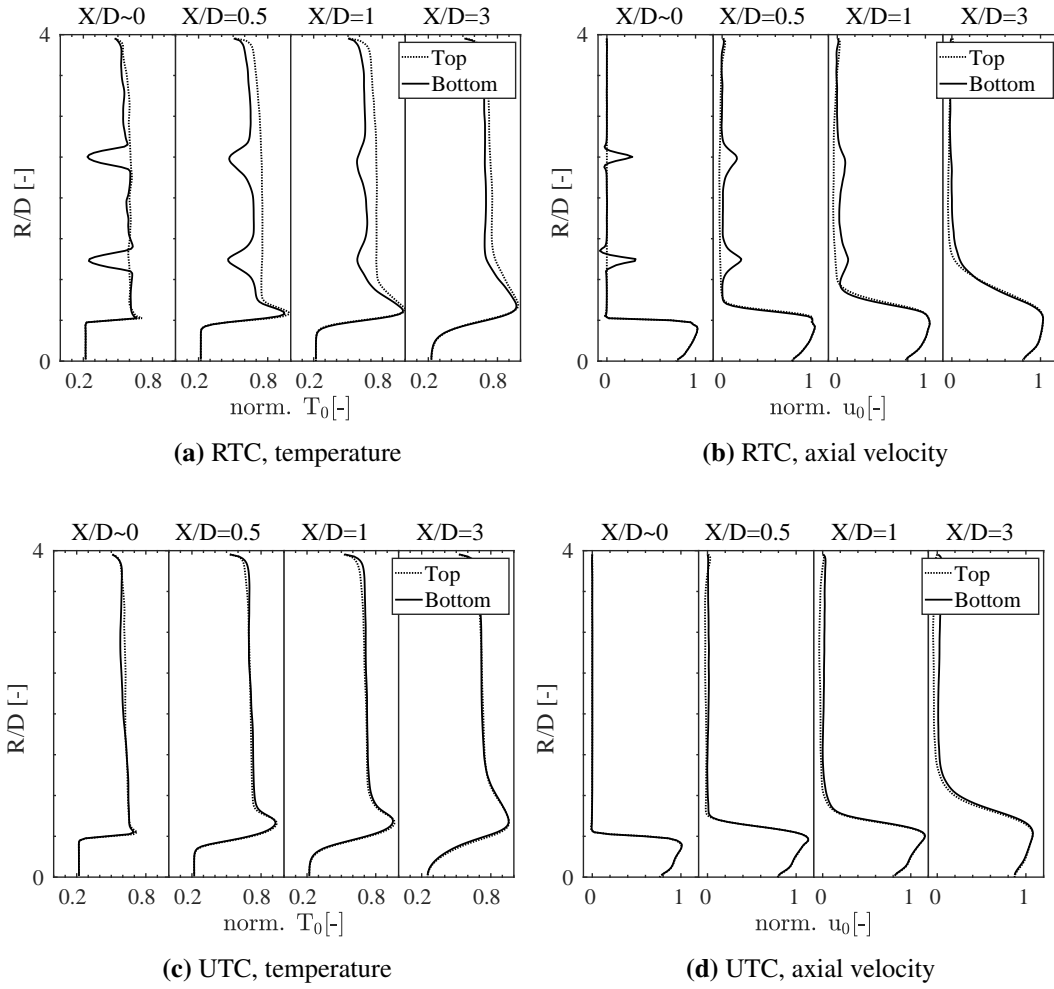


**Fig. 7.19** Time averaged temperature and axial velocity over the chamber radius. The axial velocity was normalized by 130 m/s and the temperature by 2150 K.

which the pressure oscillates spatially in phase. Furthermore, this figure shows the normalized contribution from the density oscillations  $\dot{Q}_\rho$ , laminar flame speed oscillations  $\dot{Q}_{Sl}$ , fuel mass fraction oscillations  $\dot{Q}_{fi}$  and flame surface oscillations  $\dot{Q}_A$  to global heat release rate.

In this work, phase averaging was performed for the last 100 ms of the signal with a repetition frequency of 3050 Hz using 8 sampling points. This corresponds to 50 high-frequency oscillations. For both configurations a comparable quantitative behavior of the oscillations was observed. It can be seen that the density and flame surface oscillate almost in phase with the pressure and thus have a destabilizing effect. Oscillations in the laminar flame speed and equivalence ratio can be neglected. The density oscillations exhibit the highest amplitude and may be identified as the main driving mechanism. At this point, the reader should be warned that the use of the global heat release rate in the context of HFI must be done with care. For the case under investigation, this consideration was useful as the acoustic mode was radial and the flame was positioned at the

acoustic pressure anti-node. In contrast, for the case where the flame is positioned at the acoustic pressure node, the consideration of the global heat release rate is meaningless. In such a case, the amplitude of the oscillation of the global heat release rate is nearly zero and it oscillates twice as often as pressure oscillation. For the flame in the acoustic pressure node, however, the global heat release rate of half of the flame can be considered, as demonstrated in previous work [35]. Since the density oscillations are always present and are in phase with the pressure oscillations, such a mechanism needs to be eliminated by means other than classical time-delay methods. A mitigation method has been successfully tested (by simulation) by Sharifi et al. [159] for this type of thermoacoustic coupling. In order to avoid high-frequency instabilities, the cut-off frequency in the combustor was changed by forming the chamber conically (for the modified geometry refer to [159]). As a result, the acoustic mode downstream of the base plate was attenuated and the flame was not exposed to pressure fluctuations with high amplitudes. Thus, no sufficiently strong driving mechanism was developed.

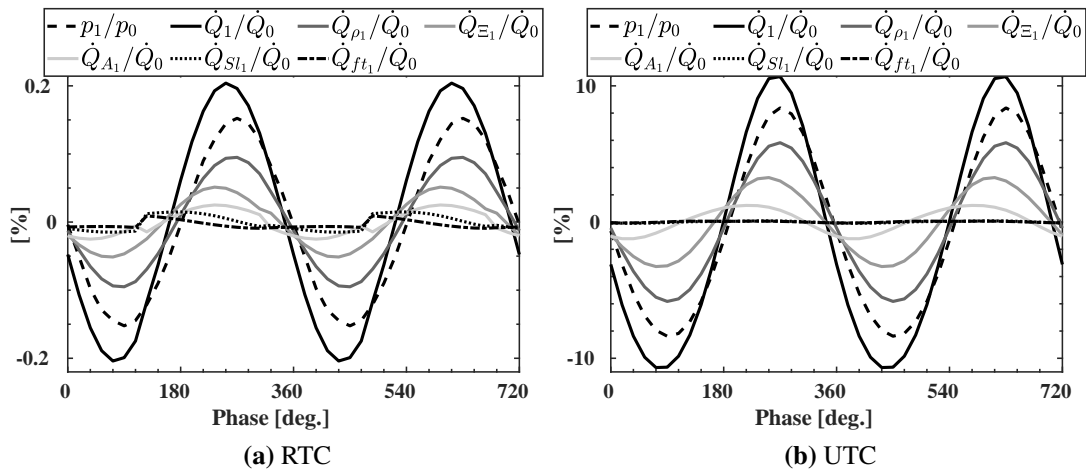


**Fig. 7.20** Phase-averaged normalized global heat release rate  $\dot{Q}_1$ , the contribution of density oscillations  $\dot{Q}_\rho$ , the contribution of wrinkling factor  $\dot{Q}_\Xi$ , the contribution of laminar flame speed  $\dot{Q}_{St}$ , the contribution of burning area oscillations  $\dot{Q}_A$  and the contribution of fuel mass fraction oscillations  $\dot{Q}_{ft}$  and volume averaged unsteady pressure  $p_1$ .

To identify the local position at which the heat release rate oscillations adds/ subtracts energy to/ from the acoustic field of the system, the spatial distribution of the Rayleigh indices are shown in Fig. 7.21. Additionally, the flame position is visualized by the iso-line of the regression variable  $\bar{b} = 0.5$ . The Rayleigh index field is characterized by the areas with positive and negative values, which are typical for the interaction of convective dynamics with the flame (e.g. interaction with vortices, pockets of lean and rich equivalence ratios). The significant difference in the Rayleigh index fields for the two configurations is that with UTC it is less distributed than with RTC, due to a shorter flame, and has more pronounced positive areas near the jet outlet. It should

be noted that the global Rayleigh index, which represents the spatial integral of these fields, is crucial for the thermoacoustic potential of the system. However, a comparison of the total Rayleigh index due to the different pressure amplitudes of both configurations is not meaningful. However, it is possible to illustrate the importance of each pathway by which the instabilities are caused by comparing the normalized contribution of density  $RI_\rho$ , laminar flame speed  $RI_{Sl}$ , wrinkling factor  $RI_\Xi$ , flame area  $RI_A$  and fuel mass fraction  $RI_{ft}$  in each configuration, as listed in table 7.3. It can be seen that the contribution of the density (deformations mechanism) with UTC is about 15 % more than with RTC, which is assumed to be due to the earlier mentioned difference in the flame length.

In the table 7.3, one can notice that the sum of the contributions of the different Rayleigh indices was not equivalent to the total Rayleigh index. The reason for this, however, needs further investigation. At this point we believe that the reason is due to the linearization and neglect of higher orders when deriving the different Rayleigh indices from the heat release. The total Rayleigh index, on the other hand, was calculated during the simulation run and considers any higher orders. To our best knowledge no other mechanisms were neglected for the cases considered. Both the mechanisms related to the global changes in heat release (e.g. density oscillation by  $RI_\rho$ ) and those related to local changes in heat release (e.g. displacement mechanism by  $RI_A$ ) were considered.

**Table 7.3** Normalized Rayleigh indices of different contributions.

| Configuration | $RI_\rho/RI$ | $RI_{Sl}/RI$ | $RI_\Xi/RI$ | $RI_A/RI$ | $RI_{ft}/RI$ |
|---------------|--------------|--------------|-------------|-----------|--------------|
| RTC           | 39.9         | 3.5          | 14.1        | 30.7      | 1.3          |
| UTC           | 52.8         | 0.2          | 23.6        | 12.2      | -0.1         |

## 7.4 Conclusion

The lack of suitable experiments is one of the main hurdles to study thermoacoustic instabilities at high-frequency. Based on earlier extensive numerical simulations, an experimentally feasible combustor was designed which was predicted to be susceptible to high-frequency instabilities. This paper experimentally investigates the combustor and shows that the system was able to exhibit the desired high-frequency instabilities with the first radial acoustic mode. The experiment revealed that the system tends to be most unstable at an equivalence ratio close to the stoichiometric condition. For richer and leaner mixtures, the amplitude of the high-frequency oscillations was decreased. It was also shown that an increase in mass flow rate generally led to a higher amplitude of high-frequency oscillations. In addition, the equivalence ratio at which the system

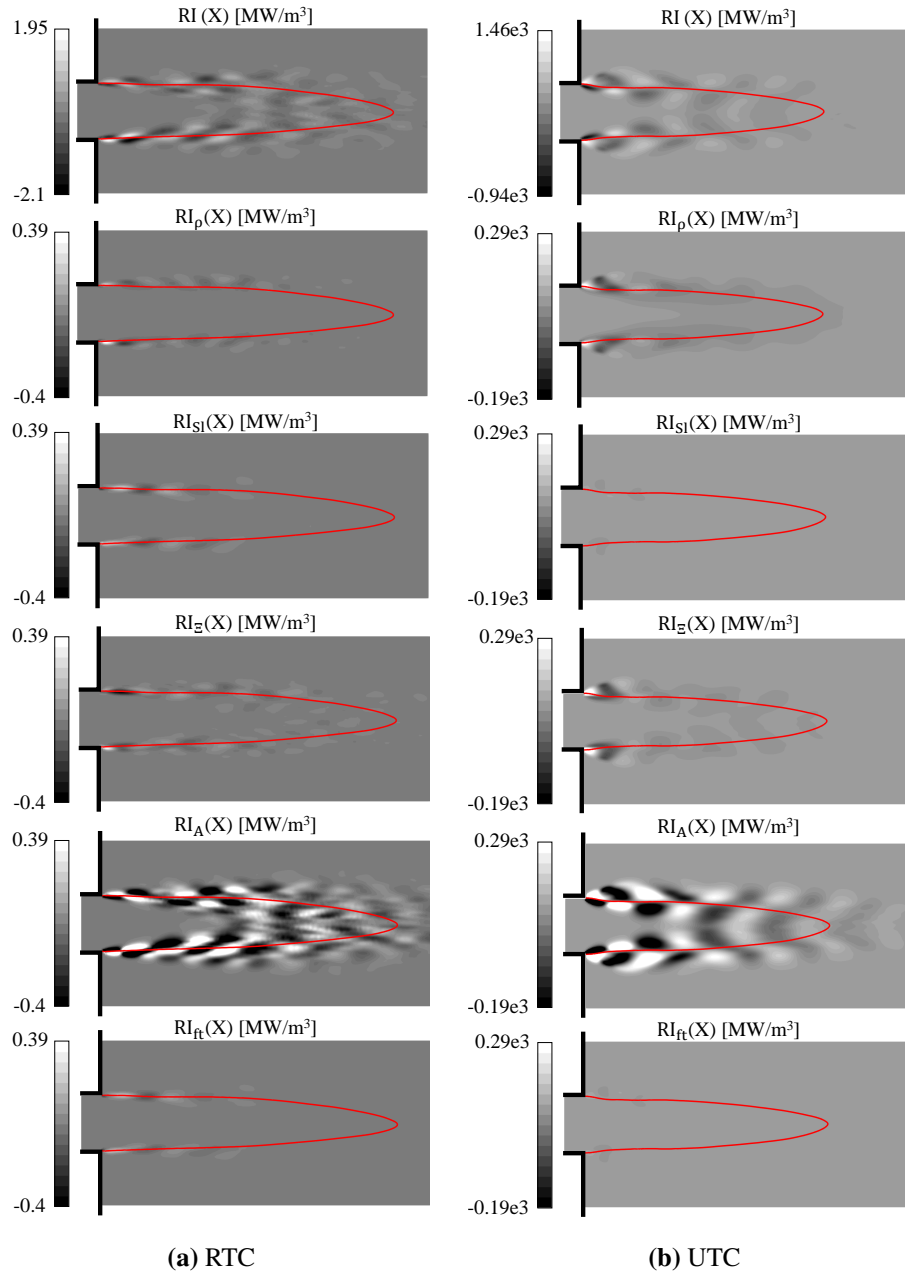


**Fig. 7.21** Comparison of fields of local Rayleigh indices for RTC and UTC.

was most unstable was shifted to the leaner mixture by increasing the mass flow rate. The experimental configuration was considered to demonstrate the ability of the LES framework to predict thermoacoustic instabilities. The comparison between experiment and simulation was performed in terms of thermoacoustic pressure amplitudes at a stable and an unstable operating point and showed a reasonably good agreement. To shed light on the decisive importance of the wall temperature for thermoacoustic simulations, an additional LES of the unstable operating point, assuming a uniform combustor wall temperature, was performed. It was found that in this configuration the amplitude of the high-frequency oscillations reached a value 60 times higher, by similar frequency and

mode shape. Evaluating the different contributions to the heat release oscillations and comparing their phases with the pressure oscillations, the most relevant mechanism of instability was identified to be the deformations mechanism. An experiment allowing optical access is planned for the future.

## Acknowledgments

The authors gratefully acknowledge the financial support of the state of North Rhine-Westphalia and the German Ministry of Economics and Technology for the collaborative project “Untersuchung der Entstehungsmechanismen zu Hochfrequenzinstabilitäten” of the Clean Energy Center stage 2 (project funding reference number 03ET7011L), as well as the computing time granted by the Center for Computational Sciences and Simulation of the University of Duisburg-Essen and provided on the supercomputer magnitUDE (Deutsche Forschungsgemeinschaft grant INST 20876/209-1 FUGG) at the Zentrum für Informations- und Mediendienste.

## CHAPTER 8

### Summery and outlook

This work dealt with the modeling of thermoacoustic instabilities and understanding its driving mechanism using Large Eddy Simulation (LES) and experimental analysis.

The major difficulty with investigating thermoacoustic instabilities is that there are hardly any suitable test cases available that can be used as a starting point for the analysis. Therefore, the main aim of this work was to develop a novel experimental lab-scale test case that was able to exhibit high-frequency thermoacoustic instabilities. The knowledge gained in the design phase and the test case itself can then serve as a basis for understanding the underlying mechanisms of thermoacoustics and its primary damping methods. Accordingly, some initial requirements for the experimental configuration have been stipulated. The test case required to be as simple as possible and the experiment as cost-effective as feasible. It had to show similarities to Siemens' modern gas turbine combustion chamber in terms of frequency of instabilities, aerodynamics and method of flame stabilization.

LES was performed for the design purpose of the test case. Combustion was described using the flame surface density (FSD) model. The numerical methods were tested and validated for the stationary state by comparing the LES results of the triple jet combustion chamber with measured data. Due to the lack of suitable experiments with high-frequency thermoacoustic instabilities, it was first assumed that the solver is capable of predicting flame's dynamics. However, the numerical method was validated in earlier work at Siemens for thermoacoustic instabilities in the intermediate frequency range.

In the first step, the few high-frequency thermoacoustic mechanisms known from literature were considered. To investigate whether these mechanisms contribute to the instabilities of the jet flames applied in the combustion chamber of modern gas turbines, a forced response study has been performed in a generic combustion chamber with similarities to the practical configuration.

By proper forcing from the non-reflecting side boundaries of the combustor it was possible to subject the flame to:

1. Pressure-forcing: an acoustic pressure anti-node (simultaneously acoustic veloc-

ity node)

2. Velocity-forcing: an acoustic velocity anti-node (simultaneously acoustic pressure node)

By comparing the Rayleigh index of the flame under the forcing scenarios, we were able to find out that flame at the pressure forcing was generally more susceptible to thermoacoustic instabilities. The influence of oscillation frequency on the flame was also investigated and found that the sensitivity of the flame to thermoacoustic instabilities decreased for higher forcing frequencies with pressure forcing, whereas the frequency impact was negligible for velocity forcing. The different pathway through which the heat release rate could oscillate under the forcing and their contribution to the Rayleigh index was calculated. With the pressure forcing, the density mechanism was determined to be the primary driving mechanism. With velocity forcing, the flame displacement was revealed to be the main driving mechanism. The influence of the flame length on the susceptibility of the flame to high-frequency thermoacoustic instabilities was investigated. A compact flame under pressure forcing was more susceptible, while a longer flame under velocity forcing tended to have a higher Rayleigh index.

Based on these observations and findings and considering the requirements of a cost-effective experiment, a generic atmospheric cylindrical combustion chamber was proposed. The susceptibility to high-frequency instabilities of the configuration was increased by placing the jet-stabilized flame centrally in the cylindrical combustion chamber to excite the radial acoustic eigenmodes of the combustion chamber. With a radial mode in the combustion chamber, the flame could be subjected to a pressure anti-node (velocity node) where the highest contribution to instabilities was ensured. The configuration could show acoustic and aerodynamic similarities with the technical combustion chamber by selecting the corresponding combustion chamber diameter and using a practical turbulence generator, and mixing channel whilst an extremely long flame was prevented.

The generic adiabatic premixed combustor was then simulated with different equivalence ratios to obtain high-frequency radial instabilities with high amplitude. It was found that the configuration was able to exhibit the first radial mode for a specific equivalence ratio ( $\phi = 0.7$ ). For lower and higher equivalence ratios, the instabilities were attenuated in the first radial mode. The results also showed that the flame was able to excite the second radial mode more strongly at a near stoichiometric condition for the adiabatic configuration.

A generic configuration with an operating condition based on the LES was designed and had to be adapted towards a feasible experiment. For this purpose, the effects of wall temperatures, technical mixing and acoustic transmission of the upstream and downstream boundary conditions were investigated.

It was observed that the higher the temperature of the combustion chamber wall, the larger the amplitude of high-frequency oscillations. LES of the generic configuration with the equivalence ratio of 0.7 and a realistic wall temperature of 1100 K led to complete elimination of the acoustic instabilities. The change in the cut-off frequency most likely caused this behavior. By changing the temperature distributions in the chamber, the amplitudes of pressure oscillations in the axial direction were attenuated, so that not the entire length of the flame was subjected to pressure oscillations with high amplitude, as was the case with the adiabatic configuration. This reduced the coupling potential of the flame and led to a less unstable (more stable) combustion when the cooling of combustion chamber walls was considered. Further investigation showed, that it was possible to recover the instabilities with the cooled wall by increasing the equivalence ratio to 0.9.

The consideration of the technical mixing in the configuration led to a greater amplitude of instabilities at almost the same frequency. The system showed pockets of rich and lean mixture generated with the frequency of instabilities and transported downstream while interacting with the flame. The resulting oscillation of the heat release rate due to the oscillation of the local equivalence ratios was in phase with the pressure, evidencing its destabilizing effect.

Since the numerical inlet boundary condition used in the generic configuration was completely reflective, the influence of the change in the acoustic transmittance of this boundary on the instabilities was investigated. It was found that if this part of the configuration was acoustically open, no instabilities were observed. The instabilities could be restored by a new plenum concept, which was acoustically almost closed. Thus, a configuration susceptible to high-frequency instabilities was developed which met the experimental requirements.

The configuration was set up and tested in the Siemens experimental laboratory. Acoustic measurements were performed to verify the occurrence of predicted first radial thermoacoustic instabilities. Experiments were performed for different equivalence ratios and mass flows with preheated air. The system showed the desired instabilities as soon as a certain equivalence ratio was exceeded. The amplitude of the instabilities increased with increasing equivalence ratio and reached its maximum at a slightly lean equivalence ratio. As the equivalence ratio was further increased, the amplitude of the high-frequency instabilities decreased. The maximum amplitude of the instabilities shifted with the rise of the combustion air mass flow rate toward the leaner mixture. It was also found that an increase in combustion mass flow rate increased the tendency of the system to be unstable.

For the final evaluation of the numerical method, two operating conditions were chosen, one assigned to a thermoacoustically stable combustion and the other to an unstable combustion. For these simulations, an attempt was made to set a realistic

wall temperature. For this purpose, the combustion chamber wall was divided into several sections for which the measured temperatures were set. The main difference between these simulations and the a priori simulations in the design phase was the wall treatment. The LES results were compared with the measurement data and overall a reasonable agreement could be demonstrated. Thus it was proven that LES was able to predict high-frequency instabilities.

The instabilities observed in the experiment had the desired frequency, but showed lower amplitudes than expected by the simulations in the design phase. To investigate the reason for this deviation, a further simulation of the experimental configuration was performed. In this simulation, a uniform combustion chamber wall temperature was assumed. The temperature was calculated by averaging the measured combustor wall temperatures obtained in the experiment. A comparison of the result of this simulation with the results of the simulation considering realistic combustor wall temperatures showed a significant increase in the amplitude of the high-frequency instabilities when a uniform mean combustor wall temperature was assumed, which emphasizes the importance of wall heat treatment in the simulation of thermoacoustic instabilities.

In this work, in addition to design of an thermoacoustically unstable combustor in high-frequency range, a method for suppressing the observed thermoacoustic instabilities was proposed. The suppression method was proposed in accordance with the obtained evidence on the damping effect of the combustion chamber wall cooling on the instabilities. It was observed that cooling the combustor wall resulted in a positive area-averaged temperature gradient along the longitudinal axis of the combustor. This temperature change resulted in an increase in the cut-off frequency of the combustor along its axis. In analogy, it was proposed to alter the cut-off frequency of the combustor by changing the diameter of the combustor. A conical combustor was designed whose radius was decreased along its axis, leading to an increase in the cut-off frequency along the longitudinal axis. LES showed that the system was stable under this modification of the combustor, proving that the conical combustor design can be considered as a damping method for high-frequency instabilities with radial modes. However, in order to make a general statement, further evidence and further investigations are required.

This work showed that LES was able to predict the occurrence of instabilities at high frequencies. The combustion chamber successfully designed by LES has the potential to be used in more sophisticated experiments in the future. However, it should be noted that both the value of the wall temperature and its non-uniformity are crucial to the occurrence of instability in the system.

# Appendices



## Appendix A

### Validation of the Combustion Model

*This chapter including all figures and tables was previously published in AIAA Journal, 57(1), V. Sharifi, C. Beck and A. M. Kempf, Large-Eddy Simulation of Acoustic Flame Response to High-Frequency Transverse Excitations [35]. The author V. Sharifi ran all simulations, wrote the paper and generated all figures and tables. The authors C. Beck and A. M. Kempf contributed corrections, discussions and proofreading.*

To validate the combustion model used for this study, for a flame that is very similar to the case examined, the experimental data from high pressure (8 bar) triple-jet combustor [179] is used. Figure A.1 shows the setup of the combustor. The combustion chamber consists of a mixing section with six laterally arranged pipes followed by a flow distributor, the combustor and the exhaust passage. In the experiment, fuel (NG) is injected through the laterally arranged pipes in the mixer and the unmixedness of fuel and air at duct outlets is eliminated by (a) premixing fuel and air upstream of the combustor and (b) using the special manifold to distribute the mixture to all the three jets. The following measurements were performed in the experiment: 1D laser Raman scattering, OH\* chemiluminescence and particle image velocimetry in order to determine the mixture fraction and temperature, flame position and the planar velocity field. To reduce the complexity of the simulation and due to the fact that a good mixing was observed at the duct outlet in the experiment [179], the simulation is performed excluding the mixing procedure. However, in order to consider the turbulence generated by the radially arranged pipes, they are considered in the simulation as illustrated in Fig. A.1. The mixture of the fuel and air was injected through the inlet with a temperature of 673 K. Hence, the natural gas composition used in the experiment consist mainly of methane (94.2% to 98.7%), pure methane is assumed for the simulation. At the inlet, velocity fluctuations with an intensity of 1 % and a length scale of 3 % of the inlet duct are added to the flow to ensure the generation of the eddies over laterally arranged pipes in the simulation. The combustor side walls were cooled in the experiment. The exact temperature of the combustor side walls is not known from the experiment. Lammel et al. [179] assumed that the temperature of the combustor side walls is between 920 K - 1200 K. For the simulation, the side walls temperature is set to an estimated value of

1100 K. The temperature of the base plate and exhaust gas nozzle are set to 600 K and 572 K, respectively as it is known from experiment. All the other walls are assumed to be adiabatic in the simulation. The combustor is discretized using 1 mm cells, which corresponds to 20 cells over jet diameter. The computational grid contains 7.6 millions cells. The value of  $C$ , the coefficient for the wrinkling model (see eq. 5.5), is set to 0.5. Table A.1 gives an overview of the boundary conditions used for this simulation. The normalized field of methane concentration from the experiment is compared with

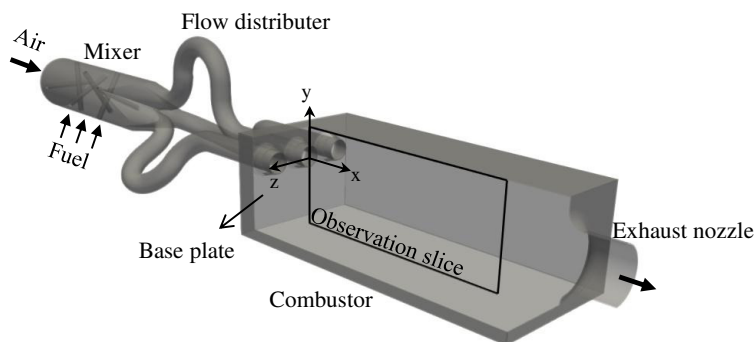


**Fig. A.1** Computational domain of the triple jet.

the field of the mean regress variable from the simulation in Fig. A.2. The data was sampled on a cutting plane through the axis of the middle jet, as illustrated in Fig. A.1. Line-Raman provide a set of independent data points. The contour of methane concentration was generated by interpolating the Raman experimental data, sampled at the locations indicated by black dots in Fig. A.2(left). To compare the flame length and

**Table A.1** Boundary condition for the validation case

| $fuel$ | $\dot{m}$ , $kg\ s^{-1}$ | $p$ , kPa | $T_{in}$ , K | $\phi$ , - | $T(side\ walls)$ , K | $T(exhaust\ walls)$ , K |
|--------|--------------------------|-----------|--------------|------------|----------------------|-------------------------|
| $CH_4$ | 0.487                    | 804       | 673          | 0.66       | 1100                 | 572                     |

the thickness of the flame brush the normalized  $CO_2$  concentration is compared with the mean progress variable. The data is sampled over the axis of the jet and over a transverse line three jet diameters downstream of the duct outlet and are shown in Fig. A.3a and A.3b. The flame length is predicted by simulation is in a good agreement with the experiment. The flame brush is however slightly underpredicted. The velocities measured in the experiment are compared against the results of the simulation and are shown in Fig. A.3c and A.3d. The mean axial velocity and its rms-value show a good agreement with the experiment.

In the topic of forced response simulation, Krediet et al. [63] used the flame surface density based combustion model, used in the present study, to validate the identification of the Flame Describing Function (fdf) [180] using Large Eddy simulation in a

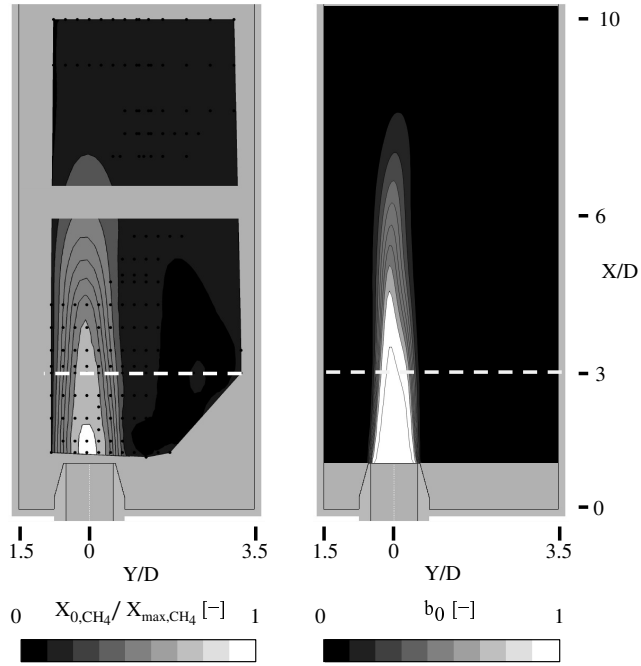


**Fig. A.2** Normalized field of methane concentration from the experiment (left) and the normalized field of regress variable from CFD (right).

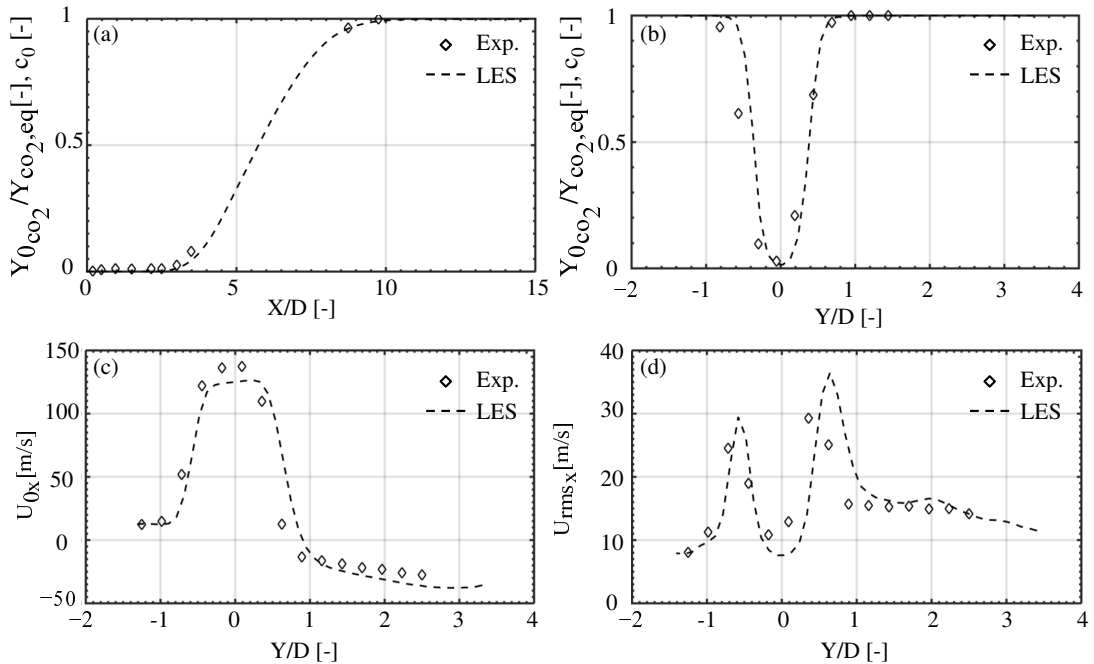


**Fig. A.3** Mean normalized progress variable and velocity statistics along center-line and a transverse line three jet diameter downstream of the duct outlet.

frequency range from 60 to 320 Hz. They used the experimental data from an atmospheric swirl-stabilized premixed flame. To calculate the FDF they set the flame under harmonic excitation at six distinct frequencies. The excitation is generated in the same manner as used in this paper. They superimposed harmonic acoustic waves on the ve-

locity at the inlet. It was shown that the calculated data are in good agreement with measurements. Thus, the combustion model used for the present study is validated for the forced response simulation at least in a low-frequency range.

## Appendix B

### Grid Refinement Study

This chapter including all figures and tables was previously published in *AIAA Journal*, 57(1), V. Sharifi, C. Beck and A. M. Kempf, *Large-Eddy Simulation of Acoustic Flame Response to High-Frequency Transverse Excitations* [35]. The author V. Sharifi ran all simulations, wrote the paper and generated all figures and tables. The authors C. Beck and A. M. Kempf contributed corrections, discussions and proofreading.

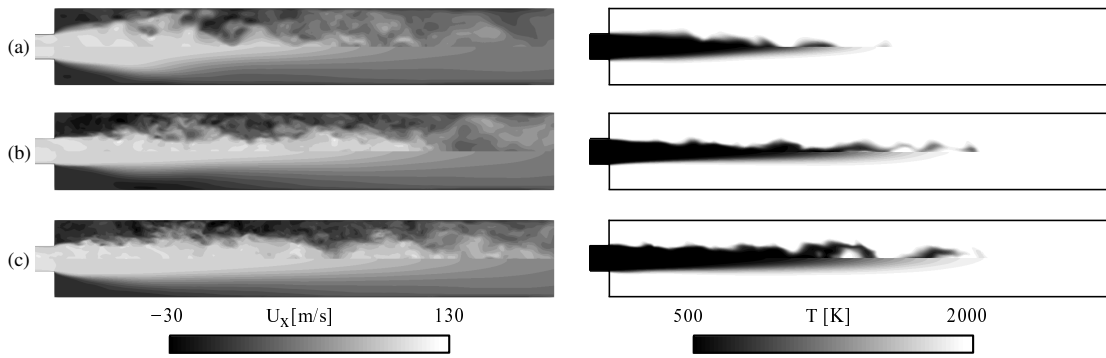


**Fig. B.1** Instantaneous (upper half) and time averaged (lower half) fields of the axial velocity (left) and the temperature (right) from the non-forced simulation for (a) coarse, (b) medium and (c) fine mesh.

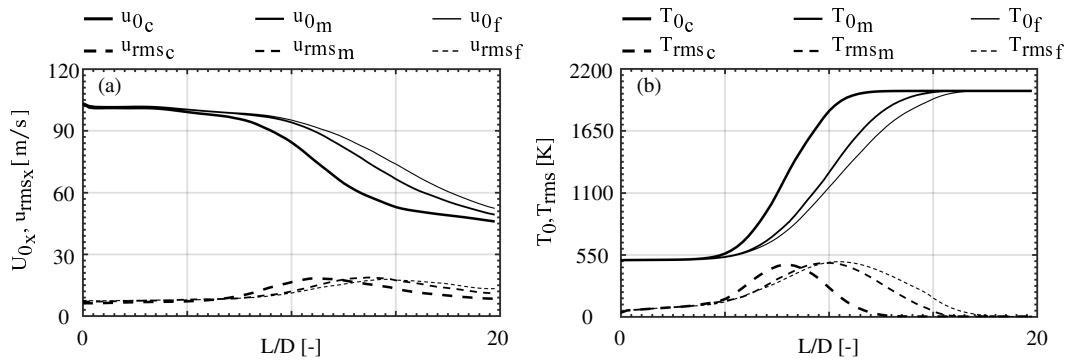


**Fig. B.2** Time averaged and rms-value of (a) axial velocity and (b) temperature along the center-line of the combustion chamber (coarse-c, medium-m, fine-f) obtained from the non-forced simulation.

A grid refinement study is conducted for the non-forced reference simulation using 1, 4 and 8 million cells corresponding to a cell size of 2, 1.33 and 1 mm, respectively. The geometry of the combustion chamber is shown in Fig. 5.2. The operating conditions used for this simulation are listed in table 5.2. The value of  $C$  (see eq. 5.5) is set to 0.5. The instantaneous and the mean field of the axial velocity and the temperature is shown in Fig. B.1, for the different mesh sizes. The flame is characterized by the strong shear layer between the high-speed jet flow and the low-speed surrounding exhaust gas in the chamber. The flame is stabilized by the outer recirculation zone and is attached at the duct outlet. As expected, with the coarse mesh less fluctuations are resolved and thus the jet appears to remain laminar up to about two jet diameters downstream of the duct outlet. The mean temperature and axial velocity and the corresponding rms-value along the center-line of the combustion chamber from the duct outlet are plotted in Fig. B.2, for all the mesh resolutions used here. The fluctuation at the duct outlet are similar in all three cases. It is shown that the flame length increased with decreasing mesh sizes. The flame length, defined as the distance between the duct outlet and the position where the mean regress variable equals 0.5 on the center-line, decreased about 20 % for the coarse mesh compared to the medium mesh, and by 8 % for the medium mesh compared to the fine mesh. Despite an absence of experimental data for this case, we assume that the flame length predicted from the simulation with the fine mesh is the most accurate one. Furthermore, the results from the medium and fine mesh are considered to have a reasonable agreement, despite the maximum deviation of 8 % in flame length. Therefore and as a compromise with computational costs, we chose to use the medium mesh for the study.

## REFERENCES

- [1] I.E. Agency, *World Energy Outlook 2019* (OECD, 2019). doi:[10.1787/caf32f3b-en](https://doi.org/10.1787/caf32f3b-en)
- [2] T. Boningari, P.G. Smirniotis, *Curr. Opin. Chem. Eng.* **13**, 133 (2016). doi:[10.1016/j.coche.2016.09.004](https://doi.org/10.1016/j.coche.2016.09.004)
- [3] G.E. Andrews, in *Modern gas turbine systems* (2013), pp. 715–790. doi:[10.1533/9780857096067.3.715](https://doi.org/10.1533/9780857096067.3.715)
- [4] W. Krebs, P. Flohr, B. Prade, S. Hoffmann, *Combust. Sci. Technol* **174**(7), 99 (2002). doi:[10.1080/713713051](https://doi.org/10.1080/713713051)
- [5] C. Lechner, J. Seume, *Stationäre gasturbinen* (Springer-Verlag, 2018)
- [6] M.P. Boyce, *Gas turbine engineering handbook* (2011). doi:[10.1016/C2009-0-64242-2](https://doi.org/10.1016/C2009-0-64242-2)
- [7] J. O'Connor, V. Acharya, T. Lieuwen, *Prog. Energy Combust. Sci.* **49**, 1 (2015). doi:[10.1016/j.pecs.2015.01.001](https://doi.org/10.1016/j.pecs.2015.01.001)
- [8] S.M. Candel, in *Proc. Combust. Inst.*, vol. 24 (1992), vol. 24, pp. 1277–1296. doi:[10.1016/S0082-0784\(06\)80150-5](https://doi.org/10.1016/S0082-0784(06)80150-5)
- [9] W. Krebs, S. Bethke, J. Lepers, P. Flohr, B. Prade, C. Johnson, S. Sattinger, *AIAA* **210**, 89 (2005). doi:[10.2514/4.866807](https://doi.org/10.2514/4.866807)
- [10] B. Ćosić, T.G. Reichel, C.O. Paschereit, *J. Eng. Gas Turbines Power* **134**(10), 101503 (2012). doi:[10.1115/1.4007024](https://doi.org/10.1115/1.4007024)
- [11] H. Mongia, T. Held, G. Hsiao, R. Pandalai, *Combustion instabilities in gas turbine engines* (2005). doi:[10.2514/5.9781600866807.0043.0063](https://doi.org/10.2514/5.9781600866807.0043.0063)
- [12] P. Berenbrink, S. Hoffmann, in *ASME Turbo Expo* (2000), pp. V002T02A001–V002T02A001. doi:[10.1115/2000-GT-0079](https://doi.org/10.1115/2000-GT-0079)
- [13] J.W.S. Rayleigh, *Nature* **18**(455), 319 (1878). doi:[10.1038/018319a0](https://doi.org/10.1038/018319a0)

- [14] D. Durox, T. Schuller, N. Noiray, A.L. Birbaud, S. Candel, *Combust. Flame* **156**(1), 106 (2009). doi:[10.1016/j.combustflame.2008.07.016](https://doi.org/10.1016/j.combustflame.2008.07.016)
- [15] J.B. Sewell, P.A. Sobieski, *Combustion Instabilities in Gas Turbine Engines* **210**, 147 (2005). doi:[10.2514/5.9781600866807.0029.0041](https://doi.org/10.2514/5.9781600866807.0029.0041)
- [16] P. Rijke, *Annalen der Physik* **183**(6), 339 (1859). doi:[10.1002/andp.18591830616](https://doi.org/10.1002/andp.18591830616)
- [17] J.W.S. Rayleigh, *The theory of sound* (Dover, 1945)
- [18] A. Sjunnesson, P. Henrikson, C. Lofstrom, in *28th JPC* (1992), p. 3650. doi:[10.2514/6.1992-3650](https://doi.org/10.2514/6.1992-3650)
- [19] T.J. Poinot, A.C. Trouve, D.P. Veynante, S.M. Candel, E.J. Esposito, *J. Fluid Mech.* **177**, 265 (1987). doi:[10.1017/s0022112087000958](https://doi.org/10.1017/s0022112087000958)
- [20] D.E. Rogers, *J. Jet Propuls.* **26**(6), 456 (1956). doi:[10.1016/j.combustflame.2018.01.016](https://doi.org/10.1016/j.combustflame.2018.01.016)
- [21] J. Schwing, T. Sattelmayer, N. Noiray, in *ASME Turbo Expo* (2011), pp. 259–268. doi:[10.1115/gt2011-45246](https://doi.org/10.1115/gt2011-45246)
- [22] K. YU, A. Trouve, S. Candel, in *29th Aerospace Sciences Meeting* (1991), p. 367. doi:[10.2514/6.1991-367](https://doi.org/10.2514/6.1991-367)
- [23] K. Schadow, E. Gutmark, *Prog. Energy Combust. Sci.* **18**(2), 117 (1992). doi:[10.1016/0360-1285\(92\)90020-2](https://doi.org/10.1016/0360-1285(92)90020-2)
- [24] H.M. Altay, R.L. Speth, D.E. Hudgins, A.F. Ghoniem, *Combust. Flame* **156**(5), 1111 (2009). doi:[10.1016/j.combustflame.2009.02.003](https://doi.org/10.1016/j.combustflame.2009.02.003)
- [25] D. Durox, T. Schuller, S. Candel, *Proc. Combust. Inst.* **30**(2), 1717 (2005). doi:[10.1016/j.proci.2004.08.067](https://doi.org/10.1016/j.proci.2004.08.067)
- [26] T. Steinbacher, A. Albayrak, A. Ghani, W. Polifke, *Proc. Combust. Inst.* (2018). doi:[10.1016/j.proci.2018.07.041](https://doi.org/10.1016/j.proci.2018.07.041)
- [27] K. Venkataraman, L. Preston, D. Simons, B. Lee, J. Lee, D. Santavicca, *J. Propul. Power* **15**(6), 909 (1999). doi:[10.2514/2.5515](https://doi.org/10.2514/2.5515)
- [28] T. Lieuwen, H. Torres, C. Johnson, B.T. Zinn, in *ASME* (1999), pp. V002T02A001–V002T02A001. doi:[10.1115/99-GT-003](https://doi.org/10.1115/99-GT-003)
- [29] J. Lee, K. Kim, D. Santavicca, in *38th AIAA/ASME/SAE/ASEE Joint Propulsion Conference and Exhibit* (2002), p. 4015. doi:[10.2514/6.2002-4015](https://doi.org/10.2514/6.2002-4015)

- [30] B. Schuermans, V. Bellucci, F. Guethe, F. Meili, P. Flohr, C.O. Paschereit, in *ASME Turbo Expo* (2004), pp. 539–551. doi:[10.1115/gt2004-53831](https://doi.org/10.1115/gt2004-53831)
- [31] J.H. Cho, T. Lieuwen, *Combust. Flame* **140**(1-2), 116 (2005). doi:[10.1016/j.combustflame.2004.10.008](https://doi.org/10.1016/j.combustflame.2004.10.008)
- [32] R. Riazi, M. Farshchi, *Scientia Iranica* **18**(4), 913 (2011). doi:[10.1016/j.scient.2011.07.002](https://doi.org/10.1016/j.scient.2011.07.002)
- [33] L. Hakim, T. Schmitt, S. Ducruix, S. Candel, *Combust. Flame* **162**(10), 3482 (2015). doi:[10.1016/j.combustflame.2015.05.022](https://doi.org/10.1016/j.combustflame.2015.05.022)
- [34] M. Zellhuber, J. Schwing, B. Schuermans, T. Sattelmayer, W. Polifke, *Int. J. Spray Combust.* **6**(1), 1 (2014). doi:[10.1260/1756-8277.6.1.1](https://doi.org/10.1260/1756-8277.6.1.1)
- [35] V. Sharifi, A. Kempf, C. Beck, *AIAA J.* **57**(1), 327 (2018). doi:[10.2514/1.J056818](https://doi.org/10.2514/1.J056818)
- [36] H. Schmidt, C. Jimenez, *Combust. Flame* **157**(8), 1610 (2010). doi:[10.1016/j.combustflame.2010.03.010](https://doi.org/10.1016/j.combustflame.2010.03.010)
- [37] G. Beardsell, G. Blanquart, *Proc. Combust. Inst.* (2018). doi:[10.1016/j.proci.2018.07.125](https://doi.org/10.1016/j.proci.2018.07.125)
- [38] S. Shreekrishna, T. Lieuwen, in *15th AIAA/CEAS Aeroacoustics Conference* (2009), p. 3261. doi:[10.2514/6.2009-3261](https://doi.org/10.2514/6.2009-3261)
- [39] S. Osher, J.A. Sethian, *J. Comput. Physik* **79**(1), 12 (1988). doi:[10.1016/0021-9991\(88\)90002-2](https://doi.org/10.1016/0021-9991(88)90002-2)
- [40] G.H. Markstein, *Nonsteady Flame Propagation* (Pergamon Press, Oxford, 1964). doi:[10.1016/c2013-0-07744-4](https://doi.org/10.1016/c2013-0-07744-4)
- [41] C. Law, C. Sung, *Prog. Energy Combust. Sci.* **26**(4-6), 459 (2000). doi:[10.1016/S0360-1285\(00\)00018-6](https://doi.org/10.1016/S0360-1285(00)00018-6)
- [42] H. Wang, C. Law, T. Lieuwen, *Combust. Flame* **156**(4), 889 (2009). doi:[10.2514/6.2007-176](https://doi.org/10.2514/6.2007-176)
- [43] A. Orchini, M.P. Juniper, *Combust. Flame* **165**, 97 (2016). doi:[10.1016/j.combustflame.2015.10.011](https://doi.org/10.1016/j.combustflame.2015.10.011)
- [44] J. Schwing, F. Grimm, T. Sattelmayer, in *ASME Turbo Expo* (2012), pp. 553–566. doi:[10.1115/GT2012-68775](https://doi.org/10.1115/GT2012-68775)

- [45] J. Schwing, T. Sattelmayer, in *ASME Turbo Expo* (2013), pp. V01AT04A003–V01AT04A003. doi:[10.1115/gt2013-94064](https://doi.org/10.1115/gt2013-94064)
- [46] T. Hummel, F. Berger, M. Hertweck, B. Schuermans, T. Sattelmayer, *J. Eng. Gas Turbines Power* **139**(7), 071502 (2017). doi:[10.1115/1.4035592](https://doi.org/10.1115/1.4035592)
- [47] F.M. Berger, T. Hummel, M. Hertweck, J. Kaufmann, B. Schuermans, T. Sattelmayer, *J. Eng. Gas Turbines Power*. **139**(7), 071501 (2017). doi:[10.1115/1.4035591](https://doi.org/10.1115/1.4035591)
- [48] F. Lespinasse, F. Baillet, T. Boushaki, *Comptes Rendus Mécanique* **341**(1-2), 110 (2013). doi:[10.1016/j.crme.2012.10.015](https://doi.org/10.1016/j.crme.2012.10.015)
- [49] Y. Méry, L. Hakim, P. Scoufflaire, L. Vingert, S. Ducruix, S. Candel, *Comptes Rendus Mécanique* **341**(1-2), 100 (2013). doi:[10.1016/j.crme.2012.10.013](https://doi.org/10.1016/j.crme.2012.10.013)
- [50] A. Sjunnesson, S. Olovsson, B. Sjoblom, in *International Symposium on Air Breathing Engines* (1991), pp. 385–393
- [51] J. Sangl, C. Mayer, T. Sattelmayer, *J. Propul. Power* **133**(7), 071501 (2011). doi:[10.1115/1.4002659](https://doi.org/10.1115/1.4002659)
- [52] T. Buschhagen, R. Gejji, J. Philo, L. Tran, J.E.P. Bilbao, C.D. Slabaugh, *Proc. Combust. Inst.* (2018). doi:[10.1016/j.proci.2018.07.086](https://doi.org/10.1016/j.proci.2018.07.086)
- [53] T. Buschhagen, R. Gejji, J. Philo, L. Tran, J.E.P. Bilbao, C.D. Slabaugh, *J. Eng. Gas Turbines Power*. **140**(11), 111503 (2018). doi:[10.1115/1.4039760](https://doi.org/10.1115/1.4039760)
- [54] P. Wolf, G. Staffelbach, L.Y. Gicquel, J.D. Müller, T. Poinsot, *Combust. Flame* **159**(11), 3398 (2012). doi:[10.1016/j.combustflame.2012.06.016](https://doi.org/10.1016/j.combustflame.2012.06.016)
- [55] L. Hakim, A. Ruiz, T. Schmitt, M. Boileau, G. Staffelbach, S. Ducruix, B. Cuenot, S. Candel, *Proc. Combust. Inst.* **35**(2), 1461 (2015). doi:[10.1016/j.proci.2014.05.142](https://doi.org/10.1016/j.proci.2014.05.142)
- [56] C.Y. Lee, L.K.B. Li, M.P. Juniper, R.S. Cant, *Combust. Theory Model* **20**(1), 131 (2016). doi:[10.1080/13647830.2015.1118555](https://doi.org/10.1080/13647830.2015.1118555)
- [57] A. Ghani, T. Poinsot, L. Gicquel, G. Staffelbach, *Combust. Flame* **162**(11), 4075 (2015). doi:[10.1016/j.combustflame.2015.08.024](https://doi.org/10.1016/j.combustflame.2015.08.024)
- [58] A. Ghani, M. Miguel-Brebion, L. Selle, F. Duchaine, T. Poinsot, in *Summer Program* (2016), pp. 133–142

- [59] C.Y. Lee, S. Cant, *Combust. Theory Model* **21**(4), 722 (2017). doi:[10.1080/13647830.2017.1293849](https://doi.org/10.1080/13647830.2017.1293849)
- [60] F. Nicoud, H.B. Toda, O. Cabrit, S. Bose, J. Lee, *Phys. Fluids* **23**(8), 085106 (2011). doi:[10.1063/1.3623274](https://doi.org/10.1063/1.3623274)
- [61] G. Jourdain, L.E. Eriksson, in *ASME Turbo Expo* (2010), pp. 269–278. doi:[10.1115/GT2010-22339](https://doi.org/10.1115/GT2010-22339)
- [62] B. Schuermans, F. Guethe, D. Pennell, D. Guyot, C.O. Paschereit, *J. Eng. Gas Turbines Power*. **132**(11), 111503 (2010). doi:[10.1115/gt2009-59605](https://doi.org/10.1115/gt2009-59605)
- [63] H. Krediet, C. Beck, W. Krebs, J. Kok, *Proc. Combust. Inst.* **34**(1), 1223 (2013). doi:[10.1016/j.proci.2012.06.140](https://doi.org/10.1016/j.proci.2012.06.140)
- [64] T. Poinso, D. Veynante, *Theoretical and numerical combustion* (RT Edwards, Inc., 2005)
- [65] W. Polifke, A. Poncet, C. Paschereit, K. Döbbling, *J. Sound Vib.* **245**(3), 483 (2001). doi:[10.1006/jsvi.2001.3594](https://doi.org/10.1006/jsvi.2001.3594)
- [66] U. Krüger, J. Hüren, S. Hoffmann, W. Krebs, P. Flohr, D. Bohn, in *ASME Turbo Expo* (2000), pp. V002T02A015–V002T02A015. doi:[10.1115/1.1374437](https://doi.org/10.1115/1.1374437)
- [67] K.T. Kim, H.J. Lee, J.G. Lee, B. Quay, D. Santavicca, in *ASME Turbo Expo* (2009). doi:[10.1115/GT2009-60026](https://doi.org/10.1115/GT2009-60026)
- [68] M. Schulze, T. Hummel, N. Klarmann, F. Berger, B. Schuermans, T. Sattelmayer, *J. Eng. Gas Turbines Power*. **139**(3), 031510 (2017). doi:[10.1115/gt2016-57818](https://doi.org/10.1115/gt2016-57818)
- [69] T. Hummel, C. Temmler, B. Schuermans, T. Sattelmayer, *J. Eng. Gas Turbines Power* **138**(5), 051502 (2016). doi:[10.1115/1.4031542](https://doi.org/10.1115/1.4031542)
- [70] S.K. Thumuluru, T. Lieuwen, *Proc. Combust. Inst.* **32**(2), 2893 (2009). doi:[10.1016/j.proci.2008.05.037](https://doi.org/10.1016/j.proci.2008.05.037)
- [71] W. Sutherland, *Philos. Mag.* **36**(223), 507 (1893). doi:[10.1080/14786449308620508](https://doi.org/10.1080/14786449308620508)
- [72] E.W. Woolard, *Monthly Weather Review* **50**(2), 72 (1922). doi:[10.1017/cbo9780511618291.001](https://doi.org/10.1017/cbo9780511618291.001)
- [73] S.B. Pope, S.B. Pope, *Turbulent flows* (IOP Publishing, 2000)

- [74] H. Tennekes, J.L. Lumley, J. Lumley, et al., *A first course in turbulence* (MIT press, 1972)
- [75] N. Peters, *Turbulent combustion* (Elsevier, 2000). doi:[10.1016/c2009-0-64242-2](https://doi.org/10.1016/c2009-0-64242-2)
- [76] D. Dunn-Rankin, *Lean combustion: technology and control* (Academic Press, 2011)
- [77] G.P. Smith, D.M. Golden, M. Frenklach, N.W. Moriarty, B. Eiteneer, M. Goldenberg, C.T. Bowman, R.K. Hanson, S. Song, W. Gardiner Jr, et al., URL [http://www. me. berkeley. edu/gri\\_mech](http://www.me.berkeley.edu/gri_mech) (2011)
- [78] J. Warnatz, U. Maas, R.W. Dibble, J. Warnatz, *Combustion*, vol. 3 (Springer, 1996)
- [79] N. Sikalo, O. Hasemann, C. Schulz, A. Kempf, I. Wlokas, *Int. J. Chem. Kinet.* **46**(1), 41 (2014). doi:[10.1002/kin.20826](https://doi.org/10.1002/kin.20826)
- [80] A. Massias, D. Diamantis, E. Mastorakos, D. Goussis, *Combust. Flame* **117**(4), 685 (1999). doi:[10.1016/s0010-2180\(98\)00132-1](https://doi.org/10.1016/s0010-2180(98)00132-1)
- [81] D.A. Goussis, U. Maas, in *Turbulent Combustion Modeling* (2011), pp. 193–220
- [82] J. Van Oijen, F. Lammers, L. De Goey, *Combust. Flame* **127**(3), 2124 (2001). doi:[10.1016/s0010-2180\(01\)00316-9](https://doi.org/10.1016/s0010-2180(01)00316-9)
- [83] T. Turányi, A.S. Tomlin, *Analysis of kinetic reaction mechanisms* (Springer, 2014). doi:[10.1007/978-3-662-44562-4](https://doi.org/10.1007/978-3-662-44562-4)
- [84] N. Sikalo, O. Hasemann, C. Schulz, A. Kempf, I. Wlokas, *Int. J. Chem. Kinet.* **47**(11), 695 (2015). doi:[10.1002/kin.20942](https://doi.org/10.1002/kin.20942)
- [85] D.B. Spalding. Some fundamentals of combustion (1955). doi:[10.1201/9781420039757.ch2](https://doi.org/10.1201/9781420039757.ch2)
- [86] A. Linan, F.A. Williams, (1993)
- [87] R. Borghi, in *Recent advances in the Aerospace Sciences* (1985), pp. 117–138
- [88] T.C. Lieuwen, *Unsteady combustor physics* (Cambridge University Press, 2012)
- [89] M.J. Crocker, *Handbook of acoustics* (John Wiley, 1998)

- [90] T.C. Lieuwen, V. Yang, *Combustion instabilities in gas turbine engines: operational experience, fundamental mechanisms, and modeling* (American Institute of Aeronautics and Astronautics, 2005). doi:[10.2514/5.9781600866807.0029.0041](https://doi.org/10.2514/5.9781600866807.0029.0041)
- [91] W. Krebs, H. Krediet, E. Portillo, S. Hermeth, T. Poinso, S. Schimek, O. Paschereit, *J. Eng. Gas Turbines Power* **135**(8), 081503 (2013). doi:[10.1115/1.4023887](https://doi.org/10.1115/1.4023887)
- [92] W. Lang, T. Poinso, S. CANDEL, E. ESPOSITO, in *23rd Joint Propulsion Conference* (1987), p. 1876. doi:[10.2514/3.23108](https://doi.org/10.2514/3.23108)
- [93] R. Balachandran, B. Ayoola, C. Kaminski, A. Dowling, E. Mastorakos, *Combustion and Flame* **143**(1-2), 37 (2005)
- [94] G.D. Smith, *Numerical solution of partial differential equations: finite difference methods* (Oxford university press, 1985)
- [95] E. Courtine, L. Selle, T. Poinso, *Combust. Flame* **162**(11), 4331 (2015). doi:[10.1016/j.combustflame.2015.07.002](https://doi.org/10.1016/j.combustflame.2015.07.002)
- [96] A. Leonard, in *Advances in geophysics*, vol. 18 (Elsevier, 1975), pp. 237–248. doi:[10.1016/S0065-2687\(08\)60464-1](https://doi.org/10.1016/S0065-2687(08)60464-1)
- [97] A. Yoshizawa, *Phys. Fluids* **29**(7), 2152 (1986). doi:[10.1063/1.865552](https://doi.org/10.1063/1.865552)
- [98] W.W. Kim, S. Menon, in *33rd Aerospace Sciences Meeting and Exhibit* (1995), p. 356. doi:[10.2514/6.1995-356](https://doi.org/10.2514/6.1995-356)
- [99] S. Huang, Q. Li, *Int. J. Numer. Methods Fluids* **81**(7), 835 (2010). doi:[10.1002/nme.2715](https://doi.org/10.1002/nme.2715)
- [100] D.G. Goodwin, H.K. Moffat, R.L. Speth, Caltech, Pasadena, CA (2009)
- [101] E. Hawkes, R. Cant, *Proc. Combust. Inst.* **28**(1), 51 (2000). doi:[10.1016/S0082-0784\(00\)80194-0](https://doi.org/10.1016/S0082-0784(00)80194-0)
- [102] H. Weller, G. Tabor, A. Gosman, C. Fureby, in *Symp. (Int.) Combust.*, vol. 27 (1998), vol. 27, pp. 899–907. doi:[10.1016/S0082-0784\(98\)80487-6](https://doi.org/10.1016/S0082-0784(98)80487-6)
- [103] T. Butler, P. O’rourke, in *Symp. (Int.) Combust.*, vol. 16 (1977), vol. 16, pp. 1503–1515. doi:[10.1016/S0082-0784\(77\)80432-3](https://doi.org/10.1016/S0082-0784(77)80432-3)
- [104] O. Colin, F. Ducros, D. Veynante, T. Poinso, *Phys. Fluids* **12**(7), 1843 (2000). doi:[10.1063/1.870436](https://doi.org/10.1063/1.870436)

- [105] F. Williams, in *The mathematics of combustion* (SIAM, 1985), pp. 97–131. doi:[10.1137/1.9781611971064.ch3](https://doi.org/10.1137/1.9781611971064.ch3)
- [106] H. Pitsch, Center for Turbulence Research Annual Research Briefs **4** (2002)
- [107] K. Bray, P.A. Libby, J. Moss, *Combust. Flame* **61**(1), 87 (1985). doi:[10.1016/0010-2180\(85\)90075-6](https://doi.org/10.1016/0010-2180(85)90075-6)
- [108] M. Boger, D. Veynante, H. Boughanem, A. Trouvé, in *Symp. (Int.) Combust.*, vol. 27 (1998), vol. 27, pp. 917–925. doi:[10.1016/S0082-0784\(98\)80489-X](https://doi.org/10.1016/S0082-0784(98)80489-X)
- [109] C. Fureby, *Proc. Combust. Inst.* **30**(1), 593 (2005). doi:[10.1016/j.proci.2004.08.068](https://doi.org/10.1016/j.proci.2004.08.068)
- [110] F. Charlette, C. Meneveau, D. Veynante, *Combust. Flame* **131**(1-2), 159 (2002). doi:[10.1016/S0010-2180\(02\)00400-5](https://doi.org/10.1016/S0010-2180(02)00400-5)
- [111] D. Bradley, in *Proc. Combust. Inst.*, vol. 24 (1992), vol. 24, pp. 247–262. doi:[10.1016/S0082-0784\(06\)80034-2](https://doi.org/10.1016/S0082-0784(06)80034-2)
- [112] S. Dederichs, N. Zarzalis, C. Beck, in *ASME Turbo Expo 2015* (2015), pp. V04BT04A037–V04BT04A037. doi:[10.1115/GT2015-43502](https://doi.org/10.1115/GT2015-43502)
- [113] D.G. Goodwin, California Institute of Technology (2009)
- [114] J.H. Ferziger, M. Peric, *Computational methods for fluid dynamics* (Springer, 2012)
- [115] S. Patankar, *Numerical heat transfer and fluid flow* (CRC press, 1980)
- [116] H. Jasak, Error analysis and estimation for the finite volume method with applications to fluid flows. Ph.D. thesis, Imperial College London (1996)
- [117] P.K. Sweby, *SIAM journal on numerical analysis* **21**(5), 995 (1984). doi:[10.1137/0721062](https://doi.org/10.1137/0721062)
- [118] A. Harten, *J. Comput. Phys.* **49**(3), 357 (1983). doi:[10.1016/0021-9991\(83\)90136-5](https://doi.org/10.1016/0021-9991(83)90136-5)
- [119] H. Versteeg, W. Malalasekera, *The finite volume method* (1995)
- [120] H. Jasak, H. Weller, A. Gosman, *Int. J. Numer. Methods Fluids* **31**(2), 431 (1999). doi:[10.1002/\(SICI\)1097-0363\(19990930\)31:2<431::AID-FLD884>3.0.CO;2-T](https://doi.org/10.1002/(SICI)1097-0363(19990930)31:2<431::AID-FLD884>3.0.CO;2-T)

- [121] D. Zhang, C. Jiang, D. Liang, L. Cheng, *J. Comput. Phys.* **302**, 114 (2015). doi:[10.1016/j.jcp.2015.08.042](https://doi.org/10.1016/j.jcp.2015.08.042)
- [122] N.P. Waterson, H. Deconinck, *J. Comput. Phys.* **224**(1), 182 (2007). doi:[10.1016/j.jcp.2007.01.021](https://doi.org/10.1016/j.jcp.2007.01.021)
- [123] J. Crank, P. Nicolson, in *Math. Proc. Camb. Philos. Soc.*, vol. 43 (1947), vol. 43, pp. 50–67. doi:[10.1017/S0305004100023197](https://doi.org/10.1017/S0305004100023197)
- [124] M. Klein, A. Sadiki, J. Janicka, *J. Comput. Phys.* **186**(2), 652 (2003). doi:[10.1016/S0021-9991\(03\)00090-1](https://doi.org/10.1016/S0021-9991(03)00090-1)
- [125] C. Bogey, C. Bailly, *Acta Acustica united with Acustica* **88**(4), 463 (2002)
- [126] W. Polifke, C. Wall, P. Moin, *J. Comput. Physik* **213**(1), 437 (2006). doi:[10.1016/j.jcp.2005.08.016](https://doi.org/10.1016/j.jcp.2005.08.016)
- [127] T.J. Poinso, S. Lelef, *J. Comput. Physik* **101**(1), 104 (1992). doi:[10.1016/0021-9991\(92\)90227-p](https://doi.org/10.1016/0021-9991(92)90227-p)
- [128] K.W. Thompson, *J. Comput. Phys.* **68**(1), 1 (1987). doi:[10.1016/0021-9991\(87\)90041-6](https://doi.org/10.1016/0021-9991(87)90041-6)
- [129] G. Hedstrom, *J. Comput. Phys.* **30**(2), 222 (1979). doi:[10.1016/0021-9991\(79\)90100-1](https://doi.org/10.1016/0021-9991(79)90100-1)
- [130] N. Guézennec, T. Poinso, *AIAA J.* **47**(7), 1709 (2009). doi:[10.2514/1.41749](https://doi.org/10.2514/1.41749)
- [131] G.R. Tabor, M. Baba-Ahmadi, *Comput. Fluids* **39**(4), 553 (2010). doi:[10.1016/j.compfluid.2009.10.007](https://doi.org/10.1016/j.compfluid.2009.10.007)
- [132] T. Lieuwen, H. Torres, C. Johnson, B.T. Zinn, *J. Eng. Gas Turbines Power.* **123**(1), 182 (2001). doi:[10.1115/1.1339002](https://doi.org/10.1115/1.1339002)
- [133] J.J. Keller, *AIAA J.* **33**(12), 2280 (1995). doi:[10.2514/3.12980](https://doi.org/10.2514/3.12980)
- [134] S. Goers, B. Witzel, J. Heinze, G. Stockhausen, J. van Kampen, C. Schulz, C. Willert, C. Fleing, in *ASME Turbo Expo 2014: Turbine Technical Conference and Exposition* (2014), p. V04BT04A048. doi:[10.1115/GT2014-26977](https://doi.org/10.1115/GT2014-26977)
- [135] P. Wolf, G. Staffelbach, A. Roux, L. Gicquel, T. Poinso, V. Moureau, *Comptes Rendus Mecanique* **337**(6-7), 385 (2009). doi:[10.1016/j.crme.2009.06.003](https://doi.org/10.1016/j.crme.2009.06.003)

- [136] A. Urbano, L. Selle, G. Staffelbach, B. Cuenot, T. Schmitt, S. Ducruix, S. Candel, *Combust. Flame* **169**, 129 (2016). doi:[10.1016/j.combustflame.2016.03.020](https://doi.org/10.1016/j.combustflame.2016.03.020)
- [137] J. O'Connor, T. Lieuwen, *Combust. Sci. Technol.* **183**(5), 427 (2011). doi:[10.1080/00102202.2010.529478](https://doi.org/10.1080/00102202.2010.529478)
- [138] M. Zellhuber, C. Meraner, R. Kulkarni, W. Polifke, B. Schuermans, *J. Eng. Gas Turbines Power.* **135**(9), 091508 (2013). doi:[10.1115/1.4024940](https://doi.org/10.1115/1.4024940)
- [139] M. Zellhuber, W. Polifke, in *Direct and Large-Eddy Simulation IX* (Springer, 2015), pp. 533–539. doi:[978-3-319-14448-1\\_68](https://doi.org/978-3-319-14448-1_68)
- [140] J. O'Connor, M. Kolb, T. Lieuwen, in *49th AIAA Aerospace Sciences Meeting Including the New Horizons Forum and Aerospace Exposition, Orlando, FL, January* (2011), pp. 237–252. doi:[10.2514/6.2011-237](https://doi.org/10.2514/6.2011-237)
- [141] T. Smith, B. Emerson, W. Proscia, T. Lieuwen, *Combust. Flame* (2018). doi:[10.1016/j.combustflame.2017.12.035](https://doi.org/10.1016/j.combustflame.2017.12.035)
- [142] A. Saurabh, J.P. Moeck, C.O. Paschereit, *J. Eng. Gas Turbines Power* **139**(6), 061502 (2017). doi:[10.1115/1.4035231](https://doi.org/10.1115/1.4035231)
- [143] F. Baillot, F. Lespinasse, *Combust. Flame* **161**(5), 1247 (2014). doi:[10.1016/j.combustflame.2013.11.009](https://doi.org/10.1016/j.combustflame.2013.11.009)
- [144] Y. Méry, *Proc. Combust. Inst.* **36**(3), 3889 (2017). doi:[10.1016/j.proci.2016.08.009](https://doi.org/10.1016/j.proci.2016.08.009)
- [145] H.G. Weller, G. Tabor, H. Jasak, C. Fureby, *Comput. Phys.* **12**, 620 (1998). doi:[10.1063/1.168744](https://doi.org/10.1063/1.168744)
- [146] H. Krediet, University of Twente, Enschede (2012)
- [147] H. Krediet, W. Krebs, J.E. Portillo, J. Kok, in *46th AIAA/ASME/SAE/ASEE Joint Propulsion Conference and Exhibit* (2010), 7150. doi:[10.2514/6.2010-7150](https://doi.org/10.2514/6.2010-7150)
- [148] S. Ducruix, C. Rey, S. Candel, *Combust. Theor. Model* **9**(1), 5 (2005). doi:[10.1080/13647830500051950](https://doi.org/10.1080/13647830500051950)
- [149] M. Boger, D. Veynante, *Advances in Turbulence VIII* pp. 449–452 (2000)
- [150] C.J. Greenshields, OpenFOAM Foundation Ltd, version **3**(1) (2015)

- [151] B.J. McBride, S. Gordon, M.A. Reno, in *NASA Report TM-4513* (1993). doi:[10.1016/b978-1-4832-0083-5.50013-0](https://doi.org/10.1016/b978-1-4832-0083-5.50013-0)
- [152] R.I. Issa, *J. Comput. Phys* **62**(1), 40 (1986). doi:[10.1016/0021-9991\(86\)90099-9](https://doi.org/10.1016/0021-9991(86)90099-9)
- [153] T. Nguyen, A.M. Kempf, *Oil Gas Sci. Technol.* **72**(4), 1 (2017). doi:[10.2516/ogst/2017023](https://doi.org/10.2516/ogst/2017023)
- [154] J. Crank, P. Nicolson, *Adv. Comput. Math.* **6**(1), 207 (1996). doi:[10.1007/BF02127704](https://doi.org/10.1007/BF02127704)
- [155] S. Ducruix, T. Schuller, D. Durox, S. Candel, *J. Propul. Power* **19**(5), 722 (2003). doi:[10.2514/2.6182](https://doi.org/10.2514/2.6182)
- [156] Y. Dubief, F. Delcayre, *J. Turbul.* **1**(1), 011 (2000). doi:[10.1088/1468-5248/1/1/011](https://doi.org/10.1088/1468-5248/1/1/011)
- [157] H. Preetham, H. Santosh, T. Lieuwen, *J. Propul. Power* **24**(6), 1390 (2008). doi:[10.2514/1.35432](https://doi.org/10.2514/1.35432)
- [158] M.P.G. Zellhuber, High frequency response of auto-ignition and heat release to acoustic perturbations. Ph.D. thesis, Technische Universität München (2013)
- [159] V. Sharifi, C. Beck, A. Kempf, in *29. Deutscher Flammentag (German Flame Day), Bochum* (2019), pp. 1–10
- [160] A. Sjunnesson, S. Olovsson, B. Sjoblom, VFA9370-308 (1991)
- [161] B. Rochette, F. Collin-Bastiani, L. Gicquel, O. Vermorel, D. Veynante, T. Poinsot, *Combust. Flame* **191**, 417 (2018). doi:[10.1016/j.combustflame.2018.01.016](https://doi.org/10.1016/j.combustflame.2018.01.016)
- [162] D. Maestro, A. Ghani, L.Y. Gicquel, T. Poinsot, in *55th AIAA Aerospace Sciences Meeting* (2017), p. 1576. doi:[10.2514/6.2017-1576](https://doi.org/10.2514/6.2017-1576)
- [163] B. Winden, Powering performance of a self-propelled ship in waves. Ph.D. thesis, University of Southampton (2014)
- [164] A. Yoshizawa, K. Horiuti, *J. Phys. Soc. Jpn.* **54**(8), 2834 (1985). doi:[10.1143/jpsj.54.2834](https://doi.org/10.1143/jpsj.54.2834)
- [165] V. Sharifi, C. Beck, B. Janus, A.M. Kempf, *AIAA Journal* pp. 1–17 (2021). doi:[10.2514/1.J060072](https://doi.org/10.2514/1.J060072)
- [166] K.H. Usow, C.L. Meyer, F.W. Schulze, (1953)

- [167] W. Kaskan, A. Noreen, ASME Transactions **77**(6), 855 (1955)
- [168] T. Male, W.R. Kerslake, A.O. Tischler, *Photographic study of rotary screaming and other oscillations in a rocket engine* (NACA, 1954)
- [169] F.E. Culick, V. Yang, Liquid Rocket Engine Combustion Instability **169**, 3 (1995)
- [170] P.L. Blackshear, W.D. Rayle, L.K. Tower, (1953)
- [171] J.C. Oefelein, V. Yang, J. Propul. Power **9**(5), 657 (1993)
- [172] T. Ma, Y. Gao, A.M. Kempf, N. Chakraborty, Combust. Flame **161**(12), 3134 (2014). doi:[10.1016/j.combustflame.2014.05.023](https://doi.org/10.1016/j.combustflame.2014.05.023)
- [173] A. Urbano, Q. Douasbin, L. Selle, G. Staffelbach, B. Cuenot, T. Schmitt, S. Ducruix, S. Candel, Proc. Combust. Inst. **36**(2), 2633 (2017). doi:[10.1016/j.proci.2016.06.042](https://doi.org/10.1016/j.proci.2016.06.042)
- [174] J. Li, Y. Xia, A.S. Morgans, X. Han, Combust. Flame **185**, 28 (2017). doi:[/10.1016/j.combustflame.2017.06.018](https://doi.org/10.1016/j.combustflame.2017.06.018)
- [175] Y. Méry, Combust. Flame **192**, 410 (2018). doi:[10.1016/j.combustflame.2018.02.007](https://doi.org/10.1016/j.combustflame.2018.02.007)
- [176] L. Euler, *Institutionum calculi integralis*, vol. 1 (impensis Academiae imperialis scientiarum, 1824)
- [177] S. Candel, Proc. Combust. Inst. **29**(1), 1 (2002)
- [178] M.S. Natanzon, *Combustion instability* (AIAA, 2008). doi:[/10.2514/4.866913](https://doi.org/10.2514/4.866913)
- [179] O. Lammel, T. Rödiger, M. Stöhr, H. Ax, P. Kutne, M. Severin, P. Griebel, M. Aigner, in *ASME Turbo Expo* (2014), p. V04BT04A031. doi:[10.1115/GT2014-26376](https://doi.org/10.1115/GT2014-26376)
- [180] A.P. Dowling, J. Fluid Mech. **346**, 271 (1997). doi:[10.1017/S0022112097006484](https://doi.org/10.1017/S0022112097006484)

# DuEPublico

Duisburg-Essen Publications online

UNIVERSITÄT  
DUISBURG  
ESSEN

*Offen im Denken*

ub | universitäts  
bibliothek

Diese Dissertation wird via DuEPublico, dem Dokumenten- und Publikationsserver der Universität Duisburg-Essen, zur Verfügung gestellt und liegt auch als Print-Version vor.

**DOI:** 10.17185/duepublico/74576

**URN:** urn:nbn:de:hbz:464-20210809-150531-3

Alle Rechte vorbehalten.